

Simulation of Interaction of EUV with Metal Oxide Resists

Master Thesis

Author	Hsin-Tien, Li (Zoe)
Supervisors at TU Delft	Dr. Marcel Sluiter
Supervisors at ASML	Dr. Syam Parayil Venugopalan Dr. Luc van Kessel



Materials Science and Engineering, TU Delft
Master Thesis with ASML

Acknowledgement

I first visited Europe for a solo trip when I was 19 years old , and my first stop was the Netherlands. Ever since, studying in Europe has been on my bucket list. Now here I am, nearing the end of my master's degree. I have received immense kindness and support during my graduation project, and I would like to express my sincere gratitude to everyone who contributed to this journey.

First of all, deepest thanks to my ASML supervisors, Syam and Luc. Syam, thank you for recruiting me at the beginning and mentoring me not only in scientific endeavors but also in becoming a more well-rounded professional. Your leadership qualities have been truly inspiring. Luc, I am truly grateful for your kindness to spend extra time co-supervising my project. Your expertise with Nebula and photoresist accelerated the project progress. Your solid knowledge of physics and your patience in guiding juniors are truly impressive. I also appreciate Marcel's guidance as my university supervisor, providing fresh perspectives to my research. Your passion and curiosity for science were evident from the first day we met during the introduction week at TU Delft and it's very contagious.

Additionally, I would like to acknowledge others at ASML Research. Liesbeth, thank you for your care, career advice, and for connecting me with the right people. Vina, your warmth and our discussions about artworks, Taiwanese culture and food were really delightful. Shi-Chi, thanks for always being caring and inviting me to your home for dinner during my first month at ASML. Shao-Hsuan, my Taiwanese intern partner, I am happy to meet you here. Working on weekends together and sharing funny memes has been great. Completing my graduation project at ASML Research has been a valuable experience, surrounded by brilliant minds working on fascinating projects. Thanks for all the friendly smiles at the office and random chats in the coffee corner. I was always told that doing the internship in Research is quite isolated, but I never feel that. Moreover, I'd like to give a shout-out to the cleaning staff at Research. You are always the first person I greet in the morning when I come to the office early. Without you, we wouldn't have a clean workplace. Thank you for all that you do.

Outside the workplace, special thanks to Floris at Heckert & van Lierop Orthopedic Center for promptly fixing my prosthetics, enabling me to physically present in the office. I enjoyed our conversations about cooking, travel etc and those jokes about socket needles. Really look forward to the new prosthetic joint that will allow me to bike again after 11 years! Mirna, thank you for inviting me to your lovely house in Eindhoven and cuddle your newborn. It's amazing how we connected like old friends, sharing similar childhood cancer journeys while in different countries. I am grateful Floris connected us.

Thanks to my gym buddy Dennis, the first friend I made in Veldhoven outside of work. Thanks for reaching out. I enjoy our chats at the gym, those high-protein meal hacks as well as your engineer life in ASML. Kitty, my previous roommate, I loved our cooking sessions, making desserts (glad we haven't explode the kitchen), and those deep conversations in the night. To all my wonderful friends in Delft, thank you for inviting me back to Delft for your housewarming parties, dinners, and Dutch festivals,

and introducing me to your friends in Eindhoven, ensuring I never felt lonely.

I am thankful for the scholarships from the Taiwanese Ministry of Education, TSMC, and Delta Electronics, which allowed me to study abroad without financial worries.

Thanks to my family in Taiwan for always being supportive and being my strongest backbone. Also, thanks to Micah, those motorcycle road trips we did last year were unforgettable: the golden hour in Portugal, serene mornings in Norway with salmon and brown cheese sandwiches, the coolest Airbnb host in Denmark, the babbling brook in a random forest in Germany, riding in -3 °C in Switzerland, the stunning mountains in the Dolomites, Italy, and the many petting farms in the Netherlands. These memories have fueled me through my thesis.

Lastly, thanks to Mi-De, the cutest cat in the world. It's sad you couldn't be my 'cannabis' during my master, but I will bring you here soon. I hope you will love the Netherlands, this beautiful country with wonderful people.

Zoe, Li
Veldhoven, August 2024

Abstract

Extreme Ultraviolet (EUV) lithography plays a crucial role in the semiconductor industry, enabling the shrinkage of transistor sizes and sustaining Moore's law. However, the high cost of EUV light limits the number of available photons for high-volume wafer manufacturing. To maximize the utilization of each incoming photon, metal-oxide resist (MOR) has emerged as a promising candidate to replace conventional chemically-amplified resist due to its higher absorption coefficient when exposed to EUV light.

An open-source Monte Carlo based simulator is used in this study to model electron scattering within the photoresist materials. When EUV light strikes the photoresist, initial high-energy photoelectrons are generated, triggering a series of scattering events that produce a cascade of secondary electrons (SEs). These SEs possess energies capable of altering the chemistry of resist materials, leading to pattern formation in the following processes.

In this study, we propose a novel method of applying an electric field to the resist layer to enhance pattern performance under a fixed EUV dose. Simulation results demonstrate that this approach creates an anisotropic electron blur extended in the z direction (perpendicular to the resist surface) without compromising much the resolution in the x and y directions (parallel to the resist surface). Additionally, an increase in SE yield is observed. The optimal electric field strength, identified as -400 MV/m for MOR, results in an 11.93% increase in z -direction blur and a 3.41% increase in SE yield per absorbed photon. Moreover, the asymmetry of z -direction blur counteracts the EUV light absorption near the surface and contributes to more chemical conversions deeper in the resist.

Contents

Acknowledgement	i
Abstract	iii
Abbreviations	vi
1 Introduction	1
1.1 Background	1
1.1.1 Microchip and Moore's Law	1
1.1.2 Approaches to Continue Moore's Law	2
1.2 Photolithography	3
1.2.1 Extreme Ultraviolet (EUV) Lithography	5
1.3 Photoresist Materials	7
1.3.1 Resist Performance Metrics	7
1.3.2 Chemically Amplified Resist (CAR)	9
1.3.3 Metal-Oxide Resist (MOR)	10
1.3.4 Comparison of CAR and MOR	12
1.4 Photon Absorption and Photoelectrons Generation	17
1.5 Scattering Events Inside the Resist	18
1.5.1 Dielectric Function and Energy Loss Function (ELF)	18
1.5.2 Elastic and Inelastic Scattering Events	19
1.5.3 Secondary Electron Yield	21
1.5.4 Inelastic Mean Free Path	22
1.5.5 Resist Blur	23
1.6 Problem Statement	28
2 Methodology and Materials	29
2.1 Photoresist Materials: MOR and PMMA	29
2.1.1 Optical Properties	29
2.1.2 Mean Free Path and Kinetic Energy	30
2.1.3 Electronic Band Structure	32
2.2 Nebula Settings Changes	33
2.2.1 Photoelectron Generation Methods	33
2.2.2 Energy Loss Filters	37
2.2.3 Cut-off Energy to Stop Tracking Electrons	39
2.2.4 Energy Threshold To Divide Inner and Outer Shell	39
2.3 Apply an Electric Field	40
2.4 Events Sampling in Nebula and Electric Field Influence	42
3 Results and Discussion	44
3.1 Interaction Volume Plot	44
3.1.1 z -direction Analysis	46
3.1.2 r -direction Analysis (with different z bins)	47
3.1.3 r -direction Analysis (Effective Radius)	48

3.2	Number of Useful SE Yield per Absorbed Photon	49
3.3	Qualitative Measurement of x -blur and z -blur	51
3.3.1	Definition of Blur Size	52
3.3.2	x -blur	54
3.3.3	z -blur	56
3.3.4	Anisotropy (S)	58
3.4	Influence of deformation potential on electron blur	59
3.5	Influence of Electric Field on SE with Low Energy	63
3.5.1	Observations in Simulation	63
3.5.2	Conceptual Analysis	64
3.5.3	Quantitative Analysis: Method 1	65
3.5.4	Quantitative Analysis: Method 2	66
3.6	Influence of Cut-off Energy on Results	68
3.6.1	Observations in Simulation	68
3.6.2	Conceptual Analysis	69
3.6.3	Quantitative Analysis	69
3.7	Influence of VB width on Results	71
3.7.1	Observations in Simulation	71
3.7.2	Conceptual Analysis	72
3.7.3	Quantitative Analysis	73
3.8	Compare the influence of Cut-off Energy and VB Width	74
3.9	Compare Mott and Phonon Scattering Models for Sub-100 eV Energies	74
3.9.1	Observations in Simulation	75
3.9.2	Conceptual Analysis	76
3.9.3	Quantitative Analysis	77
3.10	Feasibility Study	78
3.11	Alternative Metrics for Analyzing Electron Blur Size	80
3.11.1	Definition of Blur Size	80
3.11.2	x -blur	81
3.11.3	z -blur	82
3.11.4	Anisotropy (S)	83
4	Conclusion	85
5	Recommendations	87
5.1	Limitations of Simulation	87
5.2	Future Work	88
	References	90
A	Material Properties	97
A.1	MOR material parameters	97
A.2	MOR optical data	99
A.3	PMMA material parameters	100
A.4	PMMA optical data	101
B	High Performance Cluster Computational Resource	102

Abbreviations

Abbreviation	Definition
AMCs	Airborne Molecularcontaminants
CAR	Chemically Amplified Resist
CB	Conduction Band
CD	Critical Dimension
CPU	Central Processing Unit
DUV	Deep Ultraviolet
DOF	Depth Of Focus
DC	Direct Current
EUV	Extreme Ultraviolet
ELF	Energy Loss Function
FET	Field-Effect Transistor
GAAFET	Gate-all-around Field-Effect Transistor
HPC	High Performance Cluster
K	Kinetic Energy
L/S	Line and Space
LER	Line Edge Roughness
LWR	Line Width Roughness
MOR	Metal Oxide Resist
MBCFET	Multi Bridge ChannelFET
NA	Numerical Aperture
PAG	Photoacid Generator
PMMA	Polymethyl Methacrylate
PED	Post-Exposure Delay
PEB	Post-Exposure Bake
RC	Resistor-Capacitor
SEM	Scanning Electron Microscope
SE	Secondary Electron
VB	Valence Band

Introduction

1.1. Background

1.1.1. Microchip and Moore's Law

A microchip, composed of semiconductor material housing millions of transistors and electronic components, can be seen everywhere in contemporary electronics, determining system computing performance. Transistors, semiconductor devices responsible for amplifying or switching electrical signals and power, are fundamental to microchip functionality. Gordon Moore, a co-founder of Intel, introduced Moore's Law, positing that the number of transistors on an integrated circuit would double approximately every two years, as shown in Figure 1.1. Sustaining Moore's Law by reducing transistor size remains a primary objective within the semiconductor industry, because it enables faster and more powerful chips, which will be discussed later in section 1.1.2.

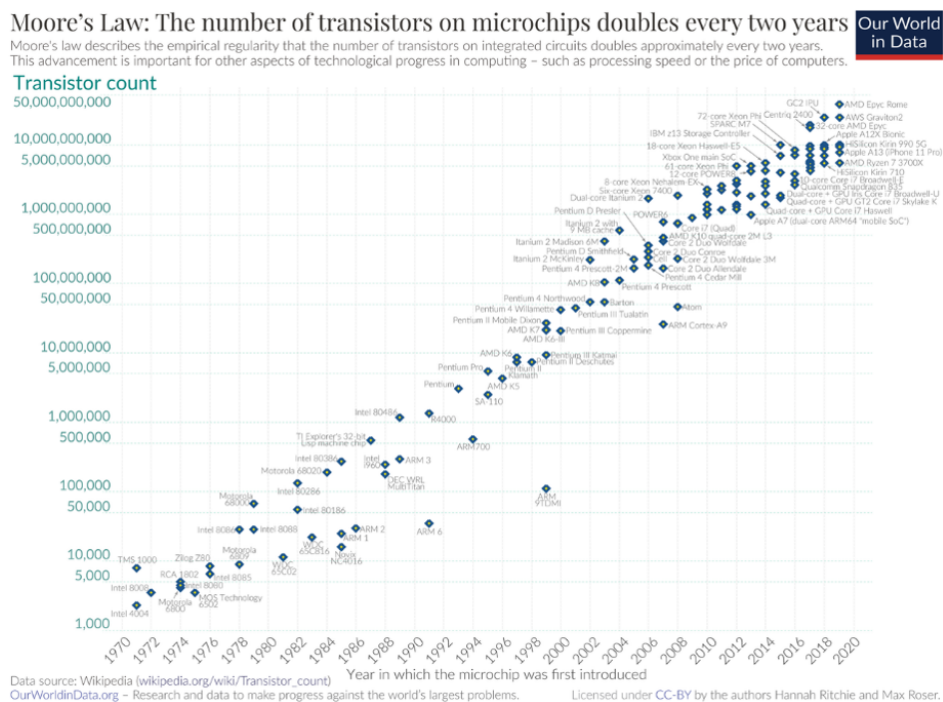


Figure 1.1: Moore's Law [86]

1.1.2. Approaches to Continue Moore's Law

A transistor consists of three terminals: the source, where current enters the transistor; the drain, where current flows out of the transistor; and the gate, which controls the conductivity between the source and drain through the application of varying voltages.

There are several strategies to continue transistor miniaturization in accordance with Moore's Law. First of all, transitioning transistor structures from two-dimensional to three-dimensional configurations allows for more transistors to be packed into a given area on the chip. Figure 1.2 illustrates the evolution of transistor architecture.

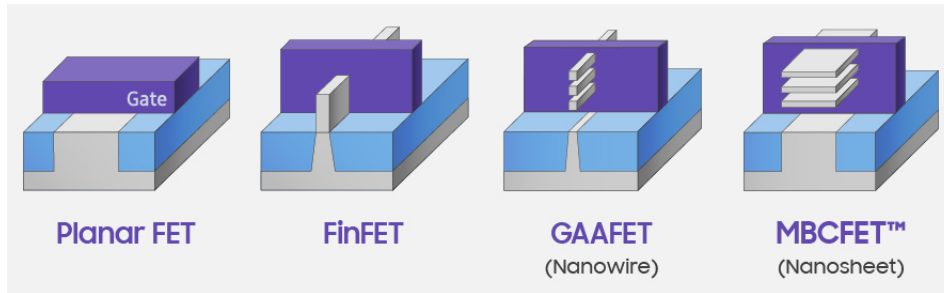


Figure 1.2: The evolution of transistor structure [90]

Initially, these fundamental elements were constructed on a two-dimensional plane, known as Planar FET (Field-Effect Transistor). The term "field-effect" arises from the fact that the conductivity of the material is modulated by an electric field. Over time, the three-dimensional FinFET (Fin Field-Effect Transistor) emerged, featuring a gate wrapped around the channel between the source and drain, with three contact surfaces. FinFETs offered improved control over electric current due to the larger contact area of the gate. Additionally, their vertical fin-like structure facilitated higher transistor density on a chip. As the height of the "fin" in FinFETs approached physical limits, GAAFET (Gate-all-around Field-Effect Transistor) was developed to address this bottleneck. GAAFETs feature gates surrounded by four faces of the channel. MBCFET (Multi Bridge Channel FET) represents an advanced iteration of GAAFETs. Instead of utilizing nanowires with small cross-sections, MBCFETs employ thin nanosheets stacked together, resulting in increased contact area and enhanced power efficiency.

The shrinkage of transistor size reduces the power consumption of the microchip. Equation 1.1 illustrates the dynamic power dissipation (P) attributed to transistor switching [1]:

$$P = C \times V^2 \times f \quad (1.1)$$

where C represents the effective switching capacitance, V denotes the power supply voltage, and f is the transistor operating frequency. The downsizing of the transistor also diminishes the distance between the source and drain, thereby reducing the gate oxide area and resulting in a smaller capacitance. Hence, as demonstrated in Equation 1, when capacitance decreases, less power consumption is required to switch the transistor.

The RC (Resistor-Capacitor) time constant, as shown in Equation 1.2, is the time necessary to charge the capacitor from zero voltage to $1 - e^{-1}$ (approximately 63.1%) of the applied DC voltage value in an RC circuit.

$$\tau = RC = \frac{1}{2\pi f_c} \quad (1.2)$$

where τ represents the RC time, R and C denote resistance and capacitance respectively, and f_c indicates the cut-off frequency. Consequently, with decreasing capacitance, the RC time delay can be reduced, and the cutoff frequency can be increased, thereby accelerating the speed of transistor switching on and off. Overall, the reduction in transistor size can diminish overall power dissipation and enhance the chip's performance per wafer area.

Additionally, leveraging Extreme Ultraviolet (EUV) light during the photolithography process facilitates achieving smaller feature sizes, compared to Deep Ultraviolet (DUV) light. The difference between EUV and DUV light will be discussed later in section 1.2.1. The smallest feature size produced during lithography, also known as critical dimension (CD), can be calculated by the Rayleigh criterion shown in Equation 1.3:

$$CD = k_1 \cdot \frac{\lambda}{NA} \quad (1.3)$$

where k_1 is a parameter that related to the lithography process, λ is the wavelength of light source and NA is the numerical aperture of the optical system. According to the Rayleigh criterion, decreasing the light wavelength correlates with a reduction in critical dimensions.

1.2. Photolithography

Photolithography is a technique for creating intricate patterns on wafers, which are later diced to produce semiconductor chips. Figure 1.3 shows a full process of chips making. During lithography, wafers are subjected to light exposure projected through a photomask, a plate containing the blueprint of the desired pattern.

The lithography techniques for various technical nodes are presented in Figure 1.4. In the early days of semiconductor manufacturing, photolithography primarily utilized mercury arc lamps emitting light at specific wavelengths known as G-Line (436 nm) and I-Line (365 nm). These wavelengths were suitable for printing larger feature sizes but were limited in resolution for smaller feature sizes. As semiconductor technology advanced and feature sizes became smaller, the industry transitioned to using deep ultraviolet (DUV) excimer lasers, which generate excimer by mixing gases and release excess energy as the form of light. Depends on the types of mixed gases, different lights are generated. Krypton-Fluoride (KrF) lasers emit light with a wavelength of 248 nm, while Argon-Fluoride (ArF) excimer lasers produce light at 193 nm. This shorter wavelength facilitated even higher resolution lithography, enabling the fabrication of semiconductor devices with smaller feature sizes and greater transistor densities. To push the limits of resolution even further, immersion lithography was introduced, utilizing ArF excimer lasers in conjunction with a liquid immersion medium (usually water) to enhance resolution. As shown in equation 1.4:

$$NA = n \times \sin \theta \quad (1.4)$$

where NA is the numerical aperture, n represents the refractive index of the media and θ is one-half angle of light acceptance. Numerical aperture is therefore increased due to

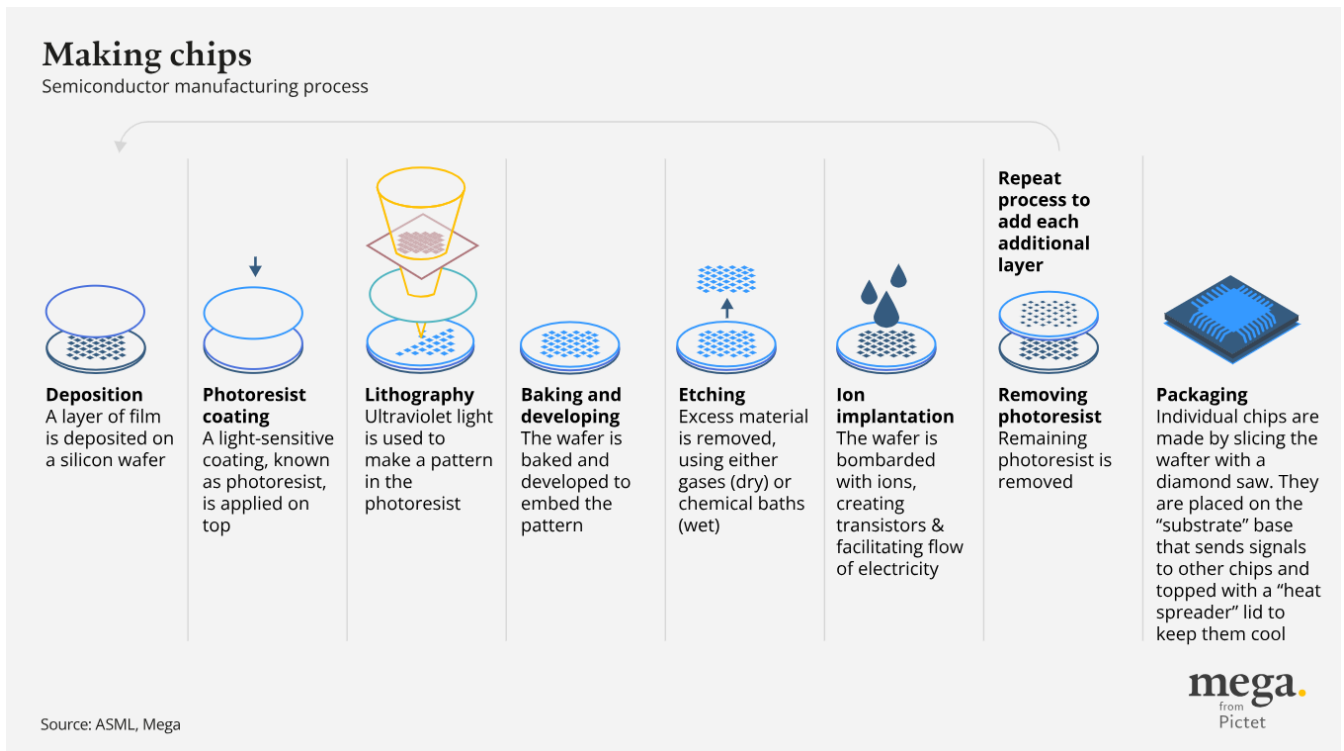


Figure 1.3: Chip making process

the higher refractive index of liquid than air. This leads to smaller critical dimension according to Equation 1.3. ArF immersion lithography became prevalent in advanced semiconductor manufacturing processes, enabling the production of chips with feature sizes below 45 nm.

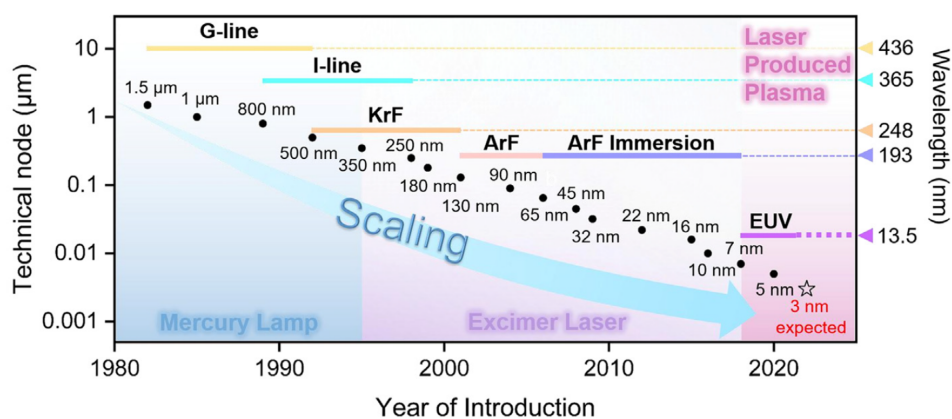


Figure 1.4: Scaling of technical nodes with the development of the semiconductor industry [104]

As semiconductor technology approached the sub-10 nm scale, traditional optical lithography faced challenges in maintaining resolution and reducing manufacturing costs. In response to this need, EUV lithography has emerged, utilizing light with a wavelength of 13.5 nm more than 14 times shorter than Deep Ultraviolet (DUV) light for finer patterning.

1.2.1. Extreme Ultraviolet (EUV) Lithography

Because of the shorter wavelength of EUV lithography, there are several fundamental differences between EUV and DUV lithography.

Firstly, the use of reflective multilayer (Bragg type) optics replaces traditional refractive optics due to the high material absorbance of EUV light, rendering refractive optics impractical. Reflective multilayer coatings, comprise of alternating layers of specific materials, which reflect EUV light through constructive interference [5, 15].

Secondly, EUV lithography employs a plasma light source instead of a DUV laser. As shown in Figure 1.5, the generation of EUV light involves a process known as laser-produced plasma (LPP). In this process, a high-powered laser beam is directed onto a droplet of tin (Sn), generating a plasma [108, 42]. This plasma emits EUV radiation, which is then collected and focused onto a reflective mask, often referred to as a photomask or reticle. To produce enough light to manufacture microchips, this process is repeated 50,000 times per second.

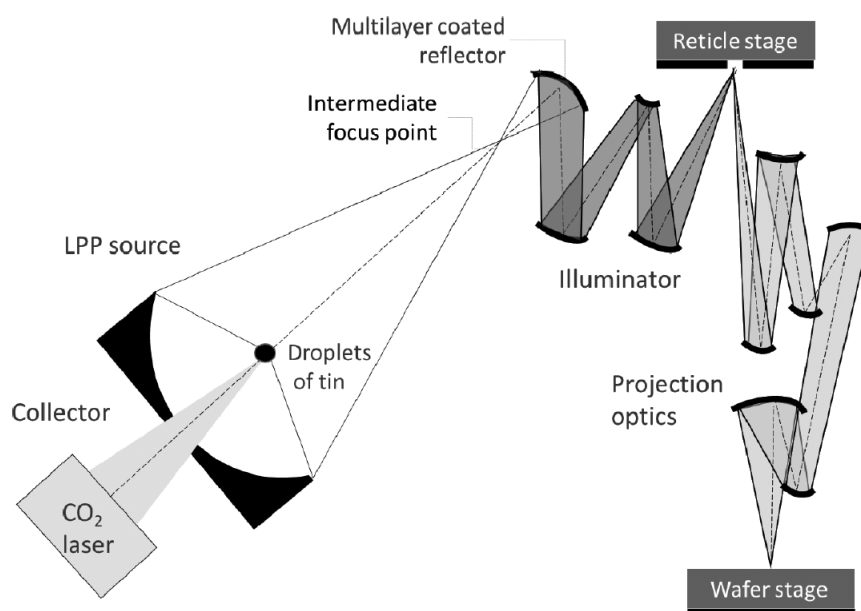


Figure 1.5: EUV light generation mechanism [30]

Thirdly, unlike DUV lithography which typically operates at atmospheric pressure, EUV lithography operates in a near-vacuum environment with stringent contamination control measures [6]. Because EUV radiation can be easily absorbed by air, operating in a near-vacuum environment prevents absorption and ensures the EUV light reaches the photoresist without significant attenuation. Normally hydrogen of 1 to 10 Pa is used as a background gas in the EUV machine because of its low absorption coefficient at EUV wavelength and its highly reductive nature, which can prevent the mirrors from contamination [58, 59]. EUV photons will ionize the hydrogen background gas and form low-density H₂ plasma. The hydrogen ions and radicals will then combine with the carbon impurities coming from fingerprints, greases or residues in lithography tools and become methane (CH₄) or other volatile hydro-carbon molecules, which can be removed by pump [57].

Lastly, when it comes to 5 nm logic technology node, EUV lithography might reduce the cost and the process complexity with single exposure. In order to achieve the similar resolution and pattern complexity at 5 nm node, ArF immersion lithography will require multiple patterning, which means 5 to 6 exposures are needed for a single layer [29, 17]. However, each exposure and the following development process will deteriorate the quality of the pattern also make the whole process too complex [20]. Especially for the logic chips, which have more complicated 2D patterns than that on memory chips, thus EUV might be more efficient for mass production below 5 nm node.

Nevertheless, even though EUV lithography possesses many advantages over DUV lithography and can be indispensable for the most advanced microchip manufacturing, photon shot noise is a potential concern for EUV lithography. Photon shot noise comes from the quantum nature of light and this effect becomes more severe when the lesser incoming photons lead to stochastic defects [26, 87, 28]. These random and isolated defects can cause printing failures, such as microbridges in pattern or randomly missing contacts [25]. As shown in Figure 1.6, the number of absorbed photons with EUV exposure is around 14 times fewer than that with ArF per mJ/cm^2 [12]. It is important to note that in this figure, doses are set to be the same in both ArF and EUV only for comparison. However, in reality, the dose for DUV is normally higher than that of EUV, because the cost of DUV light is comparatively lower than EUV light and more photons can enhance the image quality.

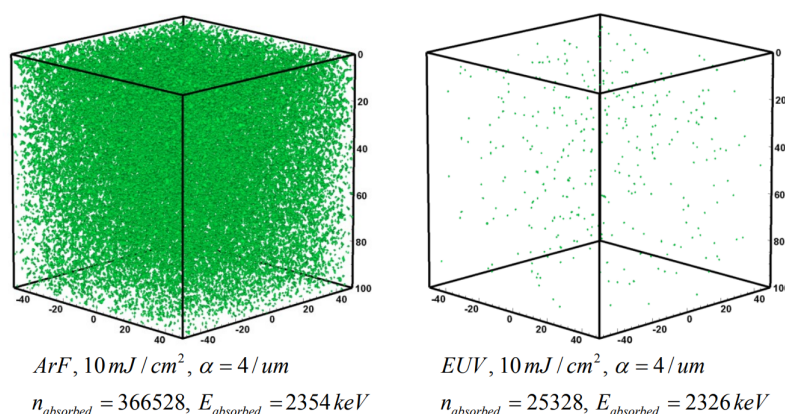


Figure 1.6: A comparison of photon counting at ArF (193 nm) and EUV (13.5 nm) in a volume when absorbance coefficient and dose are constant across wavelength [12]

Over the past few years, EUV lithography has matured for High Volume Manufacturing (HVM). The NXE:3400 with a low numerical aperture (NA) of 0.33 and a resolution of 13 nm has been employed for the 7 nm and 5 nm technology nodes. To enable cost-effective shrink beyond the 3 nm technology node, a new high NA EUV platform is being developed. In December 2023, ASML shipped the first modules of the first high NA EUV lithography system (TWINSCAN EXE:5000) to Intel. The EXE series can achieve the resolution of 8 nm, which means they can print transistors 1.7 times smaller than low NA NXE systems. The increased resolution means that more circuits can be packed into a smaller area, leading to higher chip yields per wafer and ultimately reducing production costs per chip.

1.3. Photoresist Materials

A photoresist is a light-sensitive material that undergoes a chemical transformation upon exposure to light, thereby altering its solubility in a specific solvent. Within the realm of photolithography, photoresist materials are categorized into positive-tone and negative-tone categories based on their behavior upon light exposure, as presented in Figure 1.7. Positive-tone resists become more soluble when subjected to light, while negative-tone resists exhibit reduced solubility. Following exposure, etching and development procedures are employed to transfer the pattern defined within the resist material onto the semiconductor substrate, as shown in Figure 1.3, thereby facilitating the fabrication of intricate semiconductor devices.

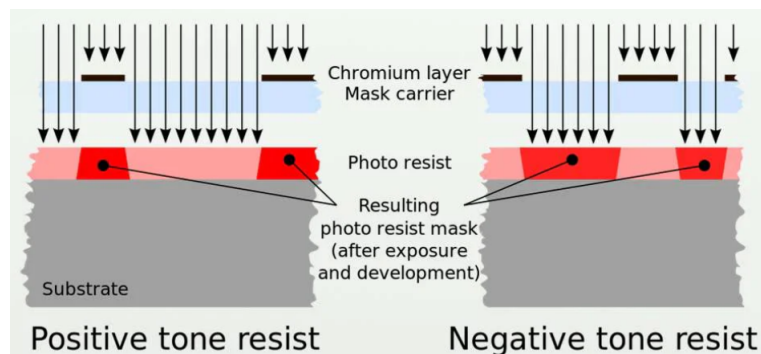


Figure 1.7: Positive and negative type of photoresists [53]

1.3.1. Resist Performance Metrics

In semiconductor photolithography, the performance of photoresist materials is assessed through various metrics, including resolution, line edge roughness (LER)/ line width roughness (LWR), sensitivity, and the trade-off between these factors [2].

First of all, resolution refers to the smallest feature size that can be reliably patterned on a semiconductor substrate using the photoresist material. It is typically characterized by the minimum achievable linewidth or spacing between features. A higher resolution indicates the ability to print smaller features with greater precision, leading to denser and more intricate semiconductor devices.

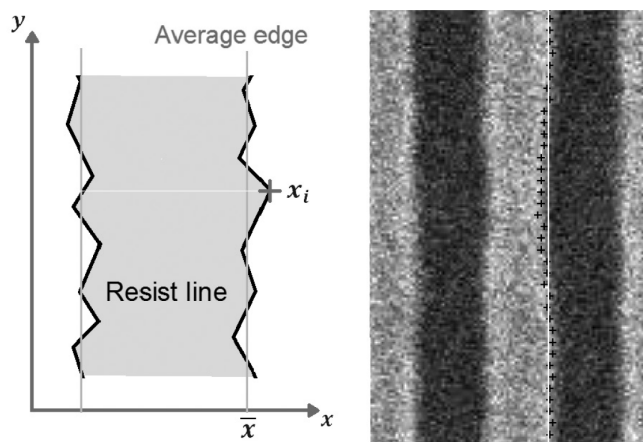


Figure 1.8: LER measurement and SEM image of a resist line pattern [30]

Secondly, LER quantifies the irregularities or fluctuations along the edges of patterned features in the photoresist material. Figure 1.6 presents the fluctuations of the line edges of the resist [30]. LER can be calculated as 3 times of the standard deviation value, as shown in Equation 1.5 and Equation 1.6 [30], where x_i means the individual point chosen, \bar{x} stands for the mean value of all points and N is the total number of selected points.

$$\sigma_{LER} = \sqrt{\frac{\sum_{i=1}^N (x_i - \bar{x})^2}{N}} \quad (1.5)$$

$$LER = 3 \times \sigma_{LER} \quad (1.6)$$

Figure 1.9 shows the illustration of LER and LWR of a resist pattern. Assume the left and right side edges are independent of each other, LWR is proportional to LER as shown in Equation 1.7 [16, 76]. It is an important parameter as smooth and well-defined edges are crucial for ensuring the functionality and reliability of semiconductor devices. Excessive LER, typically on the order of a few nanometers, may impact circuit resistance, leading to slower signal propagation or short circuits, thereby degrading device performance [94]. Historically, LER was not a major concern due to its negligible impact compared to feature size. However, with the advancement of technology nodes and the shrinking of feature sizes, LER has become increasingly significant as it approaches the scale of feature dimensions.

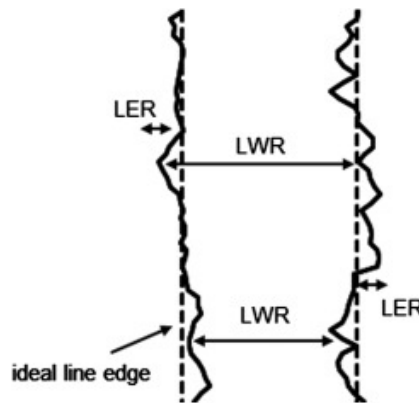


Figure 1.9: The illustration of LER and LWR [66]

$$LWR = \sqrt{2} \times LER \quad (1.7)$$

Lastly, sensitivity in photolithography refers to the photoresist material's responsiveness to light exposure, specifically indicating the amount of light energy needed to produce a desired feature and is measured in mJ/cm^2 [30]. A highly sensitive resist requires lower energy input to create a feature, making it essential for situations where light source intensity is low [105]. Sensitivity plays a crucial role in determining the efficiency and cost-effectiveness of semiconductor manufacturing processes, as it reduces the energy usage while still achieving the desired feature resolution, which increases the throughput of fabrication. Some literature mention that for industrialized production criteria, the photoresist should have a sensitivity smaller than $20 \text{ mJ}/\text{cm}^2$ [70, 96]. However, in

ASML product catalog, the specification is 30 mJ/cm^2 for EUV machine NXE series with 0.33 NA and most customer might use a higher value than this.

The Resolution Line edge roughness Sensitivity (RLS) trade-off is a fundamental consideration in photoresist performance [84]. It reflects the inherent challenge of simultaneously achieving high resolution, low LER, and high sensitivity in a single resist formulation. Improving one aspect of resist performance often comes at the expense of others due to the complex interplay between resist chemistry, process parameters, and lithography equipment capabilities. Achieving optimal resist performance involves striking a balance between these competing factors.

1.3.2. Chemically Amplified Resist (CAR)

Chemically amplified resists (CARs) have been employed in both DUV and EUV photolithography. CAR typically consists of polymer matrix, absorbers, photoacid generators (PAGs), quenchers, and additives that modulate adhesion properties.

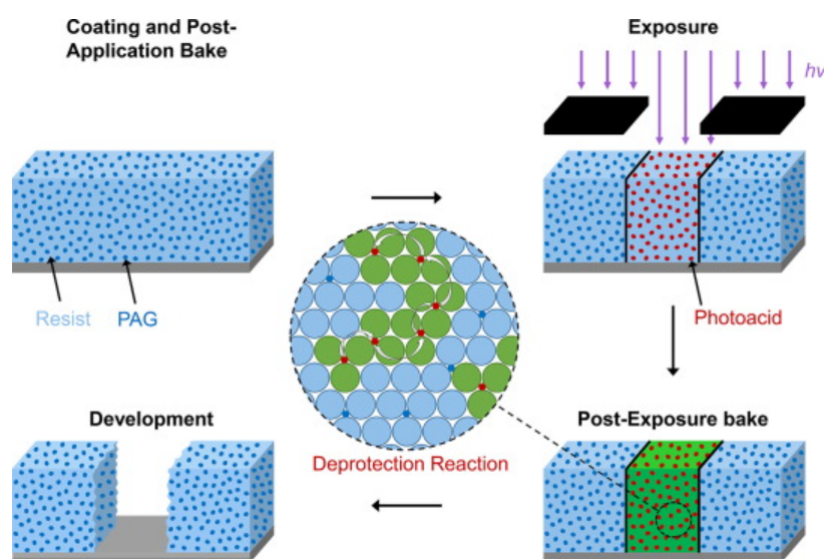


Figure 1.10: CAR mechanism [104]

As shown in Figure 1.10, under the illumination, PAGs interact with the incoming light and acid molecules are generated within the resist. Then, the wafer will undergo post-exposure bake (PEB). During the bake, the thermal energy will trigger the de-protection reaction between the acid and the polymer. This acid catalyzed reaction will modify the functional groups in the polymer matrix and thus alter the solubility of the resist. Quenchers are used to limit the diffusion of acid and control the extent of the chemical reactions, allowing for a more precise pattern.

CARs do have some limitations, especially when it comes to the EUV lithography. One of bottlenecks of CAR is that the resolution is constrained to the acid diffusion during PEB. The acid will diffuse some distance, which normally larger than the size of the resist molecule, before causing the deprotection reaction [54]. Moreover, the absorption coefficient of CAR under EUV exposure is around $4 \mu\text{m}^{-1}$ to $5 \mu\text{m}^{-1}$ [48], which leads to a significant waste of EUV illumination.

1.3.3. Metal-Oxide Resist (MOR)

MOR has emerged as promising candidates in EUV lithography, particularly in the context of high NA EUV systems [78, 4], which demand thinner photoresist layers to accommodate the reduced depth of focus (DOF) as shown in Equation 1.8 [63].

$$DOF \propto \frac{\lambda}{NA^2} \quad (1.8)$$

where λ represents the wavelength of the illuminating light and NA is the numerical aperture [49].

However, thinner resist layer limits the amount of light absorbed, necessitating materials with higher EUV absorbance to maintain patterning fidelity. Instead of employing the chemical amplification mechanism used in CAR, MOR addresses this challenge by incorporating metal particles, into the polymer matrix to enhance EUV absorption within the resist and reach the required photosensitivity [34, 95].

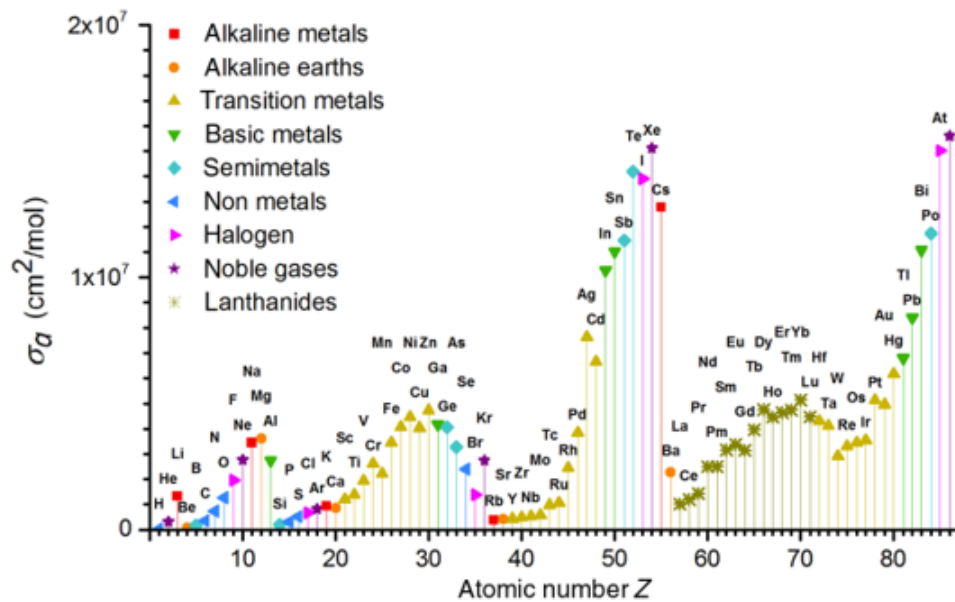


Figure 1.11: Atomic absorption cross section σ_a at EUV ($\lambda = 13.5$ nm) of elements with atomic number Z from 1 to 86 [35]

Figure 1.11 shows the atomic absorption cross section at EUV wavelength for elements with atomic number from 1 to 86. Metal atoms, such as Zn, Ti, In [47] and Sn [62, 54], are often chosen considering their relatively high absorbance under EUV exposure, cost and stability during development and etching process [67, 80]. Additionally, oxygen has a higher absorption cross section than carbon at EUV wavelength, so increasing the ratio of oxygen is expected to enhance the resist absorbance as well [75]. Among different kinds resists with metal-oxide nanoparticles, tin-based MOR made by a company called Inpria shows the best performance.

Figure 1.12 illustrates the mechanism of MOR. MO_x cluster film is composed of voxels and each voxel is made of metal-oxo core passivated with radiation-sensitive ligands. Upon EUV exposure, photoelectrons are produced inside the resist which then undergo a series of inelastic scatterings and generate the secondary electrons. The photoionization

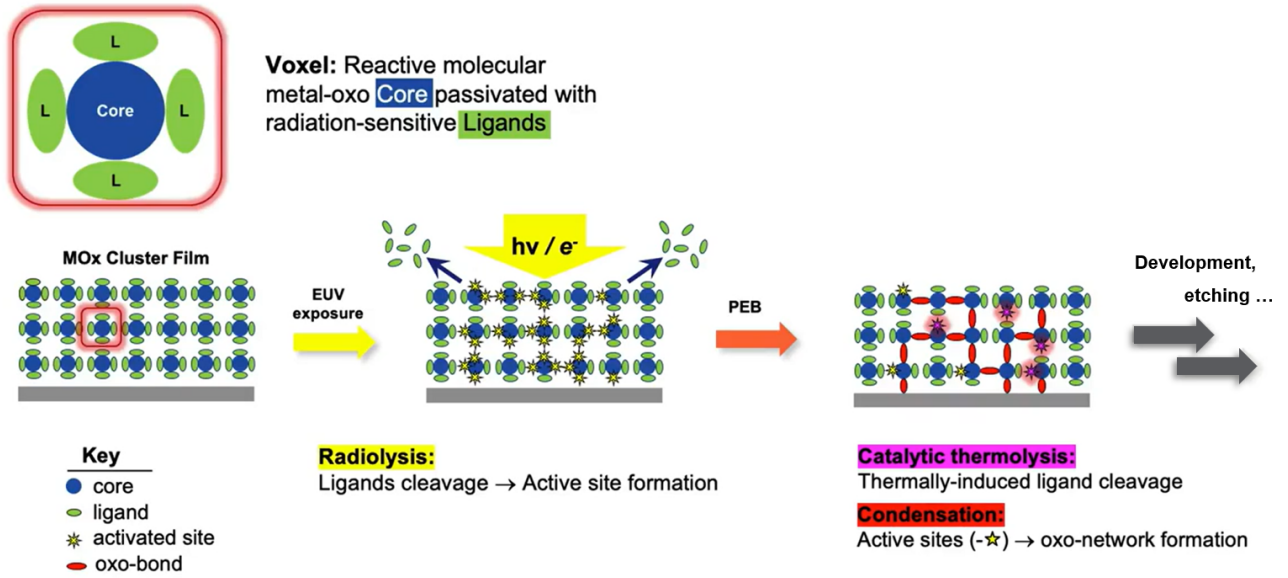


Figure 1.12: MOR mechanism [18]

and scattering events process will be elaborated in section 1.4 and 1.5. The generated secondary electrons lead to the ligand dissociation and create active sites, which is known as radiolysis. When PEB is applied, even more ligands will be cleaved through catalytic thermolysis and at the same time the active sites can crosslink with each other via condensation reaction. The condensed metal oxide bonds are insoluble in the following development solvent. Therefore, MOR ligands cleaved in both exposure and PEB steps, but the exposed area will have more catalytic thermolysis happening. In a way this is similar to an amplification mechanism, but without the need of any diffusion [18]. As presented in Figure 1.13, the effect of PEB is dose dependent, which means the higher the exposure dose, the higher fraction of ligands being dissociated during PEB and thus increase the final chemical contrast.

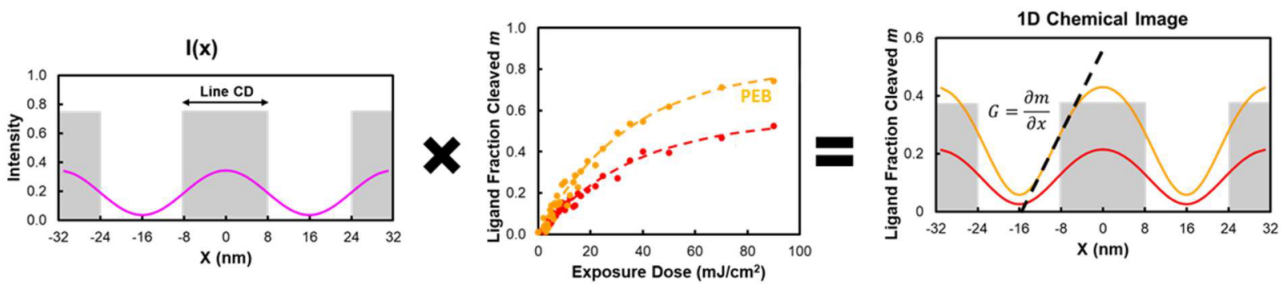


Figure 1.13: Representation of the changes in the chemical gradient expressed as fraction of ligand cleaved in a MOR resist after EUV exposure and after PEB [27]

MORs are advantageous for its high EUV absorbance and good etch resistance, which will be qualitatively compared with CARs in the section 1.3.4. However, MORs do have some drawbacks that make it not yet fully used in HVM. As described in section 1.2.1, small amount of hydrogen is used as a background gas in EUV scanner to maintain the cleanliness of mirrors. The H radicals generated under EUV radiation might interact with the metal elements in MOR and form metallic hydrides ($M_x - H_y$). The metallic hydrides might deposit on the EUV mirrors and reduce the lifetime of optics [30]. Humidity

is another factor that will affect the MOR patterning process. The moisture in the air might inhibit EUV absorption during the exposure and affect the following condensation reaction [62]. In the research done by Castellanos et al., humidity and airborne molecular contaminants (AMCs) are regarded as the two main factors that affect the MOR pattern quality [27]. Two strategies are developed to mitigate the effect of humidity and AMCs. First, stabilizing additives are utilized to either react faster with humidity and AMCs or block the sites where they might have contaminants absorbed. Second, formulations with new ligands are employed to undergo less ligand cleavage during the period of post-exposure delay (PED). During PED, MORs interact with humidity and AMCs, which cause more ligand cleavages and result in fluctuation of CD in line and space pattern image. As shown in Figure 1.14, the variation of target CD is reduced with AMC and humidity being well controlled.

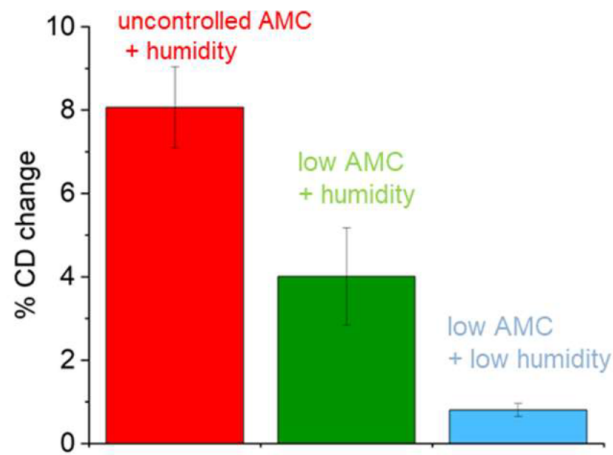


Figure 1.14: Representation of the changes in the chemical gradient expressed as fraction of ligand cleaved in a MOR resist after EUV exposure and after PEB [27]

1.3.4. Comparison of CAR and MOR

EUV Absorbance

Considering the high cost of EUV lithography, increasing the absorbance of photoresist materials is important to reduce the waste of EUV photons. The absorption coefficient of a compound can be calculated by the Equation 1.9.

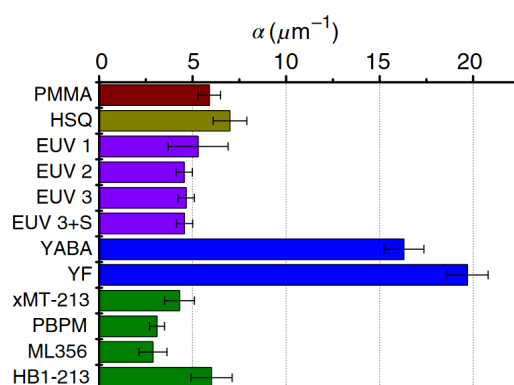
$$\alpha = \frac{N_A}{MW} \sum x_i \rho_i \sigma_{a_i} \quad (1.9)$$

where N_A is the Avogadro number, MW is the molecular weight of the compound, x_i is the relative amount of element in the compound, ρ_i its density and σ_{a_i} is density of the element. Fallica et al. measured the dynamic absorption coefficients of several CARs and MORs under EUV exposure, which are shown in Table 1.1 [36]. Figure 1.15 shows the experimental results, in which tin-based MOR produced by Inpria have significantly higher absorption coefficient of around $17 \mu\text{m}^{-1}$ compared to other CARs (about $5 \mu\text{m}^{-1}$). This means that at the same resist thickness and with the same incoming EUV photons, MORs can utilize 3 times more photons than CARs.

Moreover, boosting the absorbance can alleviate the problem of photon shot noise in EUV lithography. In Figure 1.16, a simulation result performed in Prolith compares

Table 1.1: Resist samples' description [36]

Resist	Manufacturer	Type	C.A.	Metal containing
PMMA	Sigma-Aldrich	Organic	Non-CA	N
HSQ	Dow	Inorganic	Non-CA	N
EUV 1	Undisclosed	Organic	CA	N
EUV 2	Undisclosed	Organic	CA	N
EUV 3	Undisclosed	Organic	CA	N
EUV 3 + S	Undisclosed	Organic	CA	N
YABA	Inpria	Metal oxide based	Non-CA	Y (Sn)
YF	Inpria	Metal oxide based	Non-CA	Y (Sn)
xMT-213	IM	Organic	CA	N
PBPM	IM	Organic	Non-CA	Y
ML356	IM	Organic	Non-CA	Y
HB1-213	IM	Organic	CA	Y

**Figure 1.15:** Measured linear absorption coefficient . All polymer-based resists have approximately the same value, while the tin oxide based resists (YABA and YF) have a remarkably higher [36]

the photon shot noise for both CAR and Inpria MOR at different doses. At a fixed film thickness, for Inpria MOR with high EUV absorbance, the dose required to achieve 3% relative photon shot noise is four times less than that for CAR [48].

Another model analysis, done by Stowers et al., indicates that Inpria MOR provides a minimum of a two-fold reduction in anticipated stochastic variability when compared to conventional CAR. Furthermore, simulation results obtained from Prolith demonstrate that Inpria exhibits a narrower distribution in CD compared to CAR, as shown in Figure 1.17 [95].

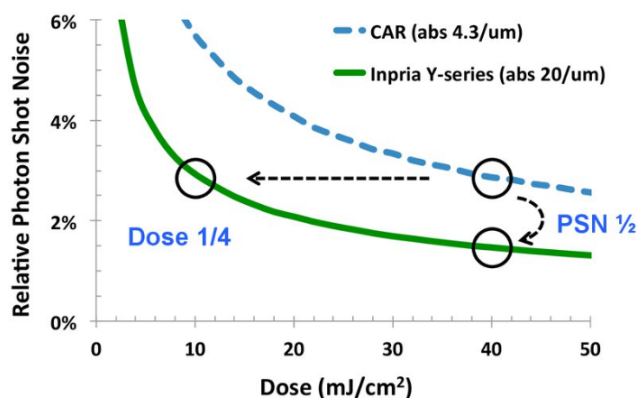


Figure 1.16: Comparison of photon shot noise contribution between conventional organic resists and Inpria Y-Series resists [48]

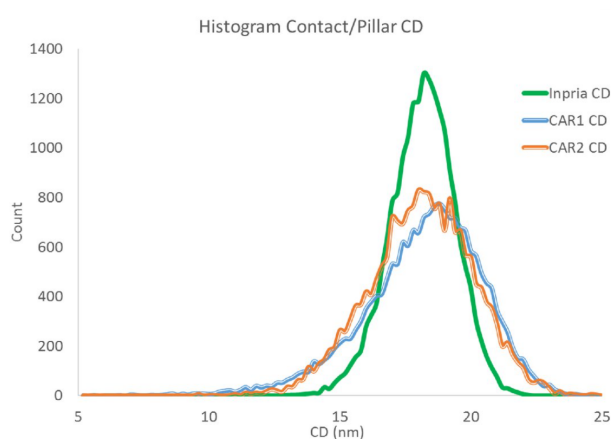


Figure 1.17: Histogram of CD's for 20,000 photon count 18nm contact/pillars simulated in Prolith for three resist models. The Inpria model shows a narrower distribution in CD by approximately a factor of 2 [95]

Etch Resistance

After exposure and development, etching is applied to remove the solvent and finalize the resist mask. As the density of circuit design on a given area is become higher and more complicated, it is essential to reduce the CD and increase the aspect ratio of the feature [56]. To get the high aspect ratio of pattern, the aspect ratio of resist layer might need to be heightened as well. However, higher aspect ratio comes with the problem of pattern collapse. Figure 1.18 illustrates the the effect of aspect ratio for CAR and MOR after etching [104]. Figure 1.18 (a) and (b) show the aspect ratio needed to be increased for higher resolution. Figure 1.18 (c) presents the issue of pattern collapse when high aspect ratio is applied to CAR. For MOR, a lower aspect ratio can achieve a high resolution thanks to its high etch resistance and selectivity. The high density of metal oxide bonds (i.e. Sn-O-Sn bonds for tin-based MOR) are considered as a reason for MOR's better etch resistance [62].

SEM Image of Pattern After Etching

Line and space pattern (L/S pattern) or contact hole pattern SEM images are usually used to evaluate the resist performance after etching. A research done by IMEC shows that, as lower exposure dose, MOR is able to achieve better LER and less defectivity with

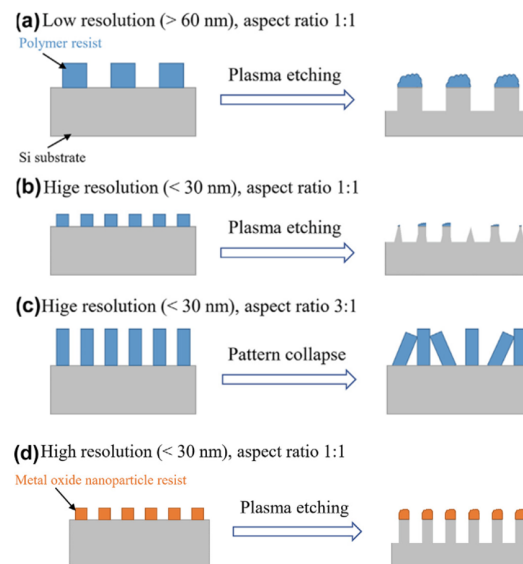


Figure 1.18: The effect of aspect ratio for CAR and MOR after plasma etching [104]

lower thickness as shown in Figure 1.19 [55].

	Metal Oxide Resist	Chemically Amplified Resist
Exposure dose (mJ/cm ²)	67	77
Nominal Film thickness (nm)	20	30
24nm pitch L/S : After etch results		
Unbiased LER (avg) 3s nm	1.48	1.55
Number of breaks/mm	0	0.23
Number of bridges/mm	0	0.39

Figure 1.19: 24nm pitch lines and spaces: patterning development for MOR and CAR. MOR is showing lower dose, better LER and defectivity, despite the low thickness [55]

Another research done by Simone et al. shows that MOR and CAR produce comparable LWR of 3.8 nm and 3.9 nm respectively with a resist thickness of 18 nm and exposure dose of 38 mJ cm⁻² for MOR and a resist thickness of 25 nm and exposure dose of 35 mJ cm⁻² for CAR, as presented in Table 1.2.

L/S patterns of CAR and MOR are shown in Figure 1.20. Some pattern collapses can be seen for CAR in Figure 1.21 (a), while there is not an issue for MOR as shown in Figure 1.21 (b). Nanobridge defectivity can be observed in both CAR and MOR, as presented in Figure 1.21 (c) and (d), in this study.

Table 1.2: Resist performance of CAR and MOR [30]

	CAR	MOR
EUV dose [mJ cm^{-2}]	35	38
Thickness [nm]	25	18
LWR [nm]	3.9	3.8

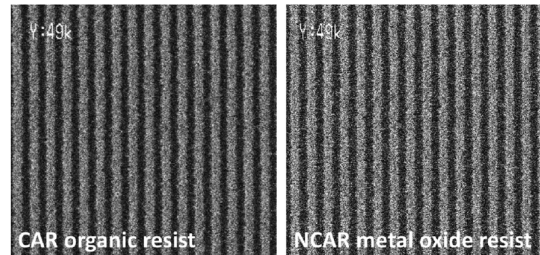


Figure 1.20: Top-down images on scanning electron microscope Hitachi CG5000 taken with rectangular scan $150 \text{ K} \times 49 \text{ K}$ magnification on a 13-nm half-pitch dense line-space pattern. Both resists were exposed at the optimum process conditions on ASML NXE3300 full-field exposure scanner at IMEC, Belgium [30]

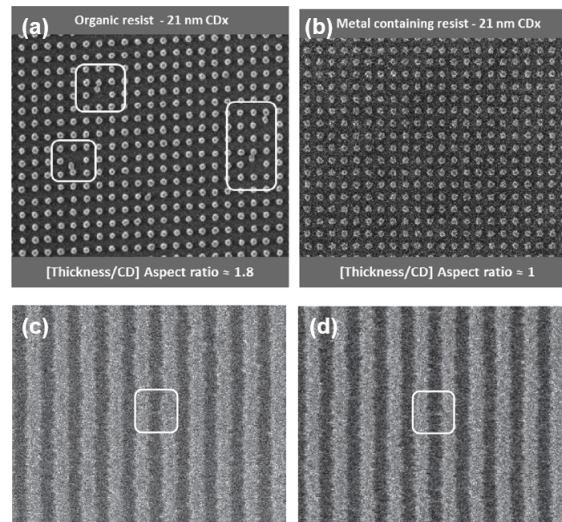


Figure 1.21: (a) a CAR with approximately 1.8 as FT/CD aspect ratio shows pattern collapse. (b) a metal oxide resist developed by Inpria Corporation with approximately 1.0 as FT/CD aspect ratio does not show pattern collapse. (c) nanobridge defectivity of CAR (d) nanobridge defectivity of MOR [30]

The smaller LER of MOR than CAR is expected to come from the differences lie in their molecular size and the fact that there is no acid diffusion occur for MOR in PEB process . MOR normally has smaller metal oxide nanoparticles size than the large molecular size in CAR, and such small particles and MOR's denser nature might minimize the scattering of electrons [80, 83]. As shown in Figure 1.22, the smaller nanoparticles in MOR is assumed to contribute to the smaller roughness than CAR. However, this is an assumption, the underlying mechanism is not yet fully understood [104].

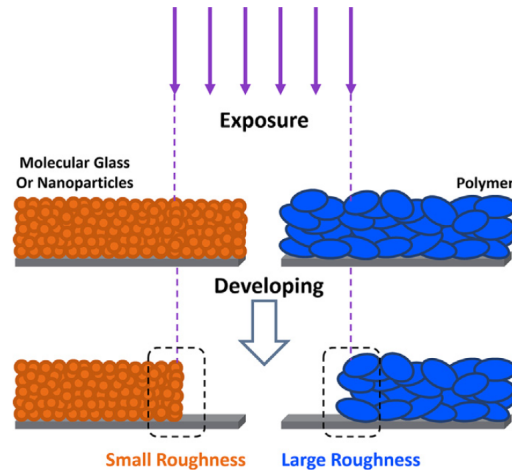


Figure 1.22: Schematic of the patterning properties of molecular glass, nanoparticle resists and polymer resists [104]

1.4. Photon Absorption and Photoelectrons Generation

Unlike DUV light, which typically has energies around 5 to 6.4 eV, EUV light with a wavelength of 13.5 nm possesses significantly higher energy of 92 eV. This heightened energy level renders EUV light not able to directly initiate certain chemical reactions, such as breaking the molecular bonds of photoresist. Consequently, the focus shifts to the role of photoelectrons and secondary electrons (SEs) generated subsequently within the resist [98]. The generation mechanism of SEs will be explained in section 1.5.3.

The interaction between incident EUV photons and photoresist leads to the ionization of valence electrons within the material, which is known as photoionization [111]. The specific binding energies of these electrons vary depending on the chemical structures of the constituent molecules in the resist. The maximum kinetic energy of the resulting photoelectrons can be determined using Equation 1.10 [11], where $h\nu$ represents the photon energy, IP is the ionization potential, m is the rest mass, v is the electron velocity, ν is the frequency of light, and h is the Planck constant.

$$\frac{1}{2}mv^2 = h\nu - IP \quad (1.10)$$

Typically, the ionization energy of the resist falls within the range of 6 to 14 eV [46, 21], resulting in photoelectrons generated by EUV photons (92 eV) with kinetic energies approximately between 78 and 86 eV [98]. For the sake of consistency, many scientific papers in this field adopt a convention of using 80 eV as the initial kinetic energy for photoelectrons in EUV simulations [8, 38, 79].

The average number of photoelectrons generated per absorbed photon can be calculated by quantum yield, as presented in Equation 1.11 [7].

$$N_e = N_p * \Phi \quad (1.11)$$

where N_e stands for the number of electrons generated, N_p means the number of photons involved and Φ represents the quantum yield. To effectively make use of each photon, higher quantum yield is desired for the commercially viable chip manufacturing.

1.5. Scattering Events Inside the Resist

The photoelectrons generated from photonization process will undergo subsequent interactions with neighboring atoms or molecules, leading to scattering events. The scattering of electrons may involve processes such as elastic scattering, in which the energy of the electron are conserved, or inelastic scattering, where the electron loses energy through interactions with the surrounding material [10]. Inelastic scattering events can result in the generation of secondary electrons cascade with low kinetic energy mostly less than 8 eV [37], which can induce dissociation of chemical bonds within the resist matrix, leading to the formation of reactive species or active sites.

1.5.1. Dielectric Function and Energy Loss Function (ELF)

When a charged particle travels through a solid material, the valence electron of material will be polarized to screen its charge [60]. Dielectric function $\varepsilon(q, \omega)$ is used to describe this response of a solid to an external electromagnetic field. The dielectric function can be measured through experiments like X-ray photoelectron spectra (XPS) [23, 52], reflection electron energy loss spectra (REELS) [110, 103] or via density functional theory calculation [107]. The dielectric function is shown in Equation 1.12:

$$\varepsilon(q, \omega) = (1 - \delta + i\beta)^2 = (n + ik)^2 \quad (1.12)$$

where q and ω are momentum transfer and energy loss related parameters during the interaction, δ and β are optical parameters of materials and can be found in Center for X-Ray Optics (CXRO) website as shown in Figure 1.23 [52]. Sometimes dielectric function is written in the format of refractive index (n) and extinction coefficient (k). Note that the optical data here are measured with momentum transfer near to zero, because the mass of photon is very small and almost negligible. As valence electrons can be nicely described as free-electron gas model, the dielectric function will then be fit with it and extrapolated for the $q > 0$ cases [60].

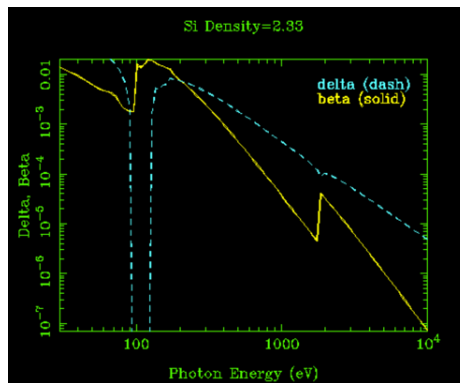


Figure 1.23: Optical parameters of silicon at different photon energy [52]

With the dielectric function, energy loss function (ELF) can be calculated accordingly, as presented in Equation 1.13. ELF is used to describe the amount of the energy loss during the inelastic scattering events.

$$ELF = Im\left[\frac{-1}{\varepsilon(q, \omega)}\right] \quad (1.13)$$

Figure 1.24 shows energy loss function of Si. The two ridges at right-hand side are corresponding to the inner shell L and K of silicon, with binding energies of around 99 eV to 149 eV and 1839 eV respectively, as shown in Table 1.3. Electronic structure of silicon is shown in Figure 1.25, with K and L being inner shells and M being outer shell accommodating four valence electrons. In the solid bulk material, these valence electrons are shared with other atoms.

In Figure 1.24, there is a maximum peak of energy loss at around 17 eV, which is the plasma frequency of the material. Plasma frequency is a collective excitation of electrons in valence band of a solid material and these bulk plasmon excitations are the dominant energy loss channel for charged particles in solid [60, 106]. For photon energy below 1 eV, there is no energy loss because of the band gap of the silicon and no electron can be excited to the forbidden gap there. In the region of very low photon energy, there are some energy loss come from the excitation of longitudinal optical phonon. These are quantized lattice vibrations that can absorb the energy transferred from the incident particle, not an electronic excitation.

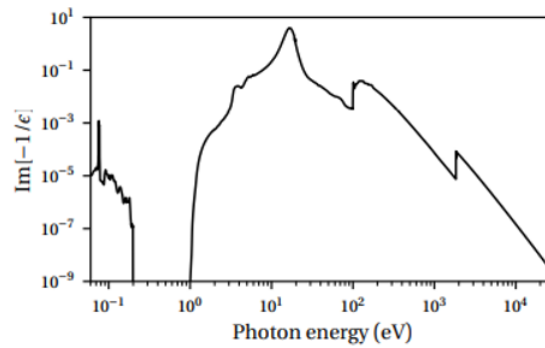


Figure 1.24: Energy loss function of silicon at different photon energy [60]

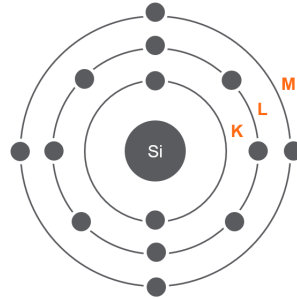


Figure 1.25: Electronic structure of silicon

Table 1.3: Electron binding energy of different shells in silicon [13]

	K1s	L ₁ 2s	L ₂ 2p _{1/2}	L ₃ 2P _{3/2}
Electron binding energy (eV)	1839	149.7	99.82	99.42

1.5.2. Elastic and Inelastic Scattering Events

Nebula [60], a Monte Carlo simulator designed to model electron-matter interactions, encompasses several fundamental types of scattering events. Figure 1.26 shows the flow chart of the interactions of charged particles with matter under EUV exposure in Nebula.

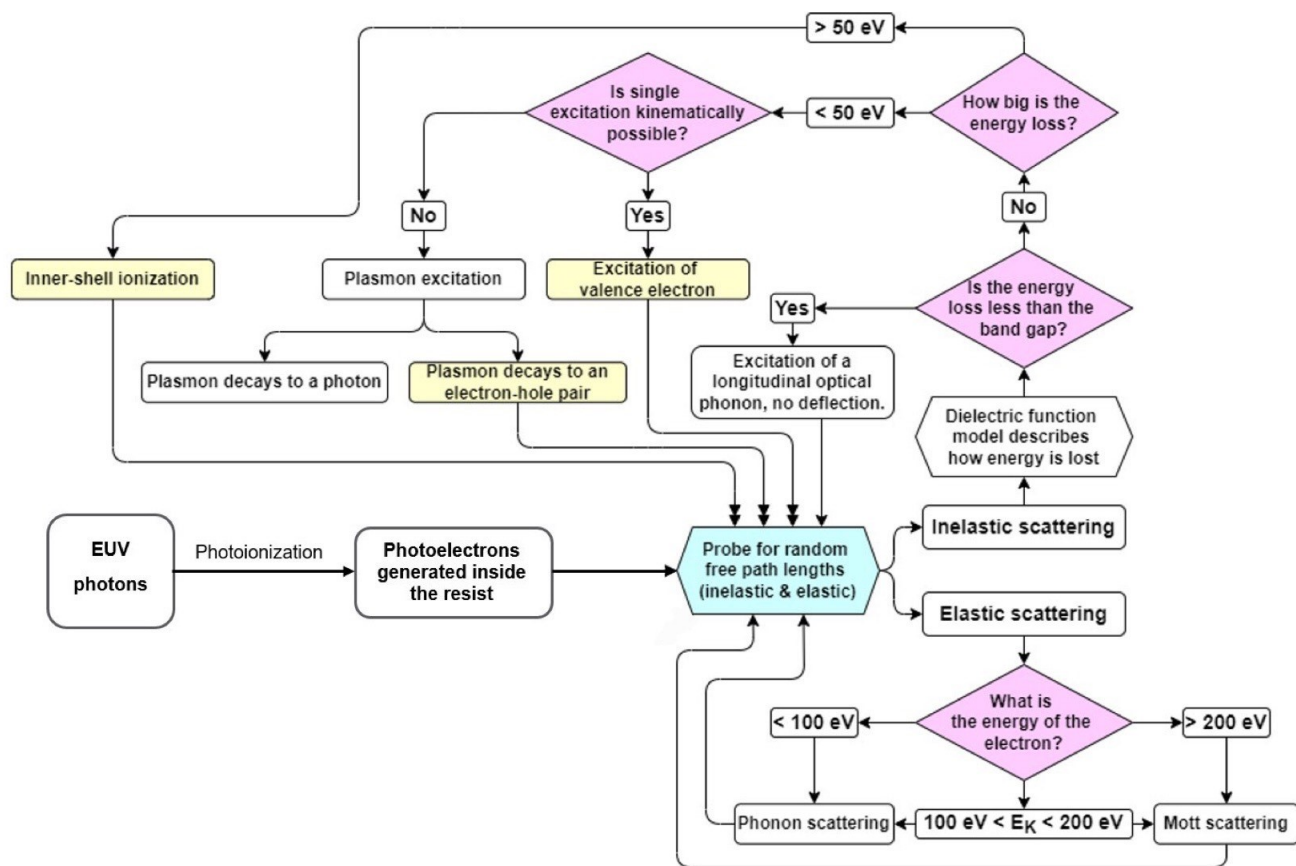


Figure 1.26: The flow of process for EUV exposure simulation in Nebula

When the resist is bombarded with EUV photons, photoionization is induced, leading to the generation of photoelectrons within the resist. These photoelectrons undergo random free path lengths, as depicted in the blue box in Figure 1.26. Elastic scattering, characterized by no energy loss during the scattering process, is addressed through the utilization of the Mott scattering model for electrons with energies exceeding 200 eV, while phonon scattering is employed for electrons with energies below 100 eV [40], with interpolation applied for energies falling between these thresholds. Mott scattering involves the interaction of a charged particle, typically an electron, with a target atom through electromagnetic force. Consequently, the atom experiences a recoil force, resulting in a minor transfer of energy from the electron to the atom. However, the amount of energy transfer can be ignored, given the atom's significantly greater mass compared to that of an electron. Mott scattering, which involves minimal kinetic energy changes when electrons are deflected by an atom, is therefore considered elastic scattering. However, for electrons with energy lower than 100 eV, the elastic mean free path is approximately 1 to 2 Å, comparable to interatomic distances. Consequently, these low-energy electrons behave more like Bloch electrons with quantized energy dispersion, indicating that they are not entirely free but rather constrained within a periodic potential [61]. Therefore, it is more appropriate to apply phonon scattering for electrons with lower energy.

Inelastic scattering in materials involves the transfer of energy from an incident particle

to the material, leading to various excitations within the material. One common outcome of inelastic scattering is the generation of secondary electrons. The process can be characterized by the loss of energy, which is often described using the dielectric function model. When the energy loss is less than the band gap of the material, one common excitation is the generation of longitudinal optical phonons, as described in section 1.5.1. However, when the energy loss exceeds the band gap, additional possibilities arise. An energy threshold of 50 eV is often used in Nebula as a criterion to distinguish between inner shell and outer shell.

If the energy loss is greater than 50 eV and is sufficient to overcome the minimum inner shell binding energy, then the inner shell excitation occurs, where an electron transitions from an inner shell to a higher energy level. For example, as shown in Table 1.24, the minimum binding energy of an inner shell of Si is 99.42 eV in L shell. Therefore, if the energy loss is 60 eV, even though it is over 50 eV, it still not enough to trigger the inner shell excitation. Consequently, an outer shell excitation will be chosen. If the energy loss is less than 50 eV, the specific excitation mechanism depends on kinetic considerations. If single excitation is kinetically favorable, the valence electron may be excited to a higher energy level. However, if single excitation is not energetically favorable, plasmon excitation may occur instead. After plasmon excitation, subsequent processes may occur, such as decay into photons or the generation of an electron-hole pair. Overall, inelastic scattering events involve significant energy transfer and can lead to the generation of secondary electrons.

1.5.3. Secondary Electron Yield

Secondary electron is an electron which originally occupies a bound state in the atom but is kicked out by the incoming electron or photon with sufficiently high energy, as depicted in Figure 1.27 [77].

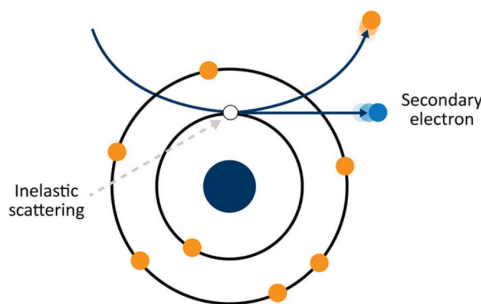


Figure 1.27: SE generation [77]

SEs produced through inelastic scattering events within the resist are the main driver of acid reaction in CAR [50] and dissociating ligands in MOR [85]. Therefore, assuming there are enough molecules for SE to do the chemistry in the resist, increasing secondary electron yield can be important to reach the full potential of each EUV exposure and make the manufacturing process more cost-effective. However, it is important to note that these secondary electrons must be within a controlled interaction volume so that the resulting electron-induced chemical reactions will not be detrimental to the pattern resolution [48]. In Nebula, three possibilities of secondary electron generation are included in the simulator, which are direct excitation of a valence electron, excitation via plasmon decay and inner-shell ionization as described in section 1.5.2.

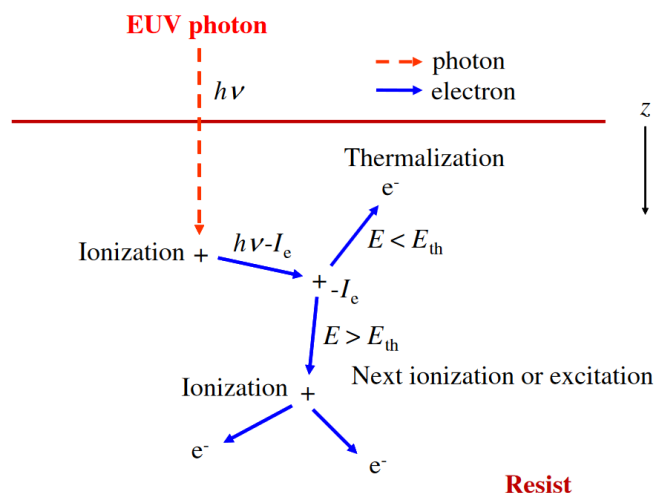


Figure 1.28: Illustration of the interaction between EUV photon and resist [64]

Figure 1.28 illustrated the interaction between EUV photon and resist. Ionization refers to the process where an electron is removed from an atom or molecule, resulting in the formation of positively charged ions within the resist material. Thermalization is the process by which the energy from the initial interaction (i.e. absorption of EUV photons) is redistributed among the particles in the material, leading to an increase in temperature [64]. The photoelectrons generated from EUV photon might trigger further ionization and excitation, which produces more secondary electrons. Thus, a photon can generate multiple secondary electrons. In a numeric model developed by Hinsberg et al., around 6 to 9 electrons will be generated per photon for an Inpria MOR, as shown in Figure 1.29. A best fit obtained with the experimental data is 8 electrons per photon [54]. Another simulation done by software PROLITH X6.0 shows the electron yield is around 6.5 per photon, for kinetic energy of the electrons larger than 2 eV [83].

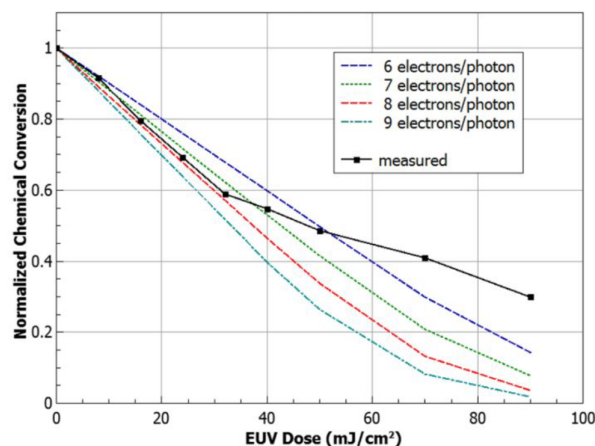


Figure 1.29: Calculated and measured extents of conversion versus EUV dose for an experimental Inpria MOx resist. The solid black line and square points represent experimentally measured values [54]

1.5.4. Inelastic Mean Free Path

Mean free path (λ) is an average distance the particle travel before the next scattering event and it is dependent of the energy loss and momentum transfer of the particle. As only inelastic scattering events are able to generate secondary electrons that can do the

chemistry in the resist, this section will focus on the inelastic mean free path. An inverse mean free path for inelastic scattering is shown in Equation 1.14.

$$\lambda^{-1} = \frac{\hbar}{\pi a_0 T} \frac{(1 + \frac{T}{2mc^2})^2}{1 + \frac{T}{2mc^2}} \int d\omega \int \frac{dq}{q} \text{Im}[\frac{-1}{\epsilon(q, \omega)}] \quad (1.14)$$

where a_0 is the Bohr radius, T is the electron's kinetic energy, q is wave factor in Fourier space (related to the momentum transfer from the primary to the secondary electron) and ω is the frequency in Fourier space (related to the total energy loss for the primary electron). The imaginary part is ELF we mentioned in section 1.5.1 and it is the dielectric function inside is related to the optical properties of the material. In the integration part, both the energy loss and momentum transfer is limited to the kinetic energy of the electron, as presented in Equation 1.15 and Equation 1.16 [60]. T' is the kinetic energy of the particle after the inelastic scattering event, which is equal to $T - \omega$.

$$0 \leq \hbar\omega \leq T \quad (1.15)$$

$$\frac{q_{\pm}}{2m} = \sqrt{T(1 + \frac{T}{2mc^2})} \pm \sqrt{T'(1 + \frac{T'}{2mc^2})} \quad (1.16)$$

Mean free path is an important performance metric for secondary electrons, because the extending of mean free path will affect the blur and the resolution of the pattern in lithography. In organic resist, the inelastic mean free path of secondary electron under EUV exposure is in around 1 to 2 nanometers [97, 37]. As shown in Figure 1.30, the trajectories of secondary electrons are distributed narrowly around the photoabsorption point.

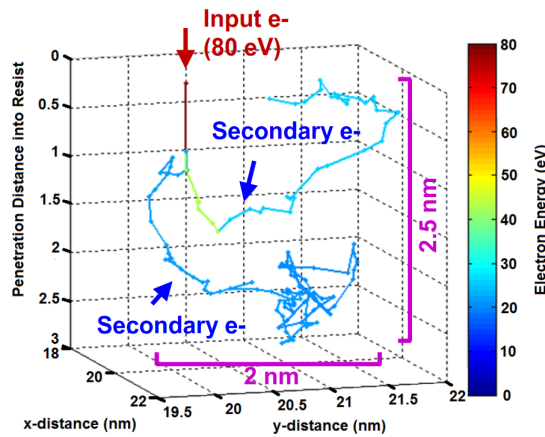


Figure 1.30: Secondary electron trajectories simulation under EUV exposure [98]

1.5.5. Resist Blur

Definition of Resist Blur

Resist blur is the maximum distance from a photon absorption event where electrons cause solubility changes, representing the sphere of influence of the event [9]. Acid diffusion blur and secondary electron blur (SEB) are the two main root causes of resist

Table 1.4: Resist blur for different types of resist and lithography light sources

Lithography light source		DUV	EUV	
Type of resist		CAR	CAR	MOR
Resist blur	Acid diffusion blur	Yes	Yes	No
	Secondary electron blur	No	Yes	Yes

blur. However, with different types of resist under different lithography light sources, the resist blur mechanisms can be varied, as shown in Table 1.4.

Under DUV exposure, CAR has only acid diffusion, because the energy of DUV is not high enough to induce SE generation [43]. For EUV lithography, in addition to the acid diffusion, secondary electrons can contribute to the blurriness for CAR as well. However, the effect of acid diffusion is believed to be larger than SEB, because acid diffusion length (around 7 nm [32]) is normally longer than electron scattering distance (around 1 to 3 nm)[33]. As for MOR, secondary electron is the leading reason for the resist blur under EUV exposure. According to the simulation done by Vaglio et al. from KLA, under EUV exposure, an average electron blur of Inpria MOR is 1.1 nm, while organic CAR has an average electron blur of 1.5 nm [83]. Table 1.5.5 shows the benchmark of SEB of MOR and CAR. In general, the blur size of MOR is slightly smaller than CAR.

Table 1.5: Benchmark of secondary electron blur size of MOR and CAR

	MOR		CAR	
Electron blur	1.1 nm	1.74 nm	1.5 nm	2.5 nm
Maximum blur distance	6 nm	5.5 nm	10 nm	no data
Method	simulation calibrated with experiment			
Reference	[83]	[92]	[83]	[36]

Blur Effects on Pattern Quality

Resist blur has two competing effects: Firstly, it reduces the aerial image contrast. As shown in Figure 1.31, excessive blur can lead to distortion and imprecision in pattern transfer, resulting in deviation from the desired design specifications. $I(x)$ represents the aerial image intensity, x is the x -axis position and p stands for the period of light wave [3]. The standard deviation of a Gaussian distribution σ is used as a conventional symbol of blur length [109]. Secondly, blur can help to increase the photon counting volume, and thus mitigate the photon shot noise problem, which was described in section 1.2.1. With larger blur range around the absorbed photon, more photons can contribute to the dissolution change of each piece of resist, as depicted in Figure 1.32.

Therefore, a trade-off between these two effects has to be made and an optimal blur is required to obtain the best pattern performance. LCDU (Local Critical Dimension Uniformity) stands for local variations and can be used to quantify the pattern performance. The lower LCDU is desired to produce better pattern quality. As presented in Figure 1.33, if the blur is too high, then LCDU will increase because the first effect is dominating. However, if the blur is too low, then the issue of photon shot noise will become more

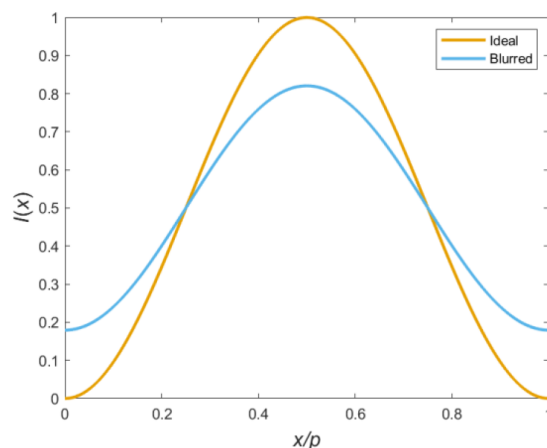


Figure 1.31: Ideal and Gaussian blurred sinusoidal aerial image obtained with EUV interference lithography [3]

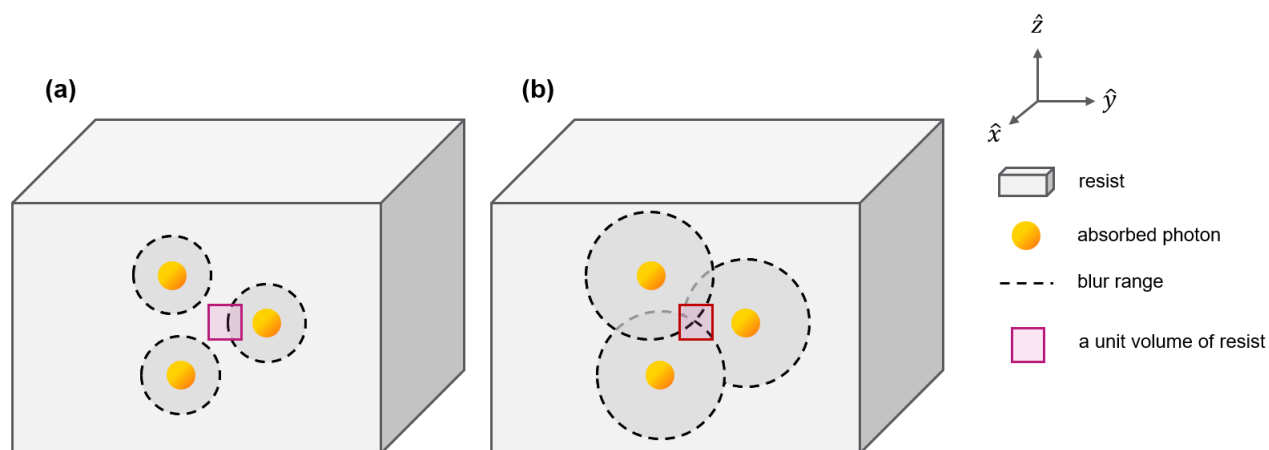


Figure 1.32: Larger blur can increase the photon counting volume (a) Small blur: only one photon contributes to the chemistry in the unit volume of resist (b) Large blur: three photons can contribute to the chemistry in the unit volume of resist

evident, which results in high local variations. The optimum blur is dependent of the half-pitch size (i.e. CD). In the study done by Yildirim et al., the optimum blur size to achieve best LCDU was found in between 20% to 33.3% CD [109]. In another research conducted by Mack et al., they concluded that the optimum blur might be in the range of 16% to 50% of the minimum CD [72].

Anisotropic Blur

It is worth mentioning that blur can be isotropic or anisotropic [44], as illustrated in Figure 1.34. Increasing the blur parallel to the resist surface (i.e. x and y directions) might degrade the pattern contrast. However, if blur along x and y directions are kept as constant, enhancing the the blur perpendicular to the surface (i.e. z direction) will be beneficial to achieve larger photon counting volume without sacrificing the optical contrast.

A research done by Long et al. has found that with increased blur in the z direction, an improved pattern uniformity and lower dose-to-size can be achieved without the

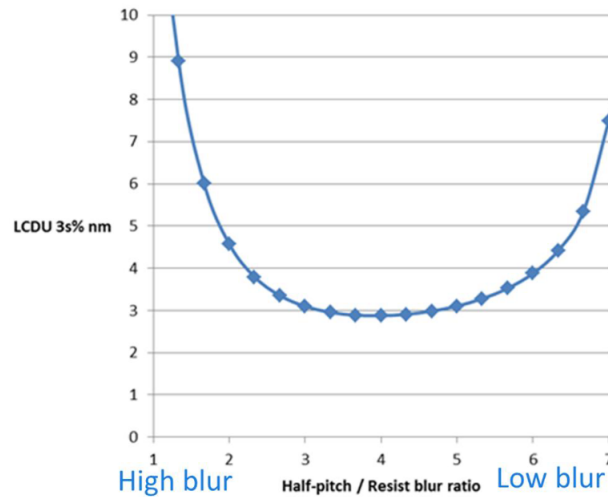


Figure 1.33: Optimal blur is pitch dependent [109].

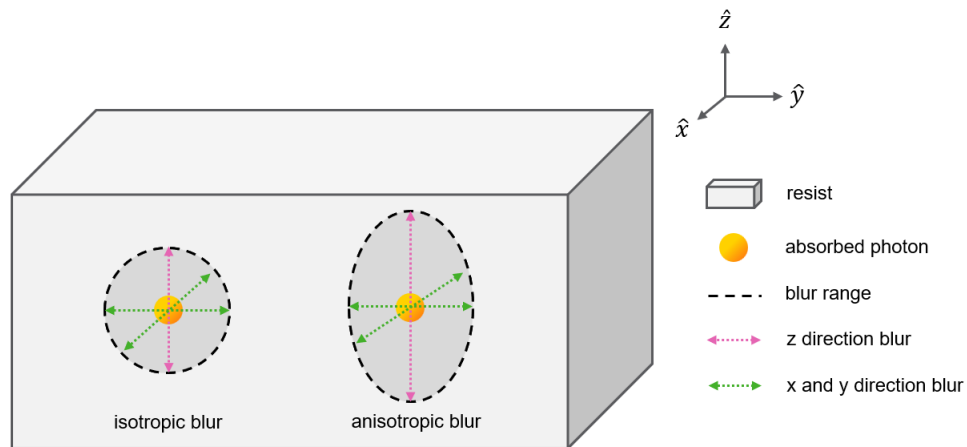


Figure 1.34: Illustration of isotropic blur and anisotropic blur

loss of resolution. Figure 1.35 shows that higher z direction blur cause higher mean CD value and narrower CD distribution. To print the same CD size, lower dose is needed for higher z direction blur, as shown in Figure 1.36 (a). Dose-to-size means the amount of exposure energy needed to produce the required feature size. Lower dose-to-size is more cost-efficient for mass manufacturing [69]. As presented in Figure 1.36 (b), with increasing z blur, the dose-to-size is reducing.

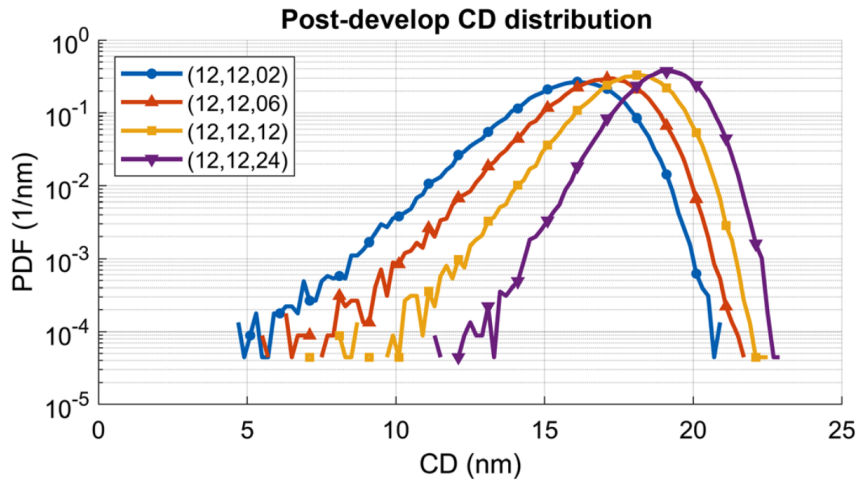


Figure 1.35: Contact CD distribution using the Mack development model [69].

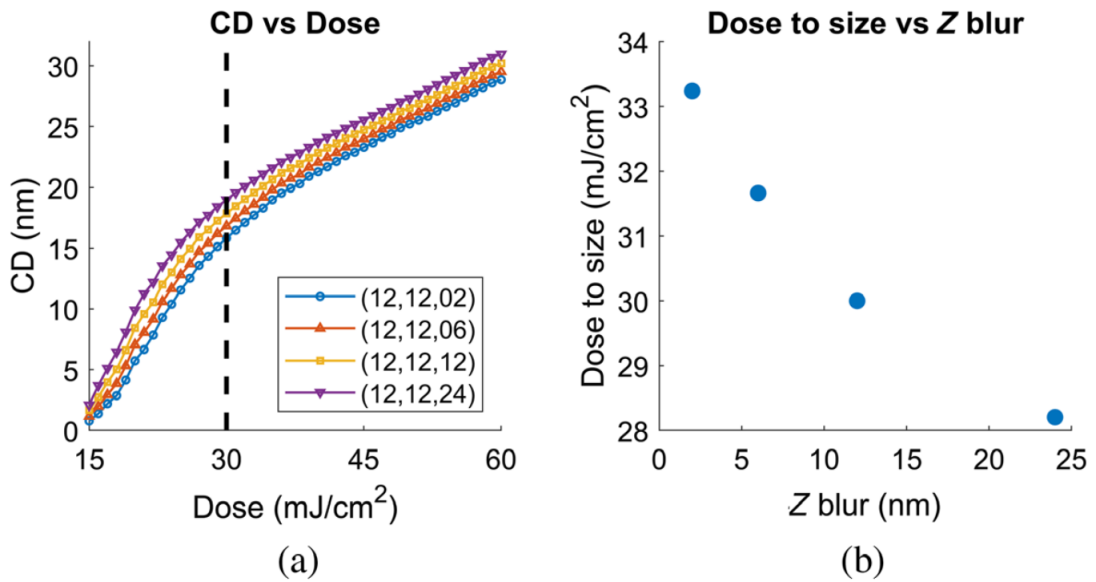


Figure 1.36: (a) CD versus dose response and (b) corresponding dose to size for the different z-blur resist models [69].

1.6. Problem Statement

What Do We Already Know?

EUV lithography is essential for advanced semiconductor manufacturing (section 1.2.1). MOR has shown potential as resist materials for EUV lithography, especially for high NA EUV (section 1.3.3). To enhance computer chip performance, improving pattern quality and reducing LER are crucial (section 1.3.1). While increasing the EUV dose can reduce LER, it is extremely expensive.

What Is the Problem?

Is there a way to increase pattern performance without increasing the EUV dose? Pattern performance might be improved by reducing LER or mitigating the problem of photon shot noise.

Why Does It Matter?

Improving pattern quality without increasing EUV dose can enhance computer chip performance cost-effectively and support the continuation of Moore's law.

Objective of the Project

This project will address the problem with a focus on:

1. Create anisotropic blur extended in the z direction while maintaining or reducing blur in the x and y directions.
2. Increase secondary electron yield with sufficient energy to perform the chemistry within the resist.

In Chapter 2, the research methodology addressing this problem will be proposed. Chapter 3 will present, analyze, and discuss the simulation results. Chapter 4 will answer the research question listed in this section and summarize the project's potential impact. Finally, Chapter 5 will outline simulation limitations and suggest future work prospects.

2

Methodology and Materials

2.1. Photoresist Materials: MOR and PMMA

This project analyzes two types of photoresist materials: MOR (produced by Inpria) and PMMA. The chemical formula for MOR is approximately $C_{46}H_{116}O_{22}Sn_{12}$ (the vendor didn't disclose the exact formula) and for PMMA is $C_5H_8O_2$. PMMA is used to mimic the behavior of CAR, because most vendors producing commercial CAR are very strict with the intellectual property and thus we have no access to the CAR material properties. The details of materials properties are shown in Appendix A.

2.1.1. Optical Properties

Figure 2.1 shows the ELF of MOR and PMMA at different photon energy.

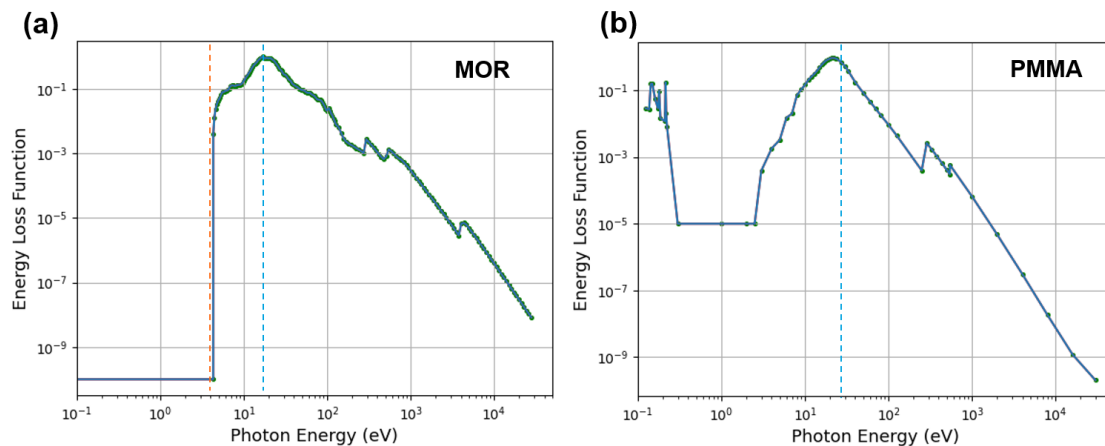


Figure 2.1: ELF with zero momentum of MOR and PMMA (Orange dashed line: band gap of MOR, Blue dashed lines: plasmon frequency)

As discussed in section 1.5.1, the photon has no rest mass but has a very small momentum, thus the dielectric function used in ELF here can be regarded as zero momentum. A free electron gas model will be fit with it to extend it to non-zero momentum. Although the free electron gas model is typically used for metals due to their high density of free electrons, it has also been found to work well for insulators. For instance, plasmons, which are collective oscillations of many valence electrons, exist in non-crystalline insulators and can be described by this model. These valence electrons can behave

like a free electron gas. Especially for polymer embedded with metallic nanoparticle, the plasmons are more likely to be induced, because the localized surface plasmon brought by the metallic nanoparticle [81]. While the free electron gas model is indeed less applicable to polymers than to metals, it remains the best approximation available for the simulation.

For MOR, the bandgap value is around 4 eV, as indicated with the orange dashed line in Figure 2.1 (a), where the forbidden region starts, and no energy loss is observed. The bandgap value for PMMA is 5.6 eV, which can be found in the literature [51], thus is not approximated from the optical data. These optical properties and the resulting ELF will be used to calculate the inelastic mean free path, as detailed in section 1.5.4. Most solid materials have a plasmon frequency in the range of 10 to 100 eV, corresponding to the largest energy loss observed in the plots.

2.1.2. Mean Free Path and Kinetic Energy

Elastic and inelastic mean free paths determine the likelihood of scattering events and the travel distance of electrons. The mean free path is dependent on the kinetic energy of the electron. Figure 2.2 shows the relationship between mean free path and kinetic energy for both MOR and PMMA. It is interesting to note that the inelastic mean free path follows a universal curve across all materials. At very low energies, electrons do not easily induce excitations, resulting in a long mean free path. At very high energies, the mean free path increases because the electrons move too quickly for the electrons in the stationary atoms to be excited. In the intermediate range of kinetic energy, electrons can readily lose energy through electronic excitation, resulting in a minimum mean free path that approximately corresponds to the plasmon frequency, as the peak ELF shown in Figure 2.1. The kinetic energy with the minimum mean free path is not exactly correspond to the plasmon frequency in optical data. This is because, when plasmon resonance extends to non-zero momentum, the electron cannot lose energy without also losing momentum. As a result, the plasmon energy increases at non-zero momentum. Therefore, electrons must have slightly higher energy at non-zero momentum to excite plasmons compared to the energy required at zero momentum.

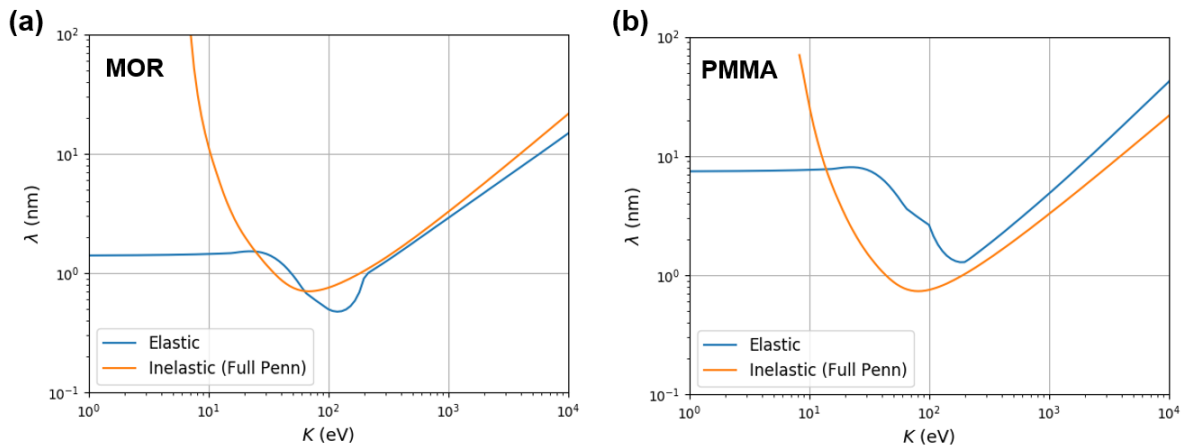


Figure 2.2: Mean free path of MOR and PMMA (Elastic: hybrid model of Mott scattering for high energy and phonon scattering for low energy, Inelastic: full Penn model)

The full Penn algorithm [82] is used in Nebula to calculate the inelastic mean free path by combining the optical data of materials presented in section 2.1.1. For elastic scattering,

Nebula uses a hybrid model. As shown in Figure 1.26, Mott scattering is used for high energies over 200 eV, and phonon scattering is used for energies below 100 eV, with interpolation applied in between. The physical mechanisms are detailed in section 1.5.2.

As presented in Appendix A.1 and A.3, four phonon related parameters are specified: lattice constant, acoustic deformation potential, and speeds of sound for longitudinal and transverse phonons. Firstly, the lattice constant sets a scale for the phonon wavelengths that can propagate through the material. Shorter lattice constants correspond to higher-frequency phonons. Secondly, the acoustic deformation potential quantifies how electronic energy levels shift due to lattice vibrations (i.e., phonons), influencing phonon scattering rates. Higher deformation potentials indicate stronger scattering effects and thus smaller elastic mean free path. Lastly, the speeds of sound for longitudinal and transverse phonons describe how quickly vibrational waves travel through the material. These speeds are linked to the material's elastic constants, which characterize its response to mechanical stress and strain.

In this project, some of the phonon parameters of MOR are set to the same as PMMA, as we don't have phonon properties of MOR and it is also very challenging to measure it empirically. This is technically not accurate, but it is the best we can have for now. The lattice constants of MOR and PMMA are set to C-C bond length of 1.54 Å, as C-C bonds are the structural backbone for these two materials. The speeds of sound of MOR are copied from PMMA. The acoustic deformation potentials are tuned for both materials to obtain the reasonable electron blur sizes that are in agreement with literature. A more detail comparison of electron blur sizes will be elaborated in section 3.4. While this is not technically accurate, it might be a better approximation than applying Mott scattering across all energy ranges. In section 3.9, we will discuss how the simulation results are varied with Mott scattering and phonon scattering mechanism applied for energy below 100 eV region.

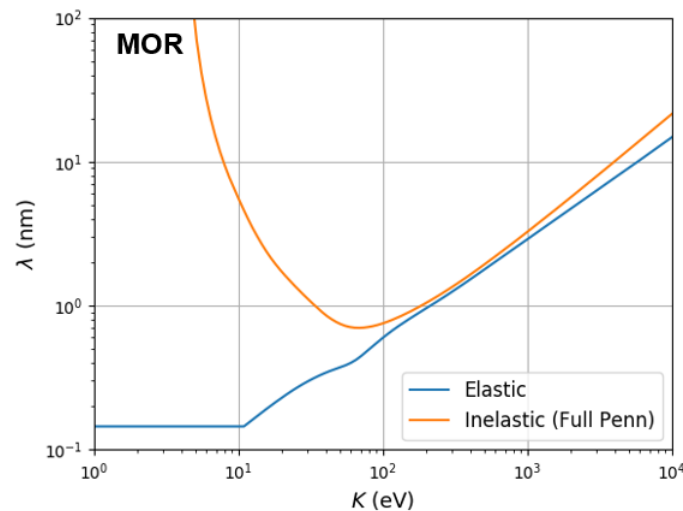


Figure 2.3: Mean free path of MOR (Elastic: Mott scattering for both high energy and low energy, Inelastic: full Penn model)

Figure 2.3 illustrates that applying Mott scattering to low energy ranges results in an elastic mean free path significantly shorter than the inelastic mean free path, indicating that elastic scattering events would be much more likely than inelastic one below 100 eV. As can be seen in Figure 2.3, the elastic mean free path is near to 1 to 2 Å, which means

electron is bouncing off almost every atom it encounters.

2.1.3. Electronic Band Structure

In solid state physics, electrons can be described using band theory, which allows for electron energy levels within specific ranges. As illustrated in Figure 2.4, when the interatomic distance is very large (i.e., for isolated atoms), electrons occupy separate orbitals. However, as atoms come closer together and the interatomic distance decreases, as in solid-state materials, these discrete energy levels start to form continuous bands. In Nebula, a simplified band structure is employed.

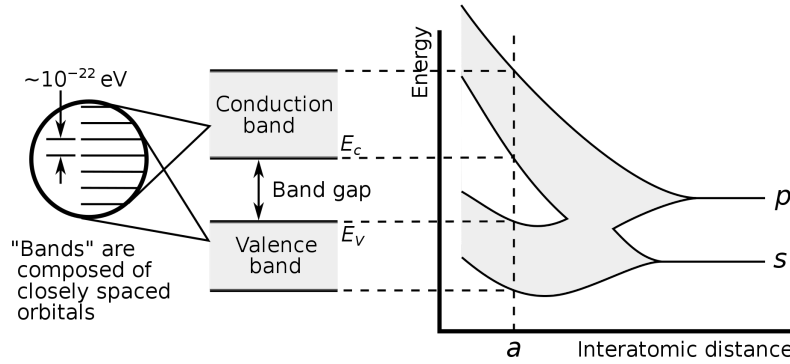


Figure 2.4: Electronic band structure in solid state [19]

Figure 2.5 depicts the band structures of MOR and PMMA. The band gap values for MOR and PMMA are derived from optical data and literature values respectively, as described in section 2.1.1. The electron affinity is set to 1.13 eV for MOR [71] and 2.5 eV for PMMA [88]. Regarding the valence band width, no reliable values were found in the literature. Additionally, the ab initio values calculated by DFT are often underestimated because electrons are not uniformly distributed in the material, and DFT often underestimate orbital overlap behaviors. Nevertheless, setting the valence band width to zero is not accurate as it would affect the momentum transfer parameters during the single excitation mechanism in Nebula.

In the single excitation event, the primary electron will transfer energy $\hbar\omega$ and momentum $\hbar q$ to a valence electron. The energy of valence electron before and after the event are shown in Equation 2.1 and Equation 2.2 respectively. The momentum transfer parameter q in Nebula is chosen to be oriented along z axis without loss of generality [60].

$$E_i = \frac{\hbar^2 k_i^2}{2m} = \frac{\hbar^2 (k_x^2 + k_y^2 + k_z^2)}{2m} \quad (2.1)$$

$$E_f = E_i + \hbar\omega = \frac{\hbar^2 k_f^2}{2m} = \frac{\hbar^2 (k_x^2 + k_y^2 + (k_z + q)^2)}{2m} \quad (2.2)$$

As the initial energy of the valence electron (E_i) is smaller than the valence band width and the energy after excitation will be larger than the valence band width (V) plus band gap (G), the values of k_x and k_y are constrained to a ring as shown in Equation 2.3.

$$\frac{2m(V + G)}{\hbar^2} - (k_z + q)^2 < k_x^2 + k_y^2 < \frac{2mV}{\hbar^2} - k_z^2 \quad (2.3)$$

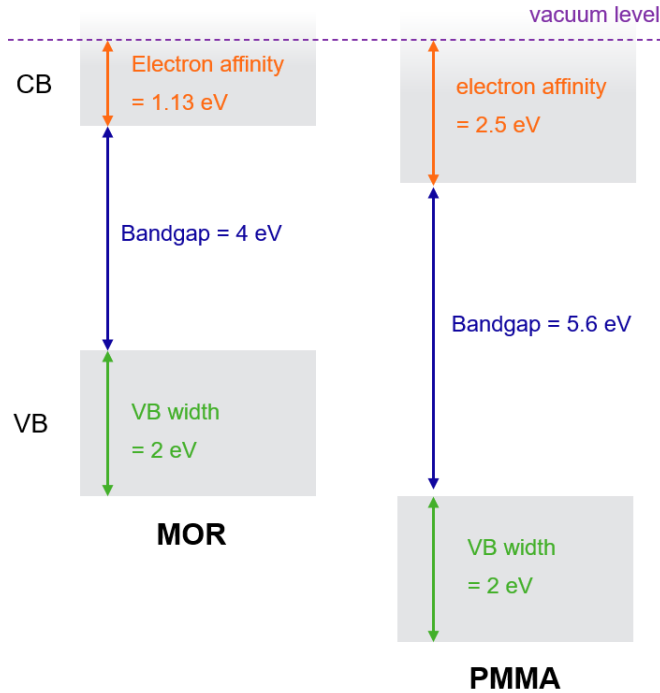


Figure 2.5: Band structure of MOR and PMMA

It is evident that the range limit varies significantly when the valence band width is set from 0 eV to 2 eV, whereas the difference is less evident between 2 eV and other non-zero values. Therefore, we chose a non-zero value of 2 eV for both materials, as most valence band widths for polymers range from 2 to 10 eV or more and the distribution of valence electron is not evenly spread across the entire energy range [89] [74]. The influence of valence band width on the simulation results will be discussed in section 3.7.

2.2. Nebula Settings Changes

Nebula is an open source electron scattering simulator with an original intention to study electron scattering in materials exposed to electron irradiation from scanning electron microscope (SEM). However, in this project, we are investigating the interaction between EUV exposure and photoresist materials with a focus on MOR. Therefore, a few modifications need to be made in Nebula source code to better suit the specific use case of this project.

As Nebula is embedded with multi-CPU calculation, it is useful to run the simulation on High Performance Cluster (HPC) to speed up the computation time. The effect of computational resource is shown in Appendix A.

2.2.1. Photoelectron Generation Methods

Instead of starting the electrons in the vacuum for SEM use case, in this study we generate primary photoelectrons directly inside the material. The physics mechanism of photoelectron generation was discussed in section 1.4. Table 2.1 summarizes the photoelectron generation methods in this project. In this section, we will explain how the starting position, direction and energy of the photoelectrons are chosen and justify each choice.

Table 2.1: Summary of photoelectron generation methods

	Description	Symbol	Sampling method
Photoelectron	position	x	Finite area exposure (Gaussian distribution with $2\sigma = 15nm$)
		y	
		z	Beer-Lambert law
	direction	dx	Isotropic
		dy	
		dz	
starting energy	E	Cross-section based photoionization method developed by Sivakumar [93]	

Position

In the Nebula simulator, each electron has its own coordinates (x, y, z) . The starting position of the photoelectrons can be divided into two parts. The first part is the x and y position, which depends on the exposure type of EUV light. The second part is the z position (i.e., depth), which is sampled randomly according to the Beer-Lambert law.

For the first part, at the beginning of this project, point beam exposure is used for simplicity. This means all photoelectrons are generated with $x = 0$ and $y = 0$. However, in reality, EUV photons distribution in the light source is not a point beam, but covers a finite area with a Gaussian distribution. As shown in Figure 2.6, only the volume that has enough absorbed photons and the subsequent electron cascade can induce desired chemistry changes and display the clear pattern after development.

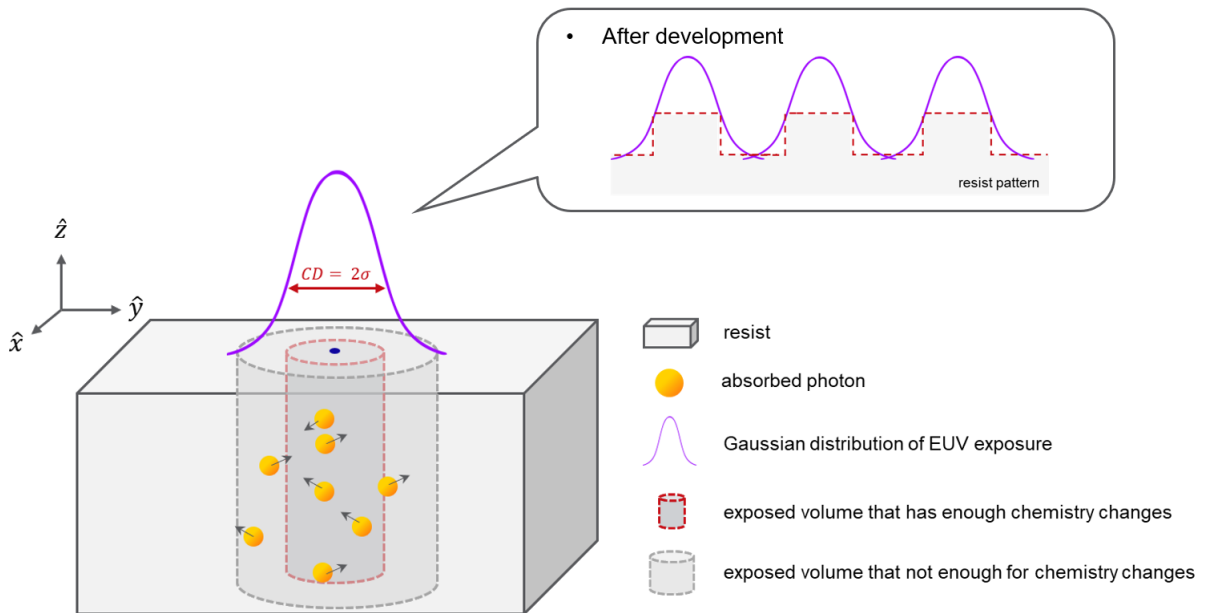


Figure 2.6: Finite area exposure and solubility changes

One of the initial applications of high NA EUV is anticipated to be a grid of holes with a pitch of approximately 30 nm. In this project, we approximate this grid as a single

Gaussian spot with a 2-sigma diameter of 15 nm. Therefore, the x and y position of photoelectrons are sampled from Gaussian distribution with a standard deviation of 7.5 nm, as demonstrated in Figure 2.7.

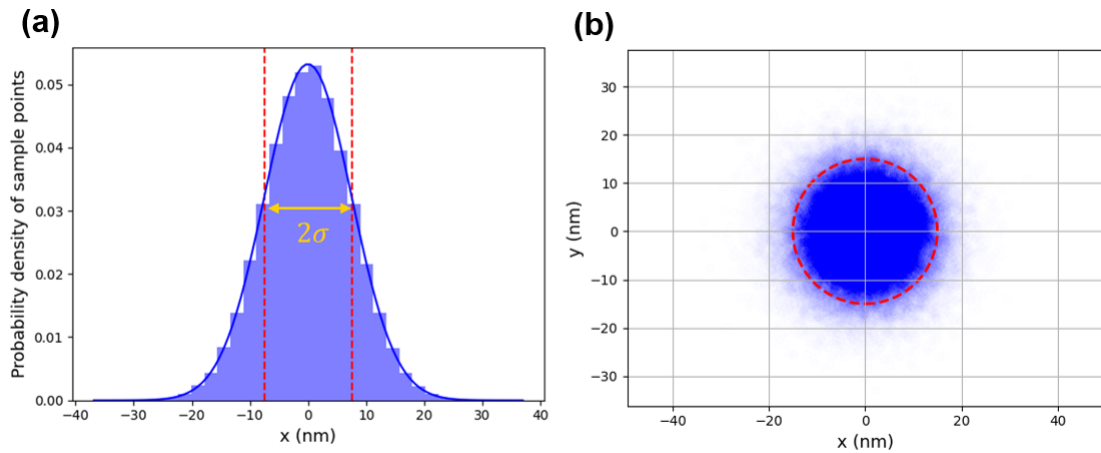


Figure 2.7: (a) Histogram of sampling points along x-axis (b) x-y plane cross section

After determining the x and y positions of the photoelectrons, the z position needs to be finalized. The generation depth of a photoelectron is determined by Beer-Lambert law, which describes the probability distribution for an electron to travel a certain path without scattering, as shown in Equation 2.4. Here, z is the depth of the photoelectron and λ is the absorption length of the materials. Absorption length, also known as attenuation length, is the distance where the intensity of beam has been dropped to $\frac{1}{e} \approx 36.79\%$. The absorption length is an experimental value that depends on the material and the photon energy. This value can be found in literature or Center for X-Ray Optics (CXRO) website [31]. In this research, the absorption length of MOR under EUV exposure is set to 54.34 nm [31], and 190 nm for PMMA [52].

$$p(z) = \frac{1}{\lambda} e^{-\frac{z}{\lambda}} \quad (2.4)$$

To draw a random path from the probability distribution $p(z)$, Equation 2.5 is used:

$$z = -\lambda \ln(r) \quad (2.5)$$

Where r is a random value sampled from a uniformly distributed interval (0,1]. For example, if we sample 100000 depth values, the distribution will follow the Beer-Lambert law as shown in Figure 2.8.

Figure 2.9 compares the interaction volume plots of point exposure and finite area exposure with a Gaussian distribution. Figure 2.9 (a) shows when the point exposure is applied, most scattering events happen around the origin and a clear boundary can be seen, which is not physically correct. Figure 2.9 (b) better mimics the real scenario in EUV exposure. The red dot lines indicate one standard deviation of 7.5 nm from the origin, which corresponds to the expected pattern edge after development.

Direction

For the direction of photoelectrons, we chose to use isotropic sampling. It is widely known that individual atom and crystalline material exhibit a preferred angular distribution for

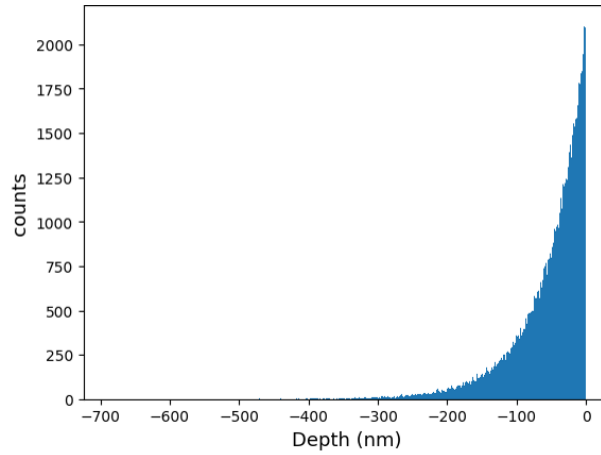


Figure 2.8: Photoelectron depth sampling for MOR with an absorption length = 54.34 nm

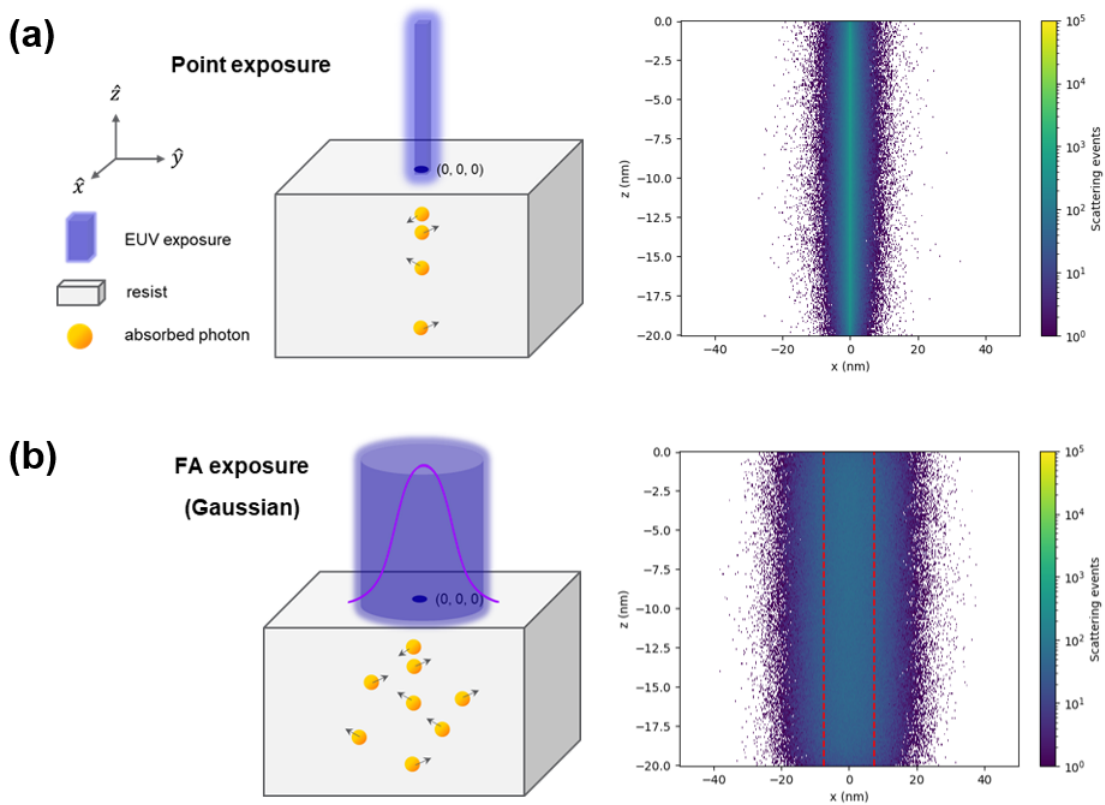


Figure 2.9: (a) Point exposure (b) Finite area exposure with Gaussian exposure of CD = 15 nm

photoelectron emission [24]. Interestingly, amorphous materials like MOR and PMMA may exhibit a preferred angular distribution as well [100][99]. However, it is difficult (or might be impossible) to simulate the exact angular distribution with the materials data we have now. Furthermore, since the electron cascade is dominated by secondary electrons, which are likely to have an isotropic distribution, the initial distribution of the photoelectrons has almost zero impact on the final result. Therefore, isotropic distribution sampling is used for photoelectron direction generation in this project.

Starting Energy

In most literature, the starting energy of photoelectrons is generally set to 80 eV for computing efficiency, as discussed in section 1.4. However, in a more physical point of view, the starting energy of photoelectrons should be varied depends on the material types and which electron is being ionized. Thus, to be more aligned with the real situation, we calculate the starting energy for different types of materials. The method is from chapter 11 of the textbook *Theory of Photo-electron emission from an X-Ray Interference Field* [101], and the implementation is developed by a previous ASML intern [93]. The main idea is to sample which electron to ionize based on their cross sections. An electron with a higher cross section will have higher probability to be ionized. In this way, the ionization energy is dependent on the molecular compositions and will not be a constant of 80 eV, as shown in Figure 2.10 (a) and (c). Note that the x-axis of Figure 2.10 (b) is binding energy. Thus, to get the starting energy of photoelectron, we need to subtract 92 eV EUV photon energy with the binding energy. The resulting photoelectron energy will be around 62 eV and 80 eV, which is correlated to our simulation results of MOR. The experimental data for CAR in Figure 2.10 (d) shows most photoelectron energy will be located at 75 to 80 eV, which also corresponds to the simulation results of PMMA. The correction of the starting energy of the photoelectrons is expected to make the entire simulation more close to the real scenario in lithography.

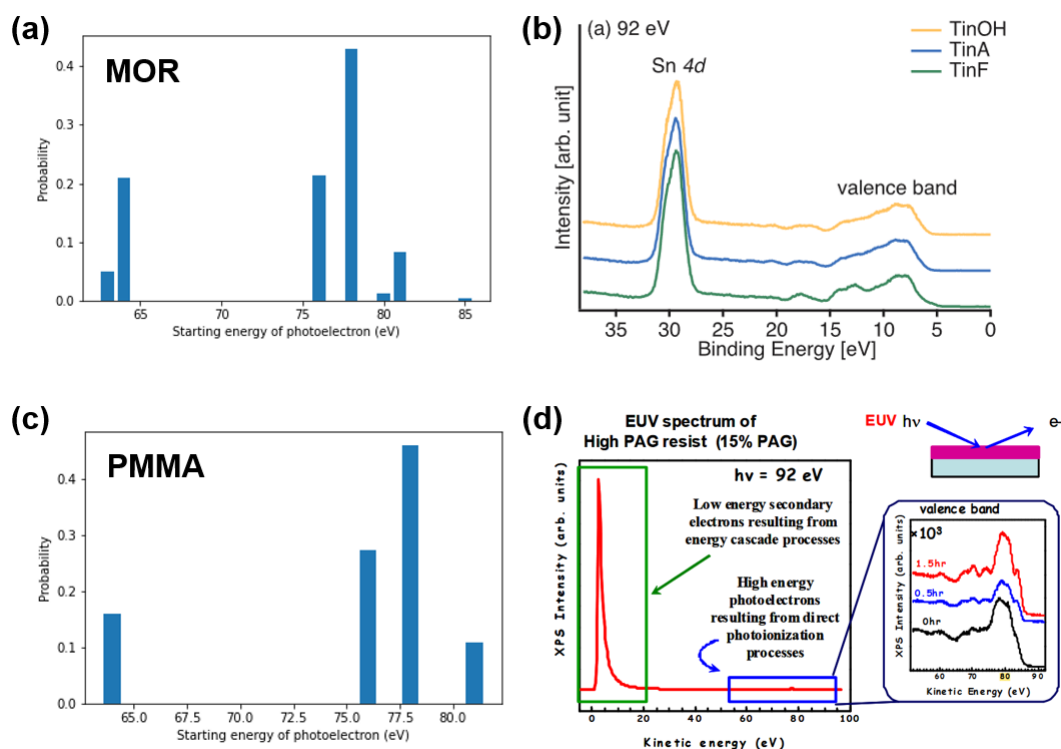


Figure 2.10: Comparison of simulation results and photoelectron spectroscopy experimental data from literature (a) our simulation results of MOR (b) experimental data for MOR [111] (c) our simulation results of PMMA (d) experimental data for CAR [14]

2.2.2. Energy Loss Filters

In Nebula, both elastic and inelastic scattering events are recorded. However, it is important to know that not every scattering event can help to do the chemistry in the

photoresist material. The energy loss filter can be tuned in Nebula to extract the types of scatterings we are interested in. Therefore, to prevent overestimating the number of useful scattering events, we firstly need to answer two questions:

1. Are electrons involved in the chemical reaction?
2. What is the minimum energy required for the secondary electron to do the chemistry?

For the first question, we have to dive into the chemical mechanism in resist materials. The detailed chemical mechanism of MOR has been shown in Figure 1.12. Now we are interested in Radiolysis stage, are electrons involved to dissociate ligands and create active sites. Figure 2.11 shows a simplified version of MOR mechanism. From the work done by CXRO and UC Berkeley [71], Sn-C bond cleavage is found to be the main contributor for the ligand dissociation in MOR, while butyl cleavage is the second. The chemical processes involved in creating active sites are impact ionization for Sn-C bond cleavage and electron attachment for butyl cleavage, where both processes are induced by electrons. As for CAR, the electrons are needed to react with PAG cation to produce acid [65].

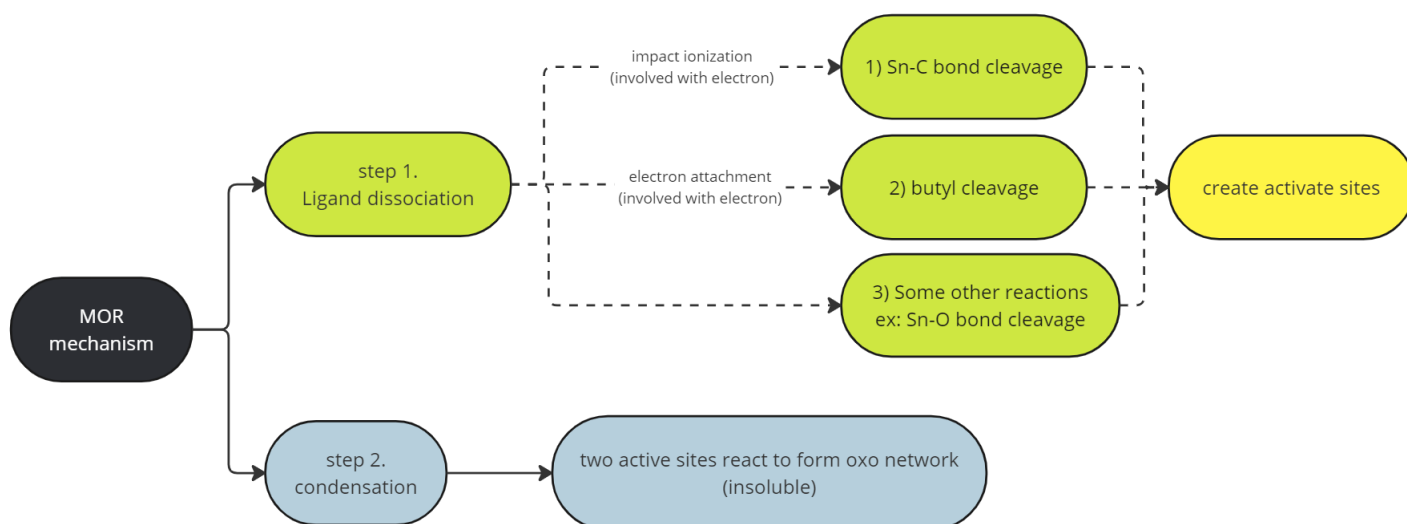


Figure 2.11: Chemical processes in ligand dissociation of MOR

After confirming that electrons are necessary for the chemical reactions, we return to the Nebula scattering mechanism. Figure 2.12 presents a simplified version of Figure 1.26 with a focus on which inelastic scattering events can generate SE. A detailed elaboration of how the energy loss is calculated is in section 1.5.1. Therefore, by setting the energy loss filter to be larger than the band gap of the material, we can isolate scattering events capable of generating electrons.

However, not every electron generated has sufficient energy to drive the chemical reactions. To answer the second question, we need to find the minimum energy required for these reactions in both MOR and PMMA to accurately identify the useful scattering events. According to the literature, the minimum energy required to induce chemical reactions via SE in MOR is 4.33 eV [9]. For CAR, the required energy varies depending on the PAG types, but the most literature agree that electrons with energy around 1 to 10 eV is necessary for the reactions. Consequently, as organized in Table 2.2, we set

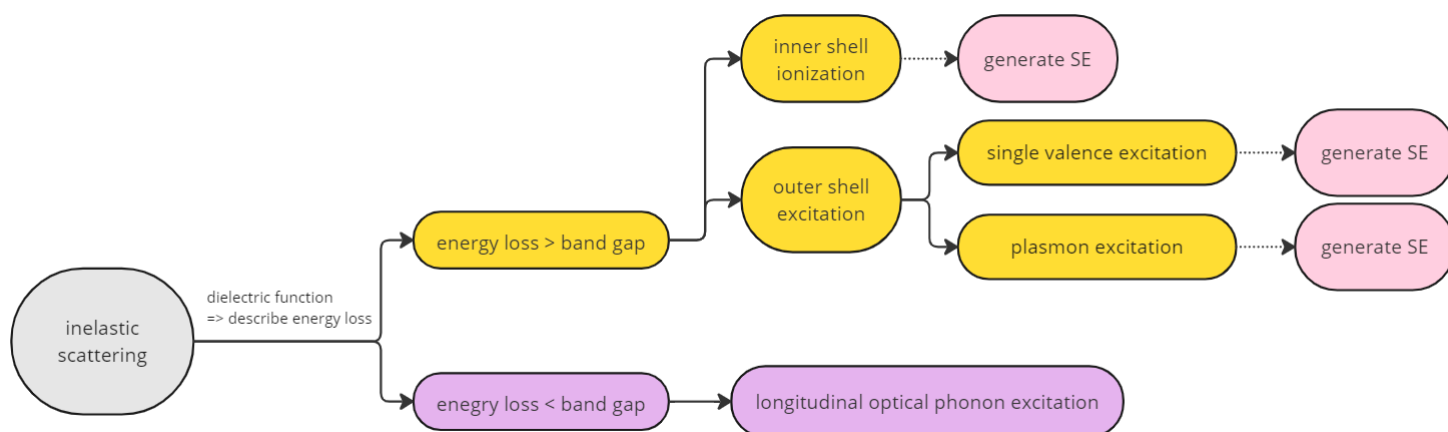


Figure 2.12: SE generation of inelastic scattering mechanism in Nebula

Table 2.2: Summary of energy loss filters of MOR and PMMA

		MOR	PMMA
Bandgap		4 eV	5.6 eV
Minimum energy delivered to SE to do the chemistry	Bandgap + 1 eV	5 eV	6.6 eV
	Literature value	4.33 eV [9]	The exact value depends on PAG types

the energy loss filter to 4.33 eV for MOR and 6.6 eV for PMMA, accounting for a 1 eV deduction from the SE energy for the chemical reaction. This ensures that we only count scattering events that impact the solubility properties of the photoresist materials.

2.2.3. Cut-off Energy to Stop Tracking Electrons

Electrons lose energy through scattering events, and Nebula stop tracking the electrons when their energy have dropped below a certain energy level, which is referred as the Cut-off Energy in this project. Originally, Nebula set the cut-off energy to the vacuum level, as in SEM applications, only electrons capable of escaping the material are of interest. However, in this study, we are interested in the behavior of electrons within the material, and those electrons in the conduction band might participate in the chemical reactions as well. Therefore, the cut-off energy is set to the bottom of the conduction band for this project purpose, as shown in Figure 2.13. This change affects the influence of the electric field because now more electrons are recorded, including some that might initially fall below the energy loss filter but gain energy from electric field afterwards and reach the energy levels necessary for chemical activity. More details on this will be discussed in Chapter 3.

2.2.4. Energy Threshold To Divide Inner and Outer Shell

In the original version of Nebula, the energy threshold that divides the inner shell and outer shell is set to 50 eV. This approach applies to most elements, but not for the Sn atom in MOR. As shown in Table 2.3, the Sn atom has its outermost inner shell in the N shell with a binding energy of 28 eV, which is lower than 50 eV. Therefore, for the Sn

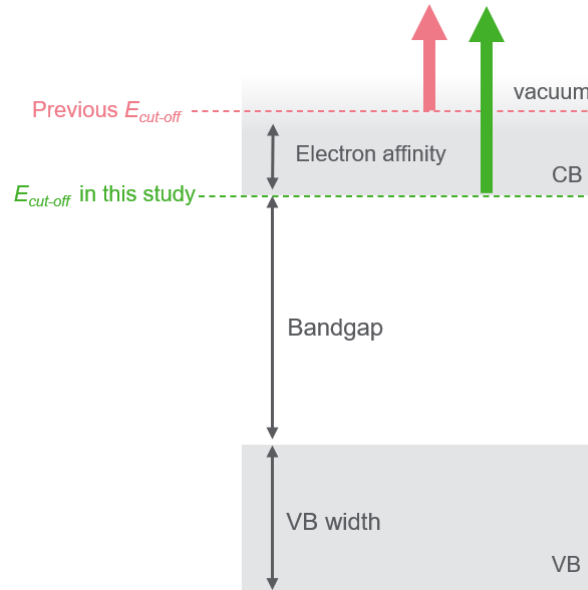


Figure 2.13: Cut-off energy in band structure (CB: Conduction band, VB:Valence band)

atom, it makes sense to set the energy threshold to 25 eV. However, this threshold is problematic for the O atom, as its deepest outer shell, the L shell, has a binding energy of 28.48 eV, which is higher than 25 eV.

Table 2.3: Outermost inner shell and deepest outer shell binding energies for elements in MOR and PMMA

	H	C	O	Sn
Atomic number	1	6	8	50
Outermost inner shell	K shell 1s _{1/2} (13 eV)	K shell 1s _{1/2} (288 eV)	K shell 1s _{1/2} (543 eV)	N shell 4d _{5/2} (28 eV)
		Deepest outer shell	L shell 2s _{1/2} (19.39 eV)	L shell 2s _{1/2} (28.48 eV)

To ensure the energy threshold is applicable to all elements in MOR and PMMA, a general energy threshold of 25 eV is set, with a specific exception of 28.48 eV being hardcoded into the source code for the O atom. The adjustment of the energy threshold between inner and outer shells will affect the calculation of kinetic energy delivered to SEs. However, this correction is expected to have a minimal impact on the results, as the change only affect Sn atom's excitation types (i.e., in the previous setting, all excitation of electrons of Sn atom will be regarded as outer shell excitation, while part of it should be inner shell excitation), and Sn atoms constitute a relatively small portion of the MOR compound composition.

2.3. Apply an Electric Field

Our project aims to improve pattern quality without increasing the EUV dose. To achieve this goal, we propose applying an electric field to steer electrons towards the bottom of

the resist. This method is expected to create an anisotropic blur with a longer z direction than the x direction, mitigating the uneven chemical gradient along the resist depth. The impact of applying the electric field will be detailed in the section 3. Here in this section, we will describe the electric field setup and outline several assumptions regarding the electric field in the simulation.

Firstly, we assume that the electric field is homogeneous, meaning that the electron experience the same acceleration due to the electric field throughout the resist material. Although, in reality, the depth of the electron's location would affect the electric field strength it experiences, this variation is considered negligible due to the very thin photoresist thickness of only 20 nm. Therefore, the electric field strength difference along the z -direction should be minimal.

Secondly, for this project, we assume that the electric field applied in the simulation is the "effective" electric field, because we don't know the static dielectric constant for MOR. We ignore the material's polarization response to the external bias, which would generate an opposing electric field, as illustrated in Figure 2.14. Since both MOR and PMMA are inhomogeneous materials, their dielectric constants might vary in different regions of the material. Thus, it is challenging to predict the materials' polarization behavior with the material data we have now, and also beyond the scope of this project. Therefore, it is important to remember that the external field we have to apply in reality in order to obtain the desired effect we got in this project is probably higher than the electric field value we show in this project.

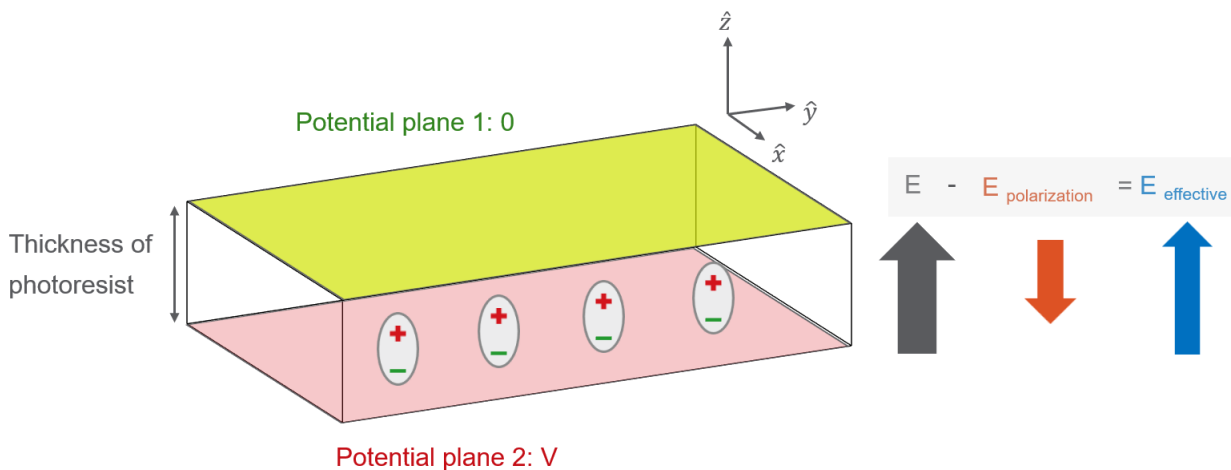


Figure 2.14: The setup of electric field

Thirdly, for each individual scattering event, we assume that the free path lengths of the electron before and after the effect of electric field are the same. This means that the initial energy loss, determined by the dielectric function (discussed in section 1.5.1), is sufficient to allow the electron to travel a certain distance without scattering before the next scattering event occurs. In the original version of Nebula, the travel path is always assumed to be a straight line for a discrete scattering event. In this study, as shown in Figure 2.15, the free travel path will be bent by the electric field with a constant acceleration dependent of the field strength. While the path length remains the same, the travel time will vary, resulting in different final velocities and kinetic energies for the electrons before and after the electric field is applied (i.e., the electron might gain or loss extra energy from the electric field). The details about when and where does the electric

field step into the simulation loop will be elaborated in section 2.4.

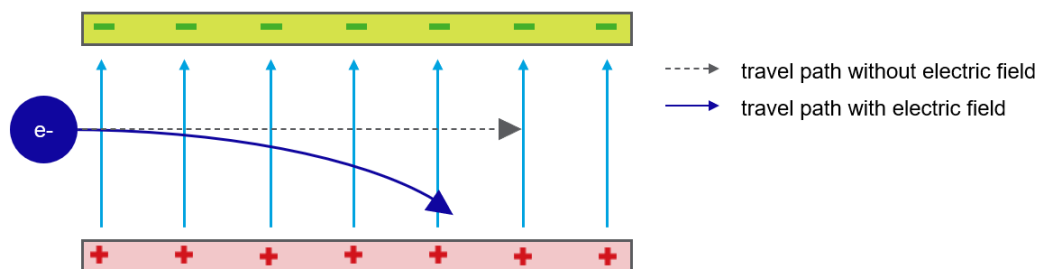


Figure 2.15: Illustration of electron movement in electric field

In this project, we choose an effective electric field range of 0 to 1 GV/m to test its effects, since most materials will break down at field strengths exceeding 1 GV/m. It is important to note that most materials will experience dielectric breakdown at lower field strengths, often within the range of 10 MV/m to few hundreds MV/m [22]. This holds true even for materials that are ultra-pure. In practical applications, the materials are typically not ultra-pure, which further reduces their dielectric strength. Moreover, dielectric strength is generally measured in terms of the externally applied voltage, rather than the internal field strength. In other words, to achieve an internal field of 1 GV/m, the externally applied field must be significantly higher than 1 GV/m. This context underscores that it is unnecessary to consider field strengths exceeding 1 GV/m, as such values are too high to be feasible in the reality. The rationale for examining a field strength of 1 GV/m is that it corresponds to adding 1 eV of energy per nanometer of travel to an electron, a scale at which significant impacts are expected.

We will present a more detailed quantitative analysis in section 3 and determine the optimal electric field strength that can enhance the pattern quality without compromising the resolution.

2.4. Events Sampling in Nebula and Electric Field Influence

In Figure 1.26, there is a blue box representing the process of probing random path length. In this section, we will show how the random path is probed and how the electric field is implemented. Figure 2.16 presents the process of mean free path sampling and the role of electric field. Everything starts with an electron possessing non-zero kinetic energy. The Nebula simulator will decide the electron's next step: whether it undergoes an elastic event or inelastic event.

Based on the electron's kinetic energy, two mean free paths will be determined for elastic and inelastic scattering respectively. Note that the mean free path is an average value, not the exact travel distance for the electron. Using these mean free paths, we can create a probability distribution following the Beer-Lambert law, as shown in Equation 2.4. We then randomly sample a path length from this probability distribution using the same method described in section 2.2.1. This results in both an elastic path and an inelastic path, and the event with the shortest path length is selected as it will happen firstly.

After determining whether the scattering is elastic or inelastic, the specific event type will be determined according to the logic in the Nebula process diagram as detailed in section 2.2.4. Following the scattering event, the electron's position, direction and kinetic energy are updated. This is where the electric field comes into play. The electric field

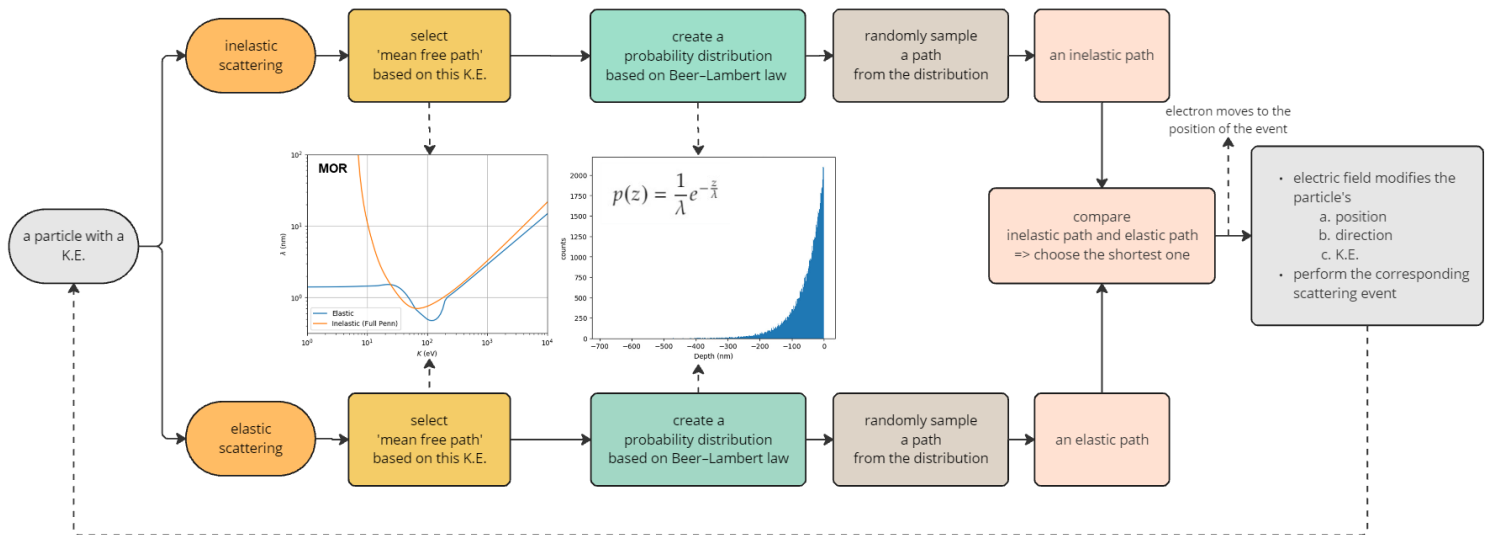


Figure 2.16: Scattering events sampling in Nebula and where does electric field come in

alters these parameters, with the electron either gaining or losing the energy depending on whether its original direction aligns with the direction of the electric field. The kinetic energy altered by the electric field will then influence the next mean free path sampling for the next scattering events until the energy is dropped below cut-off energy at which Nebula stops tracking the electrons.

3

Results and Discussion

All the details about the materials and methodologies are elaborated in Chapter 2. In Chapter 3, we will present and discuss the simulation results, validating them with the literature values. Section 3.1 will illustrate the interaction volume of MOR and PMMA under EUV exposure at different electric fields, providing an overview of electron cascade shape. We will then analyze the interaction volume in the z and r direction in section 3.1.1, 3.1.2 and 3.1.3, respectively. In section 3.2, we will examine how the electric field affect the SE yield per absorbed photon, comparing our findings to experimental values in the literature. Section 3.3 will show the definition of “blur” in this project and presents the qualitative measurement of x -direction blur and z -direction blur in the simulation. Section 3.4 will compare the blur sizes of MOR and PMMA, with comparisons to literature values. In section 3.5, we will discuss the electric fields on SE with different energies. Section 3.6 and section 3.7 will explore the impact of cut-off energy and VB width on the results and the underlying physics. Section 3.8 will conclude how these material parameters and Nebula setting changes affect the number of useful scatterings and the electric field influence. In section 3.9, we will apply Mott scattering and phonon scattering to sub-100 eV region and discuss how they response to the electric field differently and why phonon scattering might be a better model to choose. A feasibility study will be presented in section 3.10 to evaluate if this method can be beneficial to the lithography process practically and commercially. Lastly, in section 3.11, we will quantify the electron blur size with another metric and discuss our observations.

3.1. Interaction Volume Plot

The interaction volume plot represents the volume within the resist material affected by incident EUV photons and the resulting scattering events. As discussed in section 2.2.2, the energy filter is set to include only “useful” scattering events, i.e., those that generate secondary electron with enough energy to induce chemical reactions in the photoresist.

Figure 3.1 illustrates the interaction volume. In all simulations in this section, 600,000 incoming photons are used and the photoelectrons are generated following the generation method discussed in section 2.2.1. Note that even though commercially, the resist thickness for CAR is around 50 nm due to its larger absorption length under EUV exposure, the resist thickness is set to 20 nm for both MOR and PMMA in this study for easy comparison. These photoelectrons (marked as yellow spheres) generate multiple secondary electrons (marked as gray spheres) through inelastic scatterings. The scattering

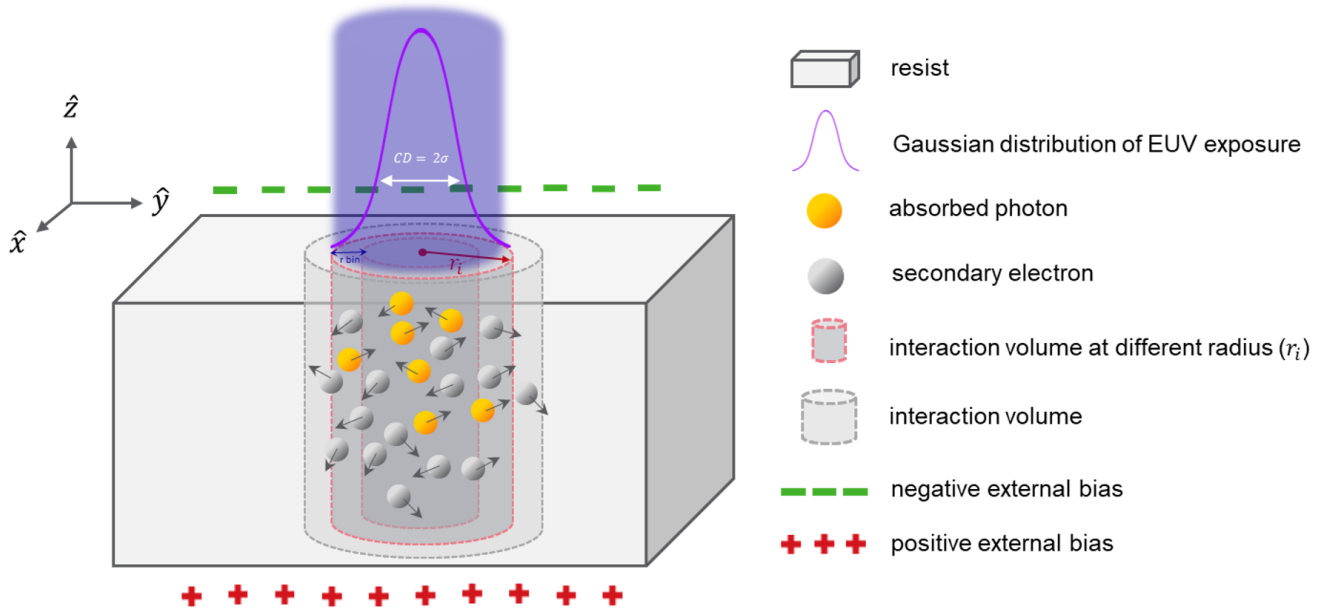


Figure 3.1: Illustration of interaction volume at different radius

is influenced by the electric field when an external bias is applied to the resist materials. Given that the exposure area is a circle, as shown in Figure 2.7, the number of useful scattering events per volume is calculated at different radii with an r-bin size of 0.07 nm, as illustrated in Figure 3.1.

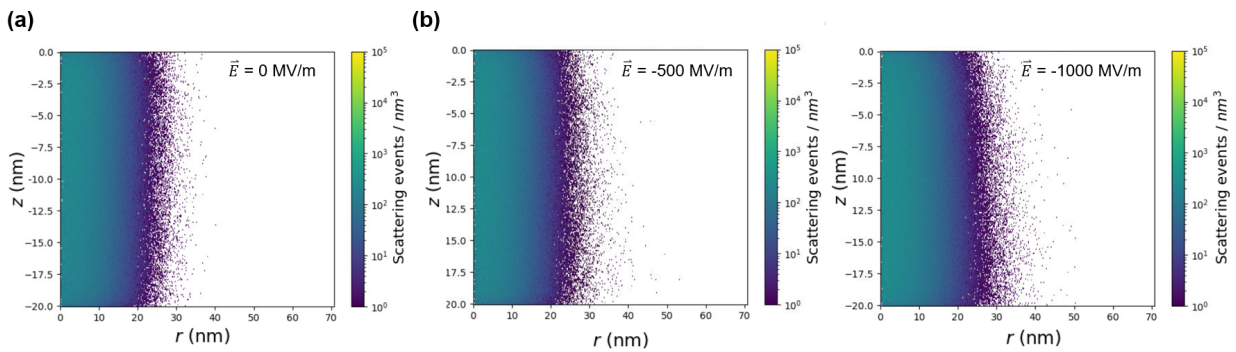


Figure 3.2: Interaction volume of MOR under varying electric fields of 0, -500, and -1000 MV/m

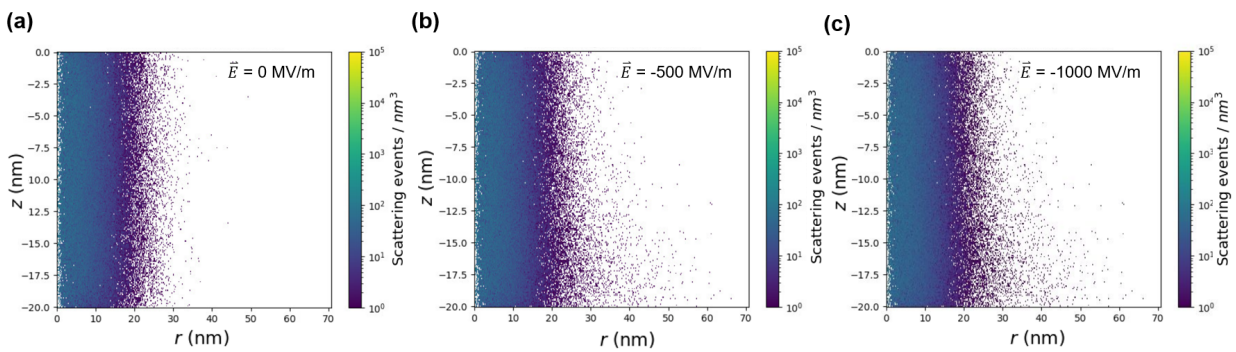


Figure 3.3: Interaction volume of PMMA under varying electric fields of 0, -500, and -1000 MV/m

Figure 3.2 and Figure 3.3 show the effect of the electric field on the electron cascade in MOR and PMMA, respectively. From the interaction volume plots, we can already see that the total number of useful scatterings in MOR is higher than in PMMA. There are two reasons for this: first, with a fixed number of incoming photons, MOR can absorb more photons than PMMA due to their different absorption lengths under EUV exposure; second, the smaller bandgap of MOR makes it easier for valence electrons to be excited.

While the interaction volume plot provides a useful overview, the logarithmic scale of the plot can sometimes exaggerate the scattering distribution. Therefore, line plots are used in the following sections for more quantitative analysis.

3.1.1. z -direction Analysis

From the interaction volume plots, we observe that electric fields can drag electrons downwards, potentially compensating for the uneven chemical gradient along the z direction, as EUV photons are absorbed more near the surface. However, an excessive concentration of electrons near the bottom is also undesirable. Therefore, we split the interaction volume in the z direction to determine the optimal electric field strength that achieves the most homogeneous distribution of useful scattering events.

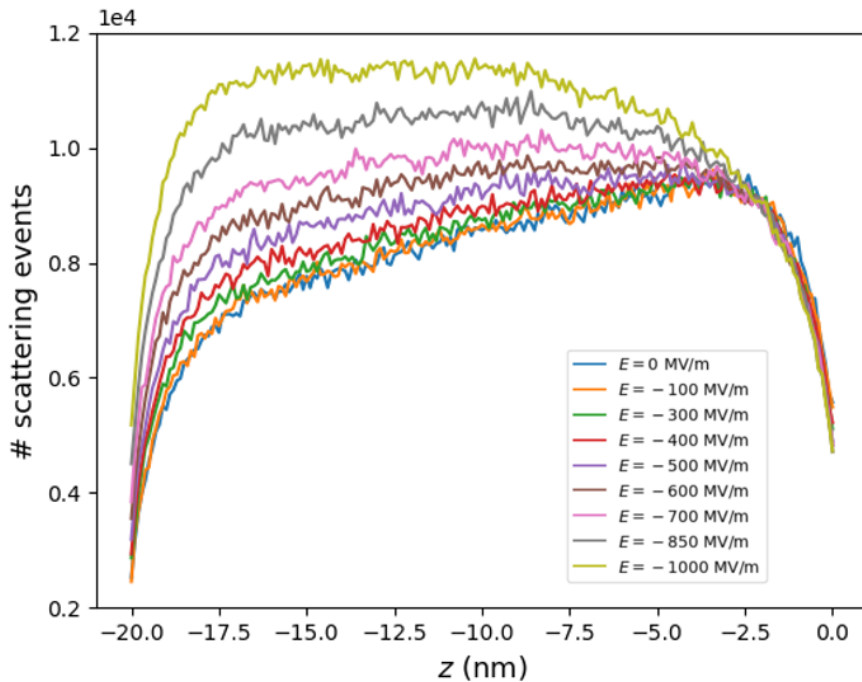


Figure 3.4: Analysis of the z -direction interaction volume of MOR under varying electric fields

Figure 3.4 shows the distribution of useful scattering along the z direction for MOR with a z -bin size of 0.1 nm. Without the electric field, most electrons are generated between $z = -2.5$ nm and $z = -5$ nm. Fewer electrons are found near the surface, as some may escape into the vacuum, and fewer are near the resist bottom due to the Beer-Lambert law, as discussed in section 2.2.1, which limits photon absorption at greater depths. However, the distribution shown on the plot is not exactly exponential decay. This is because photon absorption follows the Beer-Lambert law, whereas electron scattering does not and is a random process. There is a drop at $z = -20$ nm because electrons after this level are beyond the thickness of the resist layer, and thus are not recorded.

When the electric field is increased to -100 MV/m , the distribution remains unchanged. As the electric field strength increases further, the number of useful scatterings significantly increase near the resist bottom and decreases slightly near the surface. However, at field strengths greater than -700 MV/m , the number of useful scatterings near the bottom surpasses that near the surface, which is undesirable. Therefore, the optimal electric field strength for MOR should be at least lower than -700 MV/m to maintain a homogeneous chemical gradient along the z direction. The optimal field strength will be chosen later on combining the results of r -direction analysis.

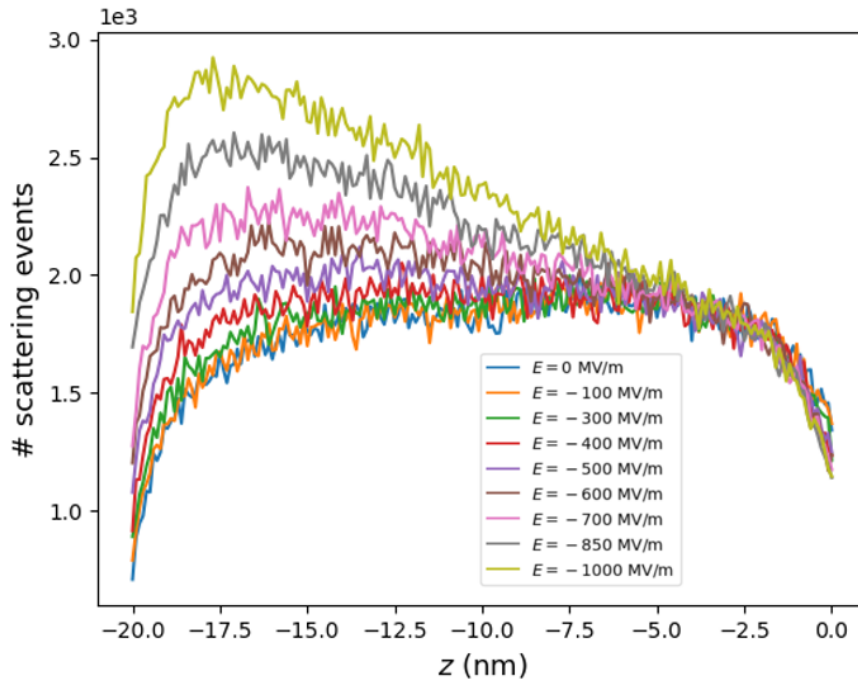


Figure 3.5: Analysis of the z -direction interaction volume of PMMA under varying electric fields

Figure 3.5 shows the distribution of useful scatterings along the z direction for PMMA. Compared to MOR, the difference of distribution in PMMA at various electric fields is more evident, corresponding to what we observed from the interaction plots in the previous section. The electric field seems to have more effect on PMMA is because PMMA's larger electron mean free path at low energies region. The physics mechanism will be elaborated in section 3.5. To keep the scattering events distribution even in the z direction, the optimal field strength should be around -400 MV/m . Also, given that the maximum dielectric strength of PMMA reported in the literature is approximately 600 MV/m [68], $E = -400 \text{ MV/m}$ can be a good choice for PMMA without breaking down the material.

3.1.2. r -direction Analysis (with different z bins)

After analyzing the interaction volume in the z direction, we then include r -direction analysis to find the optimal electric field strength for MOR and PMMA respectively. Figure 3.6 and Figure 3.7 show the distribution of useful scattering in four different z -bins along the r direction for both materials.

From Figure 3.6 (b), we observe that at the electric field of $E = -400 \text{ MV/m}$, the four z -bins have similar number of scatterings distribution within $r = 7.5 \text{ nm}$ (which is a half

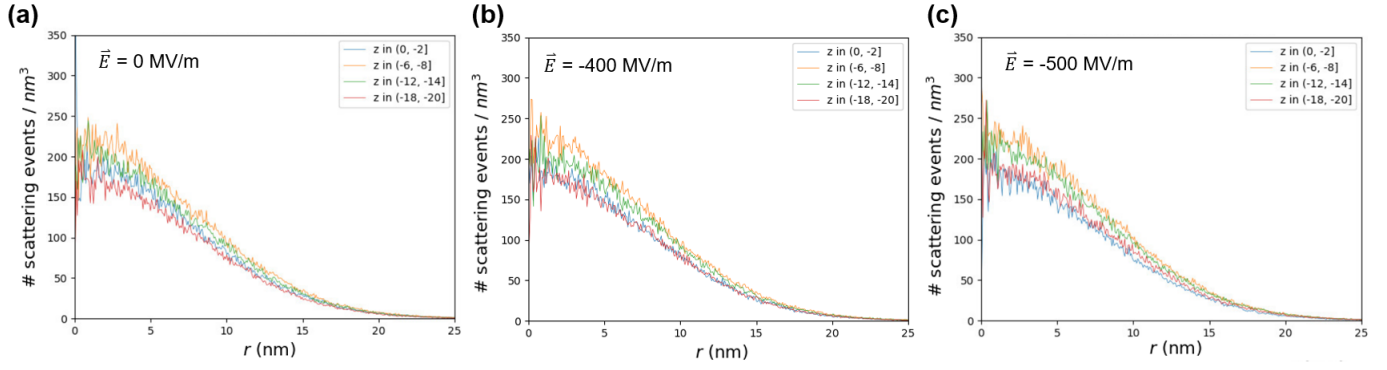


Figure 3.6: Analysis of the r -direction interaction volume of MOR in different z bins

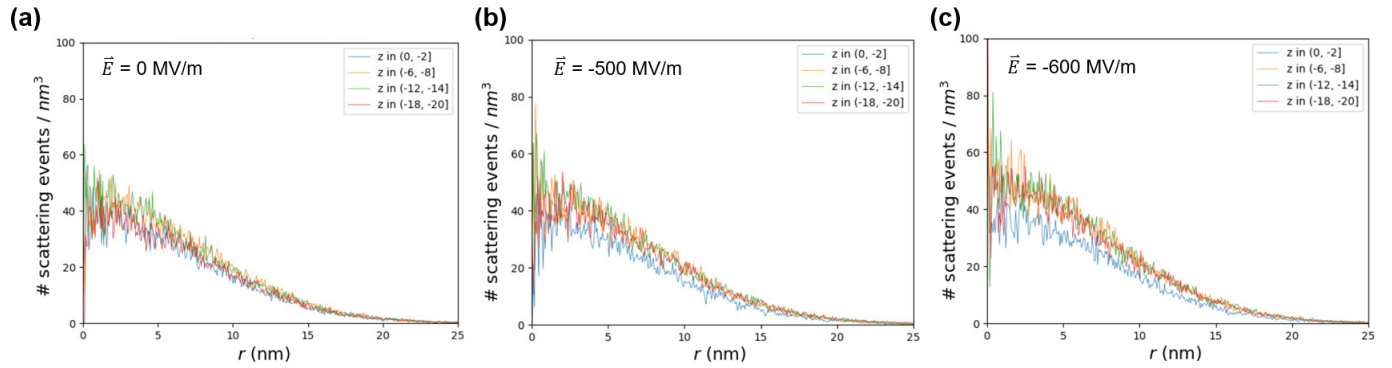


Figure 3.7: Analysis of the r -direction interaction volume of PMMA in different z bins

of CD as we discussed in section 2.2.1). However, when the electric field strength is increased to $E = -500$ MV/m, the number of scatterings in different z bins starts to split. Therefore, to maintain the homogeneous distribution along z direction within $r = 7.5$ nm, the optimal electric field for MOR should be below $E = -500$ MV/m. Combining the conclusion in section 3.1.1, the optimal electric field for MOR is chosen to be -400 MV/m. For PMMA, the number of useful scatterings in each z -bin starts to differentiate at $E = -600$ MV/m, as shown in Figure 3.7 (c). Thus, considering the conclusion in section 3.1.1, the optimal electric field for PMMA is chosen as -400 MV/m.

Combining the z and r direction analysis, we conclude that the optimal electric field strength is -400 MV/m for both MOR and PMMA, which enables a more homogeneous chemical gradient along z direction as well as an even distribution of scattering events within the critical dimension region along r direction.

3.1.3. r -direction Analysis (Effective Radius)

Effective Radius here is defined as the radius encompassing 68.3% of total useful number of scattering events, which are sufficient to cause solubility changes in the resist material, as shown in Figure 2.6. Effective Radius is examined in this section to quantify how severe the resolution along r direction is affected by the electric fields.

As presented in Figure 3.8, the effective radius of MOR does not change significantly at different electric fields. The vertical lines in the figure indicate the location of the effective radius, which are listed in Table 3.1. From Table 3.1, we can see that at the optimal electric field of $E = -400$ MV/m for MOR, the effective radius only increases by

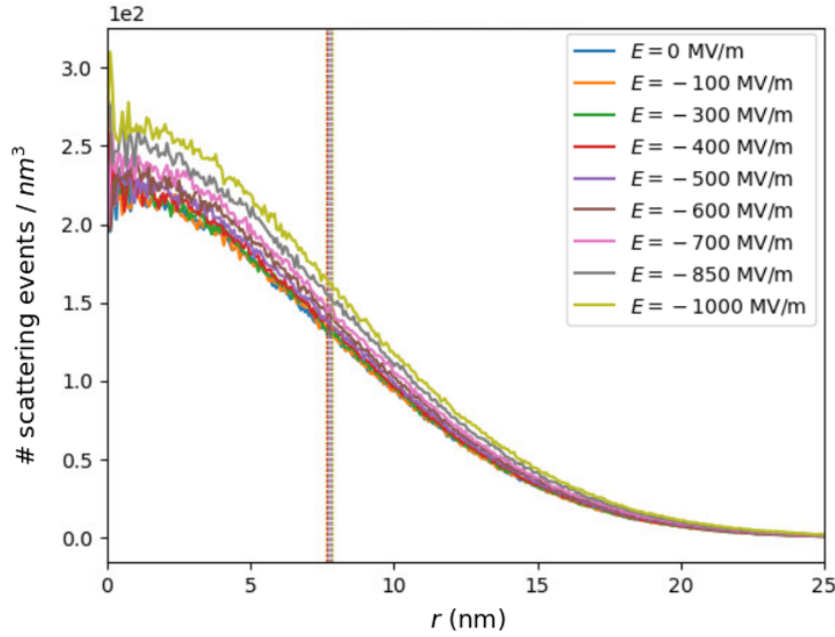


Figure 3.8: Analysis of the r -direction interaction volume of MOR under varying electric fields

0.55%.

Table 3.1: Effective radius of MOR under varying electric fields and the corresponding percentage changes

Electric field (MV/m)	Effective radius (nm)	Percentage increase (%)
0	7.640	0
-100	7.630	-0.13
-300	7.656	0.21
-400	7.682	0.55
-500	7.729	1.17
-600	7.770	1.70
-700	7.790	1.97
-850	7.833	2.52
-1000	7.871	3.03

Note: Percentage increase (%) is the effective radius at varying electric fields relative to the effective radius at $E = 0$ MV/m

Similarly, Figure 3.9 and Table 3.2 show the effective radius of PMMA. At the optimal electric field of $E = -400$ MV/m for PMMA, there is only a 0.45% increase in the effective radius. These suggest that increasing the electric field for both MOR and PMMA can improve the uneven chemical gradient along the z direction without compromising the r direction resolution.

3.2. Number of Useful SE Yield per Absorbed Photon

As discussed in section 1.3.4, MOR can absorb more EUV photons than PMMA due to its larger absorption coefficient. In the simulation results, under a fixed number of 600,000 incoming photons, MOR absorbs 185,106 photons, while PMMA absorbs only 60,008

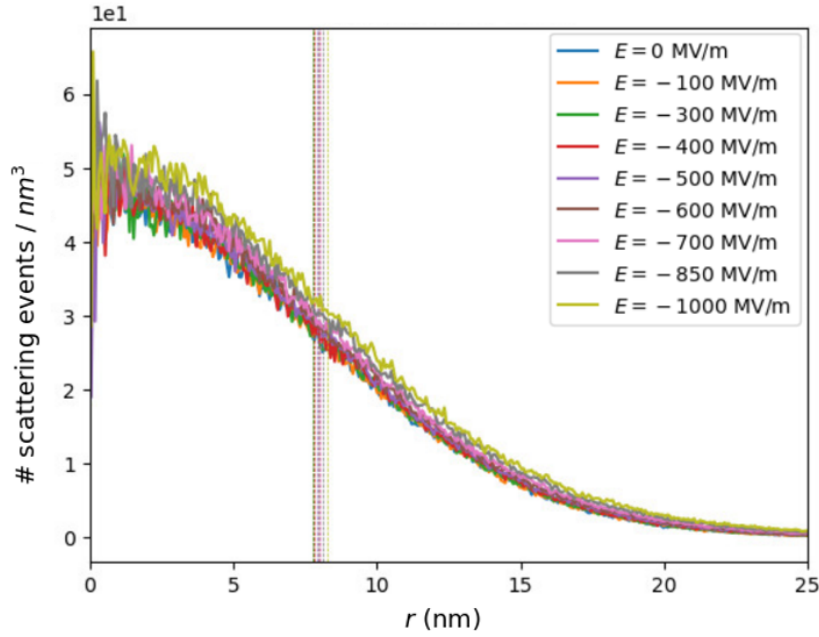


Figure 3.9: Analysis of the r -direction interaction volume of PMMA under varying electric fields

Table 3.2: Effective radius of PMMA under varying electric fields and the corresponding percentage changes

Electric field (MV/m)	Effective radius (nm)	Percentage increase (%)
0	7.759	0
-100	7.50	-0.12
-300	7.758	-0.01
-400	7.794	0.45
-500	7.908	1.93
-600	7.947	2.44
-700	8.005	3.18
-850	8.136	4.86
-1000	8.288	6.82

Note: Percentage increase (%) is the effective radius at varying electric fields relative to the effective radius at $E = 0$ MV/m

photons.

Figure 3.10 shows the number of useful scattering events per absorbed photon for MOR and how this value increases with increasing electric field strength. Without the influence of the electric field, 8.8 useful secondary electrons are generated per absorbed photon, which aligns with experimental results from Inpria, where each absorbed photon converted 8 ligands to active sites [54]. At the optimal electric field of $E = -400$ MV/m, the useful SE yield per absorbed photon increases by 3.41%. This is because electrons can gain energy from the electric field, leading to more inelastic scattering events and generating more SEs.

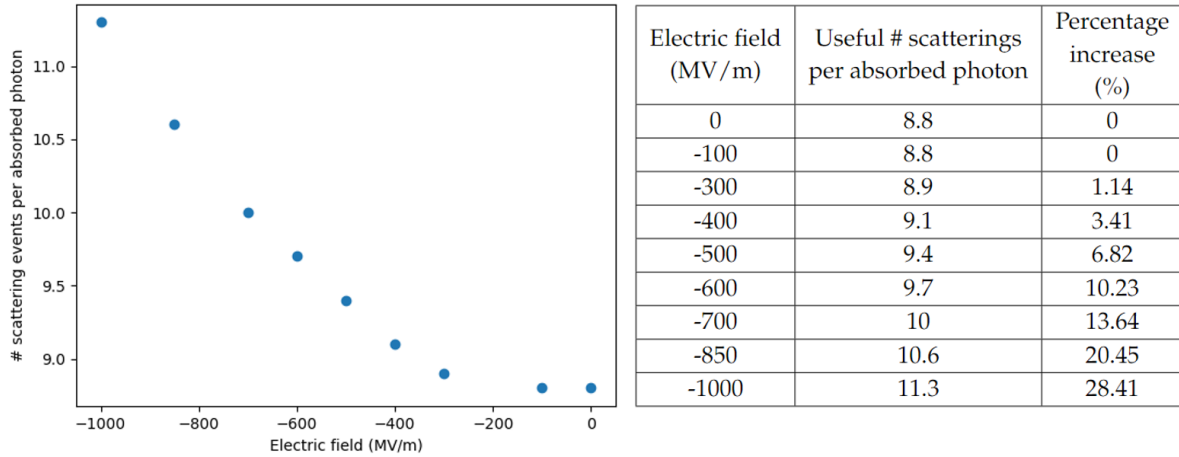


Figure 3.10: Number of useful scattering events per absorbed photon in MOR under varying electric fields

Figure 3.11 presents the simulation results for PMMA. Without the electric field, 5.9 useful SEs are generated per absorbed photon, consistent with research done by KLA, which found an SE yield per absorbed photon of 5.8 [83]. At the optimal electric field of $E = -400$ MV/m, the useful SE yield per absorbed photon increases by 3.39%.

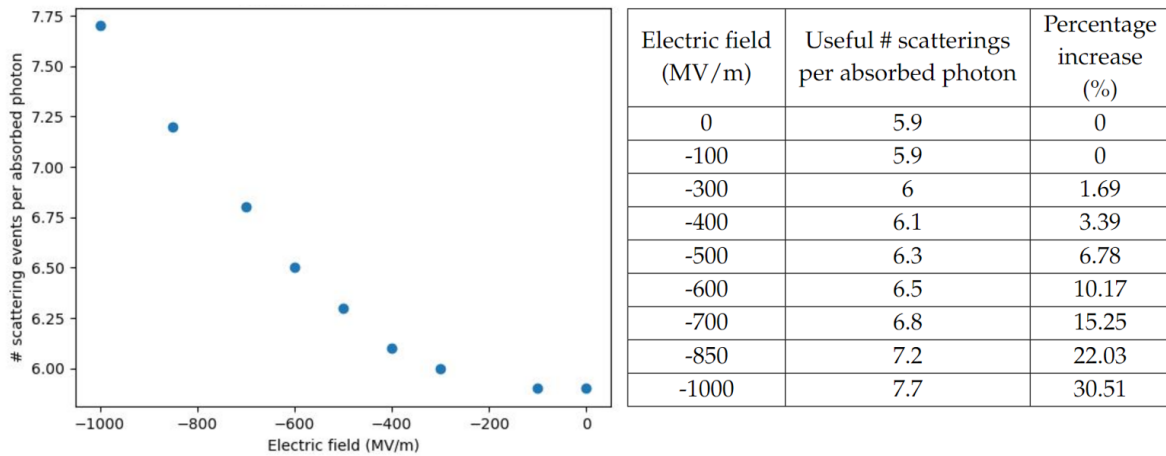


Figure 3.11: Number of useful scattering events per absorbed photon in PMMA under varying electric fields

It is important to note that increasing the SE yield per absorbed photon might not allow for a reduction of EUV dose (i.e., the number of incoming photons) due to the photon shot noise issue discussed in section 1.2.1. A minimum number of photons is necessary to ensure pattern quality and stability. However, increasing SE yield per absorbed photon enhances the likelihood that each photon will efficiently drive the chemical reaction, which is still advantageous for the process.

3.3. Qualitative Measurement of x -blur and z -blur

To quantitatively measure electron blur size in x and z direction, we generated 5000 photoelectrons at the point of $x = 0$, $y = 0$, and $z = -10$ nm, to observe how varying electric fields affect the blur.

Figure 3.12 and Figure 3.13 illustrate how different electric field strengths affect the blur

shapes, showing that the electron blur is dragged toward the bottom of resist. As shown in Figure 3.12 (a) and Figure 3.13 (a), without the influence of an electric field, the blur is isotropic since the scattering direction of electrons is randomly sampled.

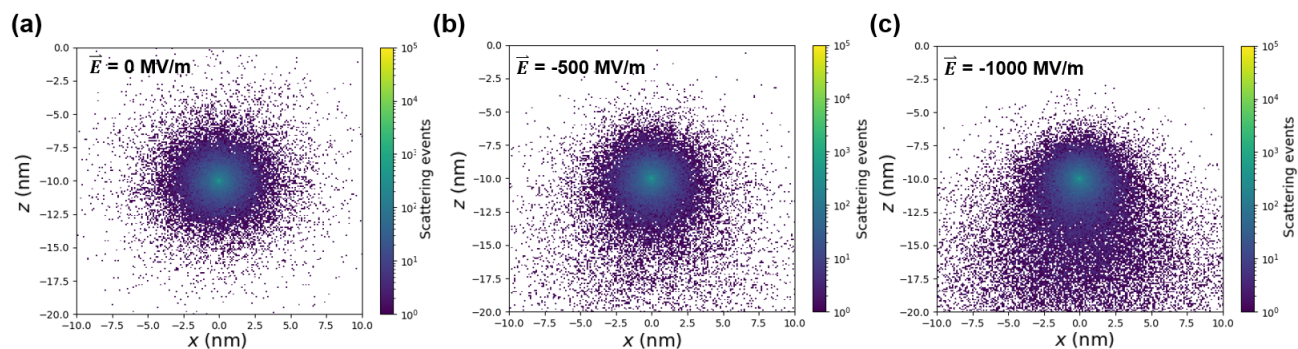


Figure 3.12: MOR blur

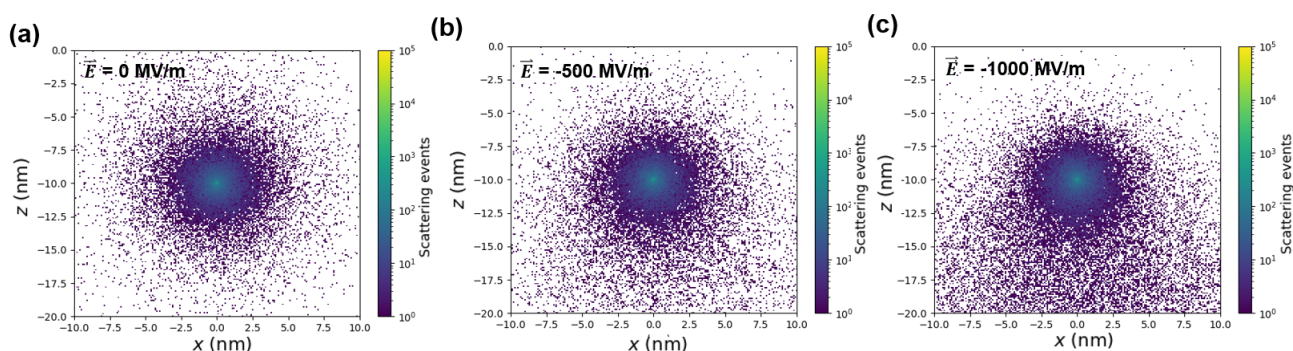


Figure 3.13: PMMA blur

The interaction volume plots shown here aim to provide an overview of the electron blur shape. A more detailed quantitative analysis will be presented in the following sections.

3.3.1. Definition of Blur Size

Before diving into the quantitative analysis of electron blur, let's define the term "blur size" as used in this project. Some literature defines electron blur as one standard deviation of a Gaussian distribution [109]. In our project, however, we define the electron blur size as the range that includes 68% of the total electrons, as these electrons might induce solubility changes in the photoresist. Note that our simulation results show that the spatial electron distribution does not resemble a Gaussian distribution. Therefore, the sigma here does not represent the standard deviation. Table 3.3 lists all the parameters used to describe electron blur and their corresponding descriptions in this project.

Figure 3.14 illustrates the definitions of x -blur and z -blur. y -blur is ignored here, because it behaves the same as x -blur. Note that while we use isotropic blur as a simple illustration example, the presence of an electric field may result in anisotropic blur with unequal x -blur and z -blur sizes, or even asymmetric blur in the z direction (i.e., $\sigma_{z+} \neq \sigma_{z-}$).

The term "anisotropy," denoted as " S " in this study, is defined as the z -blur size divided by the x -blur size. Our goal is to increase the z -blur size to enhance the counting volume of each absorbed photon without significantly increasing the x -blur, which would harm pattern resolution. We observed that increasing the electric field does lead to an increase

Table 3.3: Definition of electron blur parameters in this study

Parameter		Description
Centroid		The place photoelectrons generated: (0, 0, -10)
x -blur	Positive x -blur (σ_{x+})	The range extending in the positive x -direction (parallel to the resist surface) that includes 68% of the total electrons at positive x region. This parameter quantifies the spread of electron blur in the positive x direction.
	Negative x -blur (σ_{x-})	The range extending in the negative x -direction (parallel to the resist surface) that includes 68% of the total electrons at negative x region. This parameter quantifies the spread of electron blur in the negative x direction.
	x -blur size	The total blur size in the x direction, calculated as $\sigma_{x+} + \sigma_{x-}$.
z -blur	Upper z -blur (σ_{z+})	The range extending in the z direction (perpendicular to the resist surface) from the centroid towards the resist surface that includes 68% of the total electrons at $z > -10$ nm region. This parameter quantifies the spread of electron blur above the centroid.
	Lower z -blur (σ_{z-})	The range extending in the z direction (perpendicular to the resist surface) from the centroid downwards to the resist bottom that includes 68% of the total electrons at $z < -10$ nm region. This parameter quantifies the spread of electron blur below the centroid.
	z -blur size	The total blur size in the z direction, calculated as $\sigma_{z+} + \sigma_{z-}$.
Anisotropy (S)		The ratio of the z -blur size and x -blur size, calculated as $S = (z\text{-blur size} / x\text{-blur size})$

in z -blur size (quantitatively analyzed in section 3.3.3), but also slightly increase the x -blur (quantitatively analyzed in section 3.3.2), though not as significantly. Therefore, a trade-off must be made to balance the counting volume increase with pattern resolution. Anisotropy is used to quantify this trade-off and will be quantitatively analyzed in section 3.3.4.

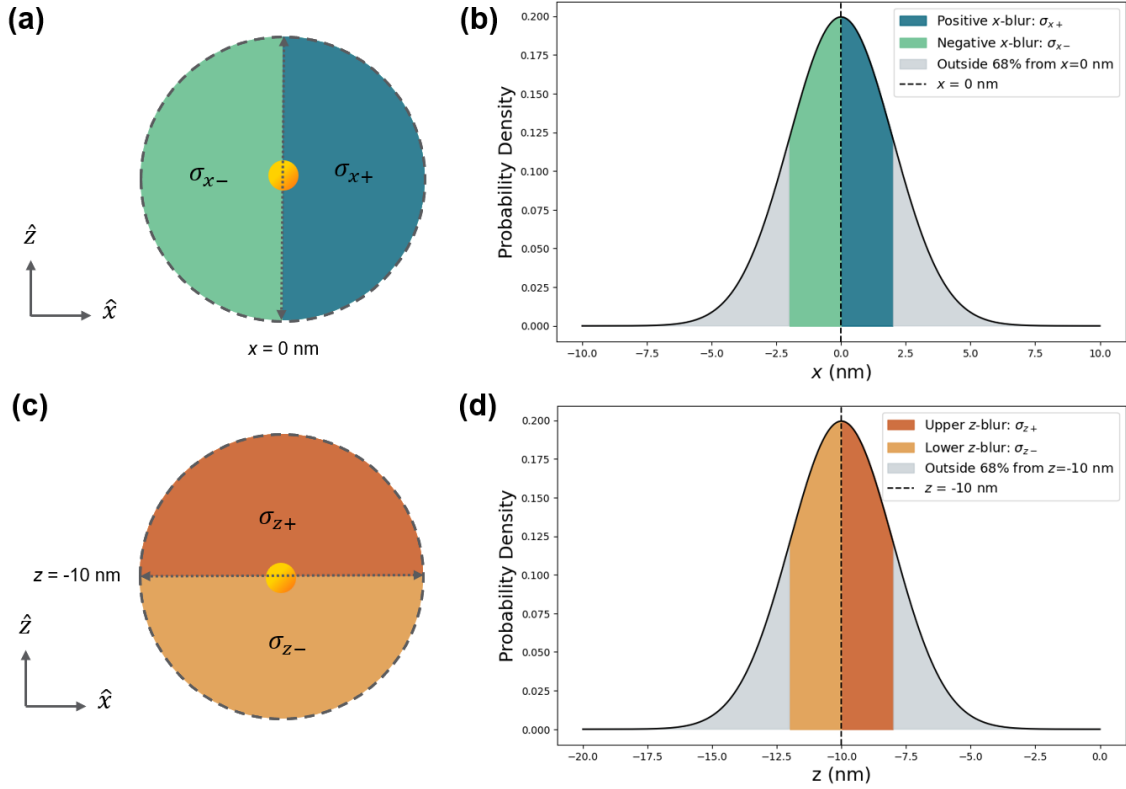


Figure 3.14: Illustration of (a) x -blur definition (b) spatial distribution along x direction with a center of $x = 0$ nm (c) z -blur definition (d) spatial distribution along z direction with a center of $z = -10$ nm

3.3.2. x -blur

Figure 3.15 (a) shows the distribution of secondary electrons in MOR along the x -direction, and Figure 3.15 (b) provides a zoomed-in view with vertical lines indicating the σ_{x+} and σ_{x-} positions from $x = 0$. Figure 3.15 (c) presents the normalized version, illustrating that the x -blur expands with increasing electric field strength. Less electric fields are shown on the plot for clarity and 600,000 photoelectrons are used here to minimize the error bars caused by this randomness.

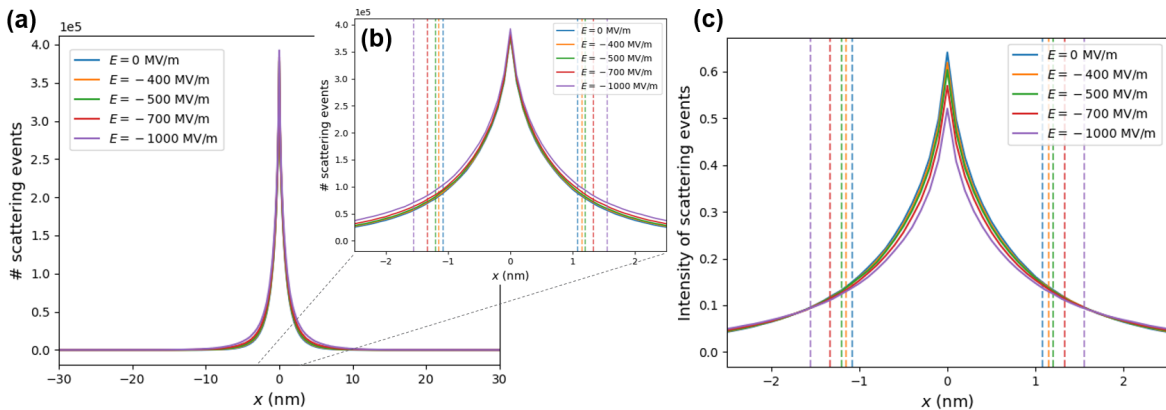


Figure 3.15: MOR (a) Secondary electron distribution along the x -direction (b) Zoomed-in plot from $x = -2.5$ nm to $x = 2.5$ nm (c) Normalized zoomed-in plot (The vertical lines indicate the x -blur region)

The percentage increases of x -blur at varying electric fields are shown in Table 3.4. Without the effect of the electric field, the positive x -blur is equal to the negative x -blur, indicating isotropy in the x direction. When an electric field is applied, both positive and negative x -blur increase by a similar magnitude. At the optimal electric field of -400 MV/m for MOR, the x -blur increases by 6.02%.

Table 3.4: Quantitative analysis of x -blur of MOR

Electric field (MV/m)	σ_{x+} (nm)	σ_{x-} (nm)	$\sigma_{x+} + \sigma_{x-}$ (nm)	Percentage increase (%)
0	1.08	1.08	2.16	0
-100	1.06	1.07	2.13	-1.39
-300	1.1	1.12	2.22	2.78
-400	1.14	1.15	2.29	6.02
-500	1.2	1.2	2.4	11.11
-600	1.26	1.27	2.53	17.13
-700	1.34	1.31	2.65	22.69
-850	1.4	1.43	2.83	31.02
-1000	1.55	1.54	3.09	43.06

Note: Percentage increase (%) is the x -blur size at varying electric fields relative to the x -blur size at $E = 0$ MV/m

A similar trend is observed for PMMA, as shown in Figure 3.16 and Table 3.5. At the optimal electric field of -400 MV/m, the x -blur increases by 6.23%.

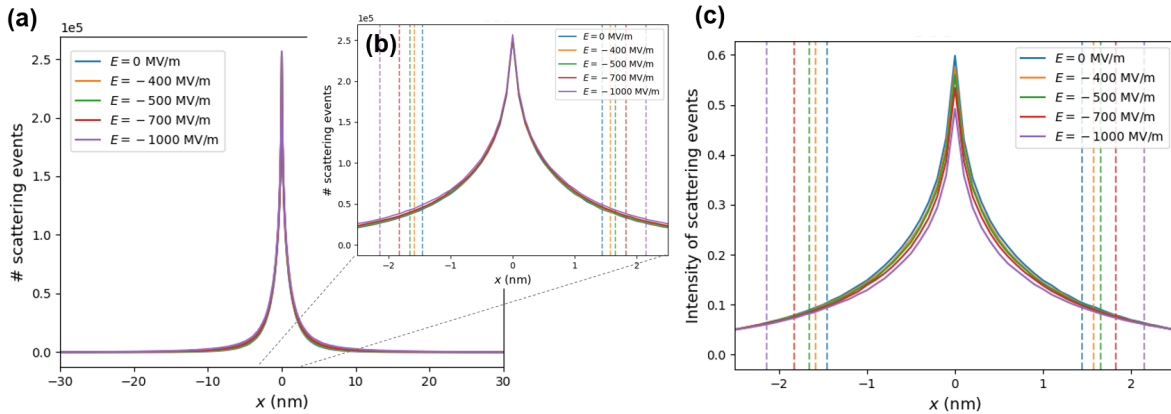


Figure 3.16: PMMA (a) Secondary electron distribution along the x -direction (b) Zoomed-in plot from $x = -2.5$ nm to $x = 2.5$ nm (c) Normalized zoomed-in plot (The vertical lines indicate the x -blur region)

Table 3.5: Quantitative analysis of x -blur of PMMA

Electric field (MV/m)	σ_{x+} (nm)	σ_{x-} (nm)	$\sigma_{x+} + \sigma_{x-}$ (nm)	Percentage increase (%)
0	1.46	1.53	2.99	0
-100	1.48	1.44	2.92	-2.34
-300	1.50	1.51	3.01	0.67
-400	1.6	1.57	3.17	6.02
-500	1.64	1.71	3.35	12.04
-600	1.72	1.75	3.47	16.05
-700	1.81	1.8	3.61	20.74
-850	1.99	1.99	3.98	33.11
-1000	2.19	2.18	4.37	46.15

Note: Percentage increase (%) is the x -blur size at varying electric fields relative to the x -blur size at $E = 0$ MV/m

3.3.3. z -blur

Figure 3.17 (a) shows the number of secondary electron along the z -direction in MOR, with vertical lines indicating the positions of upper z -blur and lower z -blur from $z = -10$ nm. Figure 3.17 (b) provides the normalized version. The plots clearly demonstrate that with increasing electric field strength, the lower z -blur increases significantly while the upper z -blur decreases slightly. This results in an enhanced number of secondary electron near the bottom of the resist. Table 3.6 lists the exact values of upper and lower z -blur and the percentage increases in z -blur size relative to the values without an electric field. Without the electric field, the ratio of σ_{z+} and σ_{z-} is around 1 : 1, indicating isotropic blur in the z direction. At the optimal electric field of -400 MV/m for MOR, the z -blur size increases by 11.93%, enhancing the counting volume along the z direction per absorbed photon. At $E = -400$ MV/m, the lower z -blur is 1.48 nm, which is longer than the upper z -blur of 0.96 nm, indicating that the z -blur is no longer symmetric as it was at $E = 0$ MV/m.

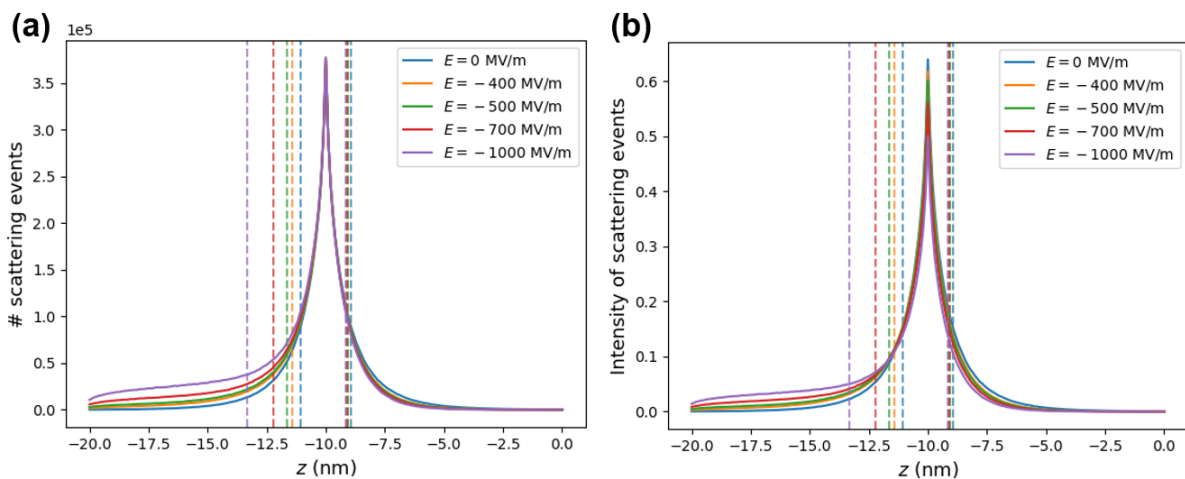


Figure 3.17: MOR (a) Secondary electron distribution along the z -direction (b) Normalized plot

Table 3.6: Quantitative analysis of z -blur of MOR

Electric field (MV/m)	σ_{z+} (nm)	σ_{z-} (nm)	$\sigma_{z+} + \sigma_{z-}$ (nm)	Percentage increase (%)
0	1.08	1.1	2.18	0
-100	1.05	1.15	2.20	0.92
-300	0.98	1.3	2.28	4.59
-400	0.96	1.48	2.44	11.93
-500	0.92	1.64	2.56	17.43
-600	0.93	1.89	2.82	29.36
-700	0.91	2.2	3.11	42.66
-850	0.88	2.75	3.63	66.51
-1000	0.81	3.27	4.08	87.16

Note: Percentage increase (%) is the z -blur size at varying electric fields relative to the z -blur size at $E = 0$ MV/m

Similarly, as shown in Figure 3.18 and Table 3.7, the z -blur increases for PMMA as well. At the optimal electric field of -400 MV/m for PMMA, the z -blur size increases by 10.17%.

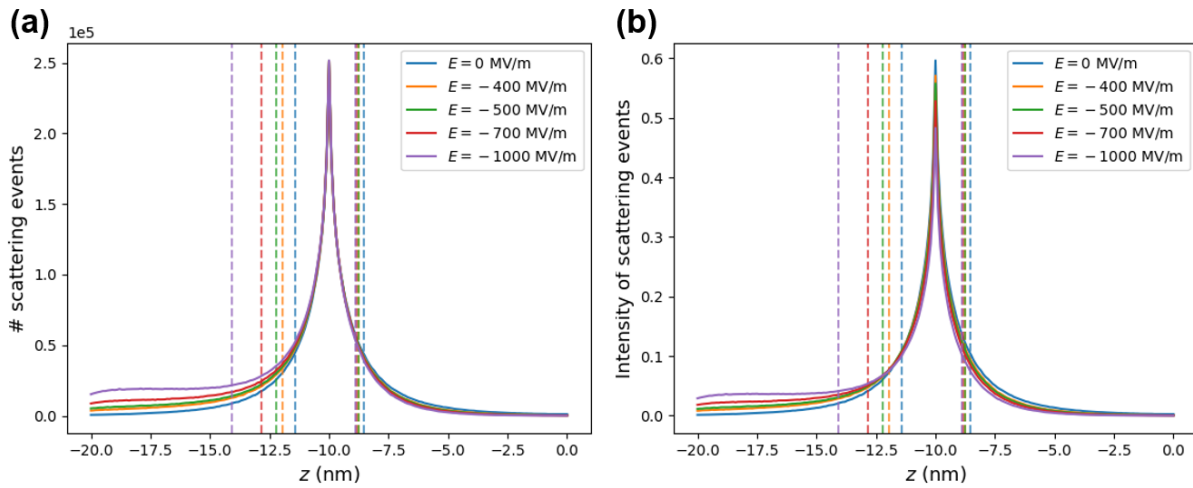
**Figure 3.18:** PMMA (a) Secondary electron distribution along the z -direction (b) Normalized plot

Table 3.7: Quantitative analysis of z -blur of PMMA

Electric field (MV/m)	σ_{z+} (nm)	σ_{z-} (nm)	$\sigma_{z+} + \sigma_{z-}$ (nm)	Percentage increase (%)
0	1.5	1.45	2.95	0
-100	1.39	1.51	2.90	-1.69
-300	1.29	1.8	3.09	4.75
-400	1.28	1.97	3.25	10.17
-500	1.20	2.23	3.43	16.27
-600	1.19	2.54	3.73	26.44
-700	1.18	2.81	3.99	35.25
-850	1.16	3.55	4.71	59.66
-1000	1.12	4.14	5.26	78.31

Note: Percentage increase (%) is the z -blur size at varying electric fields relative to the z -blur size at $E = 0$ MV/m

3.3.4. Anisotropy (S)

As discussed earlier in section 3.3.1, anisotropy is used to evaluate the ratio of z -blur to x -blur. Higher anisotropy can expand the influence of each absorbed photon without deteriorating the pattern resolution. Table 3.8 shows the anisotropy of MOR and the percentage increase with respect to $E = 0$ MV/m, while Table 3.9 shows the anisotropy of PMMA. For both materials, anisotropy is around 1 at $E = 0$ MV/m, indicating the electron blur is isotropic without the effect of the electric field. For MOR, at its optimal electric field strength of -400 MV/m, anisotropy increases by 5.7 % to 1.07. For PMMA, at its optimal electric field strength of -400 MV/m, anisotropy increases by 3.72% to 1.03.

Table 3.8: MOR: Compare x -blur and z -blur using anisotropy (S)

Electric field (MV/m)	$\sigma_{z+} + \sigma_{z-}$ (nm)	$\sigma_{x+} + \sigma_{x-}$ (nm)	S
0	2.18	2.16	1.01
-100	2.20	2.13	1.03
-300	2.28	2.22	1.03
-400	2.44	2.29	1.07
-500	2.56	2.40	1.07
-600	2.82	2.53	1.11
-700	3.11	2.65	1.17
-850	3.63	2.83	1.28
-1000	4.08	3.09	1.32

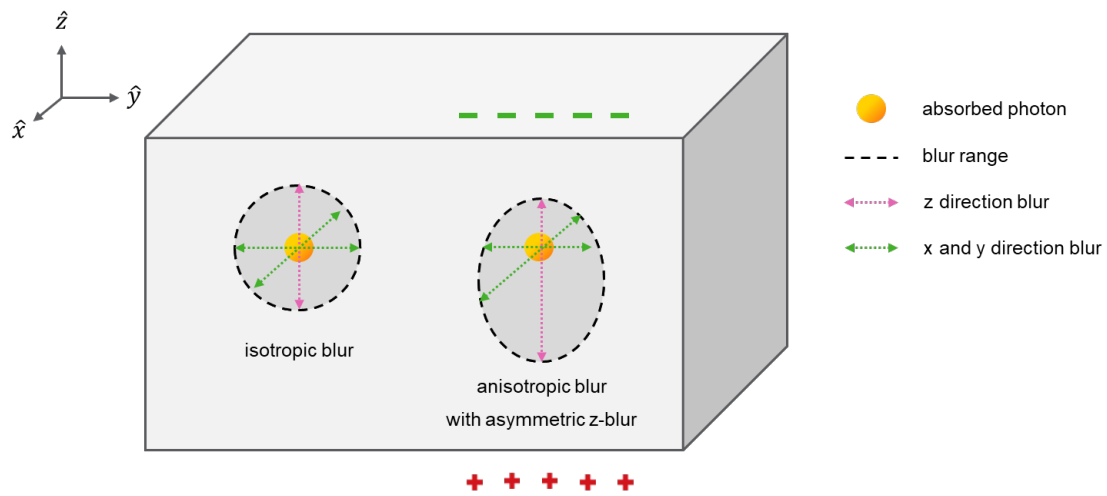
Figure 3.22 illustrates the changes in blur shape under the influence of electric field. There are two main changes:

1. The z -blur size ($\sigma_{z+} + \sigma_{z-}$) becomes larger than the x -blur size ($\sigma_{x+} + \sigma_{x-}$).
2. The lower z -blur (σ_{z-}) becomes larger than the upper z -blur (σ_{z+}).

Taking MOR as an example, without the electric field, the x -blur size is 2.16 nm and z -blur size is 2.18 nm. At $E = -400$ MV/m, the x -blur size increases slightly to 2.29 nm (6.02%),

Table 3.9: PMMA: Compare x -blur and z -blur using anisotropy (S)

Electric field (MV/m)	$\sigma_{z+} + \sigma_{z-}$ (nm)	$\sigma_{x+} + \sigma_{x-}$ (nm)	S
0	2.95	2.99	0.99
-100	2.91	2.92	0.99
-300	3.09	3.01	1.03
-400	3.25	3.17	1.03
-500	3.44	3.35	1.07
-600	3.73	3.47	1.11
-700	4.00	3.61	1.18
-850	4.71	3.98	1.20
-1000	5.26	4.37	1.21

**Figure 3.19:** Schematic of anisotropic blur with asymmetric z -blur under the electric field

while the z -blur size increases more significantly to 2.44 nm (11.93%). Consequently, anisotropy increases from 1.01 at $E = 0$ MV/m to 1.07 at $E = -400$ MV/m (Table 3.8). Furthermore, in the z direction, the upper z -blur is 1.08 nm and the lower z -blur is 1.1 nm at $E = 0$ MV/m. At $E = -400$ MV/m, the upper z -blur decreases to 0.96 nm, while the lower z -blur increases to 1.48 nm (Table 3.6).

The two changes are beneficial to enhance the resist pattern quality. The first change creates anisotropic blur, which is larger in the z direction than in the x and y directions, helping to increase the counting volume of each absorbed photon and mitigate the photon shot noise issue. The second change creates asymmetry in the z -blur, which helps to counteract light absorption at the resist surface, causing more chemical conversion to occur deeper in the resist.

3.4. Influence of deformation potential on electron blur

As mentioned in section 2.1.2, the deformation potential in the phonon properties in the material file is tuned so that the simulated electron blur size better fit the literature values. The deformation potentials for PMMA and MOR cannot be found in the literature and are difficult to obtain experimentally. In this section, we will compare the electron blur

sizes of PMMA and MOR, justify that the tuned deformation potential values fall within reasonable ranges, and explain why adjusting the deformation potential significantly affects the electron blur size but not the number of useful SE yields per absorbed photon.

The blur size found in the literature is typically one standard deviation, so the average electron blur ($\sigma_{average}$) is calculated here as the average of the x -blur size and z -blur size to compare with the literature values. Table 3.10 shows how the average electron blur is calculated.

Table 3.10: The average electron blur of MOR ($\Xi = 3$ eV) and PMMA ($\Xi = 0.9$ eV) at $E = 0$ MV/m

	Electric field (MV/m)	σ_{x+} (nm)	σ_{x-} (nm)	σ_{z+} (nm)	σ_{z-} (nm)	$\sigma_{average}$ (nm)
MOR	0	1.08	1.08	1.08	1.1	1.09
PMMA	0	1.46	1.53	1.5	1.45	1.49

Note: $\sigma_{average} = \frac{1}{4} (\sigma_{x+} + \sigma_{x-} + \sigma_{z+} + \sigma_{z-})$

Table 3.11 lists the literature values of electron blur and the number of useful SE yields per absorbed photon. Table 3.12 demonstrates how changing the deformation potential can affect the electron blur size but not the number of useful SE yield per absorbed photon. While adjusting the deformation potential changes the blur size, it doesn't significantly affect the useful SE yield because the SE yield is dominated by the inelastic mean free path, which doesn't change with phonon properties.

Table 3.11: The literature values of electron blur and useful number of SE per absorbed photon for MOR and PMMA

	MOR	PMMA
Electron blur (nm)	1.1 [83]	1.5 [83]
Useful # SE per absorbed photon	8 [54]	5.8 [83]

Table 3.12: The influence of deformation potential in electron blur and useful number of SE per absorbed photon for MOR and PMMA at $E = 0$ MV/m

	MOR		PMMA	
Deformation potential (eV)	2	3	2	0.9
Electron blur (nm)	1.39	1.09	0.98	1.49
Useful # scatterings per absorbed photon	8.7	8.8	6	5.8

From Figure 3.20 (a) and (b), we observe that increasing the deformation potential decreases the elastic mean free path for $E < 100$ eV. In the phonon scattering mechanism,

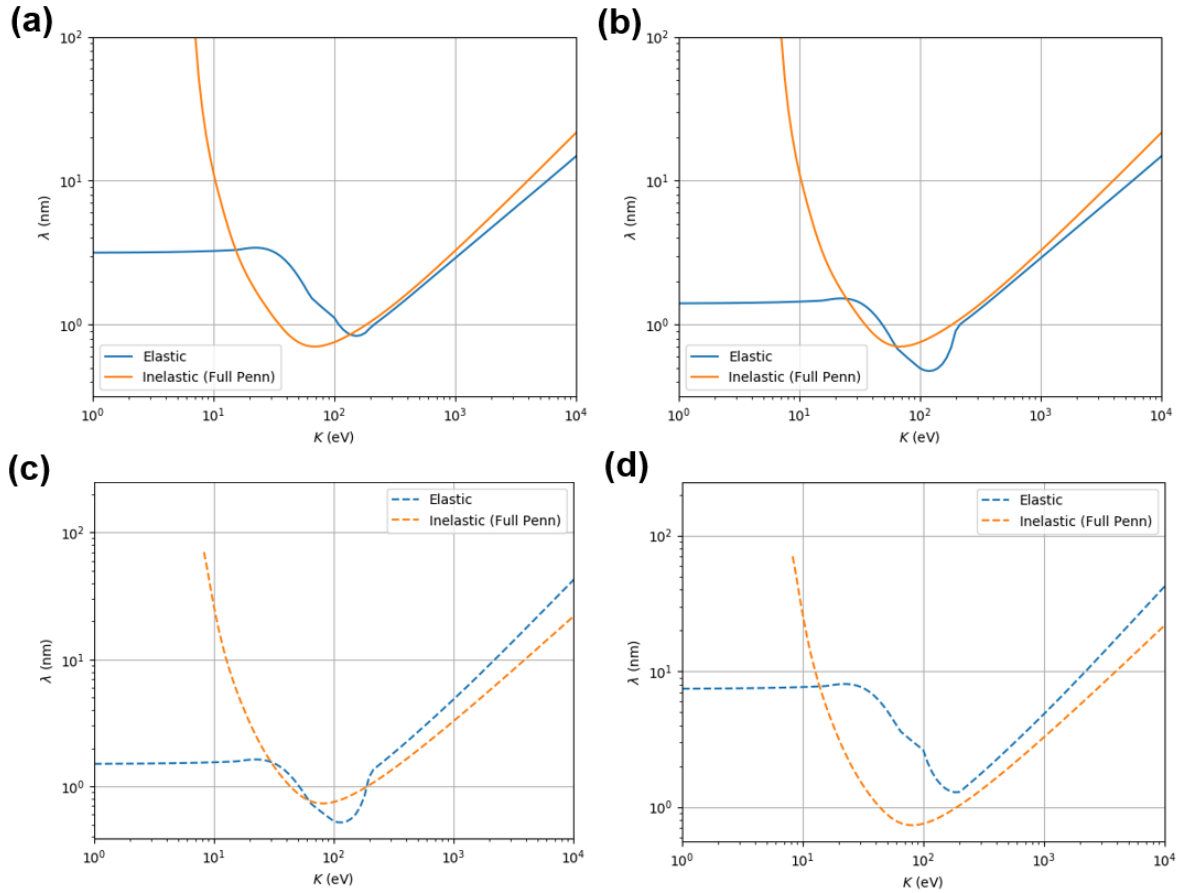


Figure 3.20: The influence of deformation potential (Ξ) in elastic mean free path (a) MOR with $\Xi = 2$ eV (b) MOR with $\Xi = 3$ eV (c) PMMA with $\Xi = 2$ eV (d) PMMA with $\Xi = 0.9$ eV

the relationship between the elastic mean free path and the deformation potential follows Equation 3.1.

$$\lambda_{elastic} \propto \frac{1}{P_{AC}} \propto \frac{1}{\Xi^2} \quad (3.1)$$

where $\lambda_{elastic}$ is the elastic mean free path, P_{AC} is the phonon acoustic scattering rate and Ξ is the deformation potential. The phonon acoustic scattering rate is the rate at which electrons are scattered by acoustic phonons, and the deformation potential describes the change in electronic levels due to strain induced by phonons. More detailed equations and physical mechanism of phonon scattering can be found in Fitting and Schreiber's work [39, 91]. Simply put, a larger deformation potential leads to a higher phonon acoustic scattering rate because the coupling strength between the electrons and lattice vibrations is stronger. With a higher scattering rate, the elastic mean free path becomes shorter. This is why increasing the deformation potential of MOR from 2 eV to 3 eV decreases the electron blur size, and vice versa when decreasing the deformation potential for PMMA.

Another reason why the elastic mean free path at low energy affects the electron blur size hugely is that most electrons have an energy below 20 eV, where elastic scattering is dominant. Figure 3.21 shows the distribution of kinetic energy and the corresponding

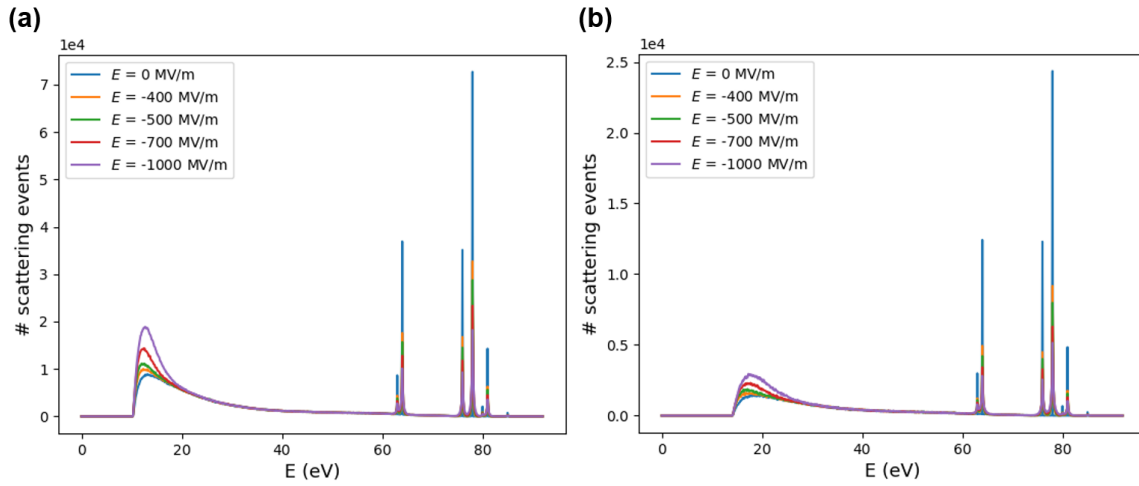


Figure 3.21: Distribution of energy before scattering event (a) MOR (b) PMMA

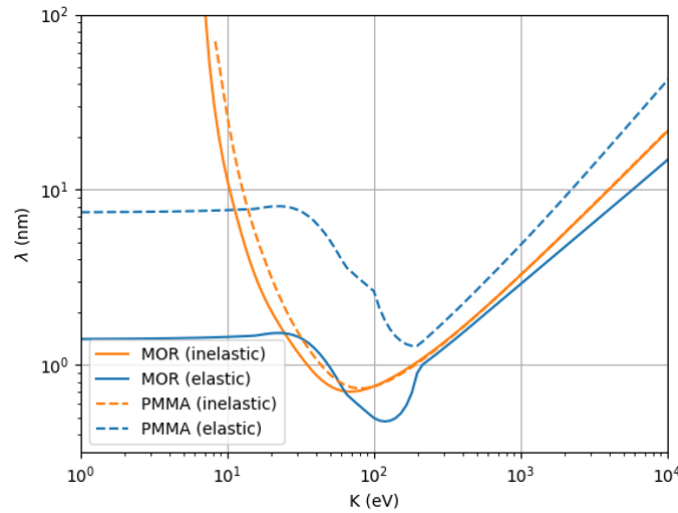


Figure 3.22: Elastic and inelastic mean free path of MOR ($\Xi = 3$ eV) and PMMA ($\Xi = 0.9$ eV)

number of scattering events. The highest peak around 60 to 80 eV is due to initially generated photoelectrons, as discussed in section 2.2.1. In Figure 3.21 (a), we see that for MOR, most scatterings occur in the energy range of 10.33 eV to around 20 eV. (Note that the electron with an energy below 10.33 eV are not recorded here as they cannot generate SEs with sufficient energy to drive the chemistry, as illustrated in Figure 3.28) Referring to Figure 3.22, we can see that elastic scattering dominates in this energy range, as the elastic mean free path is much shorter than the inelastic mean free path. In Figure 3.21 (b), most scatterings for PMMA occur in the energy range of 14.2 eV to around 20 eV. Below around 17 eV, elastic scattering dominates, while above it, inelastic scattering becomes more significant. However, both (in)elastic mean free paths of PMMA in this region are larger than those of MOR, which is why the electron blur of PMMA is larger than that of MOR.

Now, the question comes to: Do the adjusted deformation potential values make sense physically? As mentioned in section 2.1.2, there is no way to measure the deformation potential for PMMA and MOR accurately, and experimental errors might be significant. However, the deformation potential in crystalline materials is relatively well-known.

From the literature, the longitudinal deformation potential for silicon is 9.2 eV, and the transverse deformation potential is 5 eV [73]. As crystalline solids have a more rigid and ordered structure, we assume that their deformation potentials might be larger than those of PMMA and MOR. The electronic states in polymer like PMMA are less tightly bound and thus less sensitive to phonon-induced distortion. Therefore, PMMA might have a smaller deformation potential than silicon. Moreover, adding metal clusters to the polymer (i.e., MOR) might lead to a slightly higher deformation potential, as metal clusters create localized electronic states, introducing stronger electronic-lattice interactions. Thus setting a deformation potential of 0.9 eV for PMMA and 3 eV for MOR might be within a reasonable range. Additionally, the density of MOR is 2.5 g/cm^3 , and for PMMA, it is 1.192 g/cm^3 , so it makes sense that MOR has a smaller mean free path than PMMA from this perspective.

3.5. Influence of Electric Field on SE with Low Energy

From the simulation results in the previous sections, we have found that electric fields influence the electron movement and yield. Interestingly, the influence of the electric field appears to be more pronounced for electrons with lower energy. In this section, we will discuss the fundamental reasons behind this phenomenon. Note that in the following sections, only MOR will be used for discussion.

3.5.1. Observations in Simulation

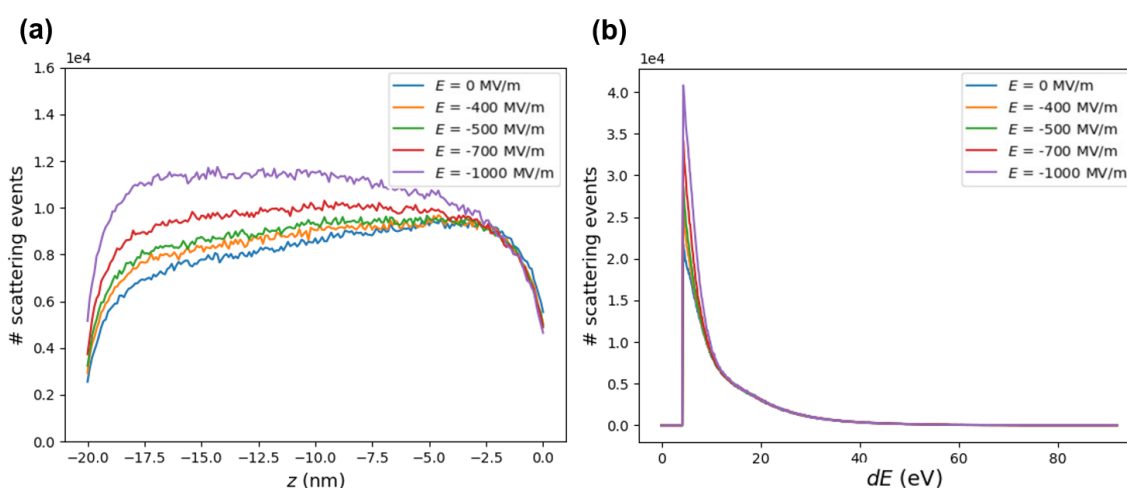


Figure 3.23: MOR (a) Analysis of the z -direction interaction volume under varying electric fields (b) Distribution of energy delivered to SE

Figure 3.23 (a) shows the z -direction analysis of the interaction volume with 600,000 initial photons at only five different electric field strengths for easier comparison. From the figure, we observe that the electric field increases the number of secondary electrons most significantly near the bottom of the resist. Most electrons near the bottom have lower energy compared to those near the surface, as EUV light is absorbed mostly at the surface. Figure 3.23 (b) shows the energy loss distribution (i.e., the energy transferred to SE), and we can see that the electric field increases the number of low energy SEs, which is sufficient to drive the chemistry. These observations imply that the electric field has the most effect on SEs with low energy.

3.5.2. Conceptual Analysis

Here in this section, we provide a theoretical and qualitative analysis to understand how electric fields affect low-energy SEs. Figure 3.24 illustrates the simplified movement of an electron with and without the influence of an electric field (Note: In Nebula, both the velocity and direction are in three dimension, not a single value as shown in the figure here). As mentioned in section 2.3, the travel free path length (ΔS) of the electron during an individual scattering event is assumed to be the same regardless of the presence of an electric field. This is because ΔS is correlated with the initial kinetic energy of the electron. However, the travel path will be bent by the electric field, and depending on the direction of acceleration and the electron's original movement, the travel time might decrease or increase.

\vec{v}_0 represents the initial velocity of the electron, and KE_1 is its corresponding kinetic energy. After scattering events and the influence of the electric field, the final velocity changes to \vec{v} , and the kinetic energy changes to KE_2 . The details of how scattering events are chosen are discussed in section 1.5.2, and the influence of the electric field on kinetic energy is covered in section 2.4.

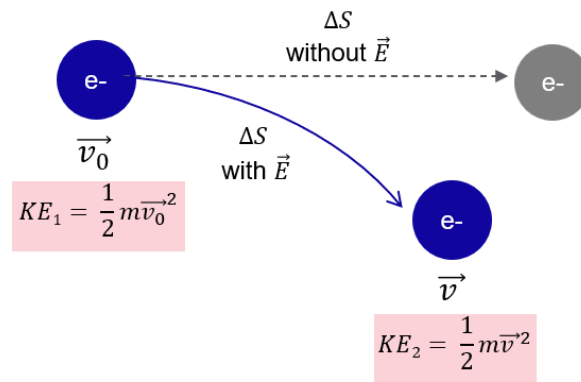


Figure 3.24: Illustration of an electron's travel path bent by an electric field

Equation 3.2 shows the relation between initial and final velocity, where \vec{a} is the acceleration due to the electric field, and Δt is the travel time affected by the electric field.

$$\vec{v} = \vec{v}_0 + \vec{a} \times \Delta t \quad (3.2)$$

As shown in Equation 3.3, the acceleration is constant and has a specific direction since the electric field is assumed to be homogeneous. Here, \vec{F} is the electric force formed from external bias, m_e is the mass of an electron, q_e is the charge of an electron, and \vec{E} is the electric field.

$$\vec{a} = \frac{\vec{F}}{m_e} = \frac{q_e \times \vec{E}}{m_e} \quad (3.3)$$

Therefore, if the acceleration is constant, then the travel time Δt acts like a scaling factor that magnifies the effect of the electric field. The travel time depends on the free travel path length ΔS , which is sampled from the mean free path as discussed in section 2.4. Referring back to Figure 2.2 (a), we can see that in the region where K is below 100 eV, the

mean free path increased as kinetic energy decrease. This explains why the electric field has a larger influence on low-energy SEs: SEs with lower energy have a larger mean free path, which corresponds to a longer travel time and thus magnifies the effect of electric field. In the next two sections, we will validate this concept with numerical values in simulation.

3.5.3. Quantitative Analysis: Method 1

To demonstrate the effect of the electric field on the electron movement, let's consider an extreme case where the acceleration due to the electric field is in the same direction as the electron's movement (i.e., downwards in the z -direction), as shown in Figure 3.25. This ensures that the electron will gain the maximum energy from the electric field. Using the data from Figure 2.2 (a), we can find the exact mean free path value and its corresponding kinetic energy of the electron in the MOR. To compare the effect of the electric field on electrons with different energies, we select an electron with a low energy of 10.33 eV (the minimum energy before useful scattering, as shown in Figure 3.21 (a)) and an electron with a relatively high energy of 80 eV.

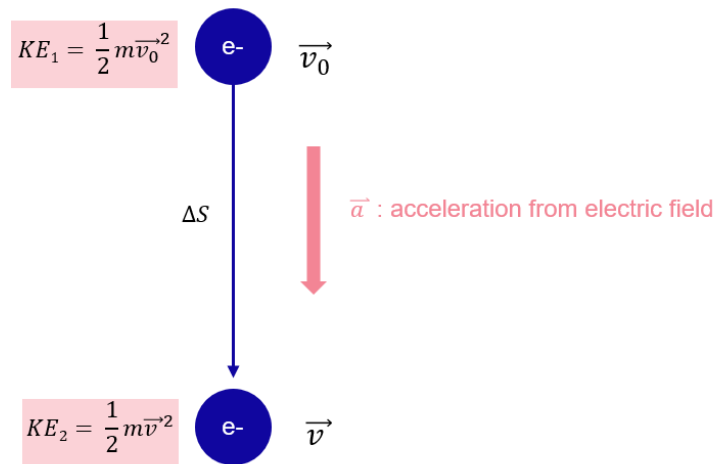


Figure 3.25: Illustration of an electron moving in the same direction as the electric field acceleration

Table 3.13 shows the percentage increase in kinetic energy before and after the effect of the electric field for an initial electron energy of 10.33 eV and a corresponding mean free path of 10 nm. Table 3.14 shows the percentage increase in kinetic energy before and after the effect of the electric field for an initial electron energy of 80 eV and a corresponding mean free path of 0.711 nm. The optimal electric field of -400 MV/m for MOR is chosen in both cases. Note that the mean free path is used here as free path length. However, in real simulations, the free path length is not necessary equal to the mean free path, but is sampled based on the Beer-Lambert law, as shown in Equation 2.4, with λ as the mean free path.

From Table 3.13, we see that the kinetic energy increases by 38.72%, starting from 10.33 eV and ending at 14.33 eV. This significant increase is due to the large mean free path, which magnifies the effect of the electric field. The travel time needed to traverse the same free path length is reduced because of the acceleration from the electric field.

On the other hand, an electron with an initial energy of 80 eV shows only a 0.35% increase in kinetic energy, from 80 eV to 80.28 eV, as shown in Table 3.14. The travel time remains

Table 3.13: Percentage increase in kinetic energy of electron in MOR at $E = -400$ MV/m with initial kinetic energy of 10.33 eV and a free path length of 10 nm

	Free path length (nm)	Velocity (m/s)	Travel time (s)	Kinetic energy (eV)	Percentage increase (%)
Before electric field	10	1.91e+06	5.25e-15	10.33	0
After electric field		2.25e+06	4.822e-15	14.33	38.72

Note: Percentage increase (%) is the kinetic energy before the electric field relative to the kinetic energy after the electric field

Table 3.14: Percentage increase in kinetic energy of electron in MOR at $E = -400$ MV/m with initial kinetic energy of 80 eV and a free path length of 0.711 nm

	Free path length (nm)	Velocity (m/s)	Travel time (s)	Kinetic energy (eV)	Percentage increase (%)
Before electric field	0.711	5.3e+06	1.34e-16	80	0
After electric field		5.31e+06	1.341e-16	80.28	0.35

Note: Percentage increase (%) is the kinetic energy before the electric field relative to the kinetic energy after the electric field

almost the same because the free path length is very short, and the electric field can hardly have any effect.

In summary, from this quantitative analysis, we see that electrons with lower initial kinetic energy are more significantly affected by the electric field due to their longer mean free paths, which allow the electric field to exert a greater influence on the travel time. This difference in influence is clearly demonstrated by the substantial increase (38.72%) in kinetic energy for the 10.33 eV electron compared to the negligible increase (0.35%) for the 80 eV electron.

3.5.4. Quantitative Analysis: Method 2

To further illustrate this concept, we generate 5000 photoelectrons at coordinates (0, 0, -10), as what we did in section 3.3. However, in the analysis of this section, instead of generating starting energies of photoelectrons using the method discussed in section 2.2.1, photoelectrons are generated with a specified starting energies to compare the influence of electric field on each case.

Figure 3.26 shows the energy spectrum of photoelectrons with different starting energies. From Figure 3.26 (a) to Figure 3.26 (d), the starting energies of the photoelectrons are 80 eV, 50 eV, 20 eV and 15 eV, respectively. We then counted the number of useful scattering events for each starting energy at varying electric field strengths.

From Figure 3.26 (a), we observe that when all photoelectrons are generated with a starting energy of 80 eV, the percentage increase in the number of useful scatterings from

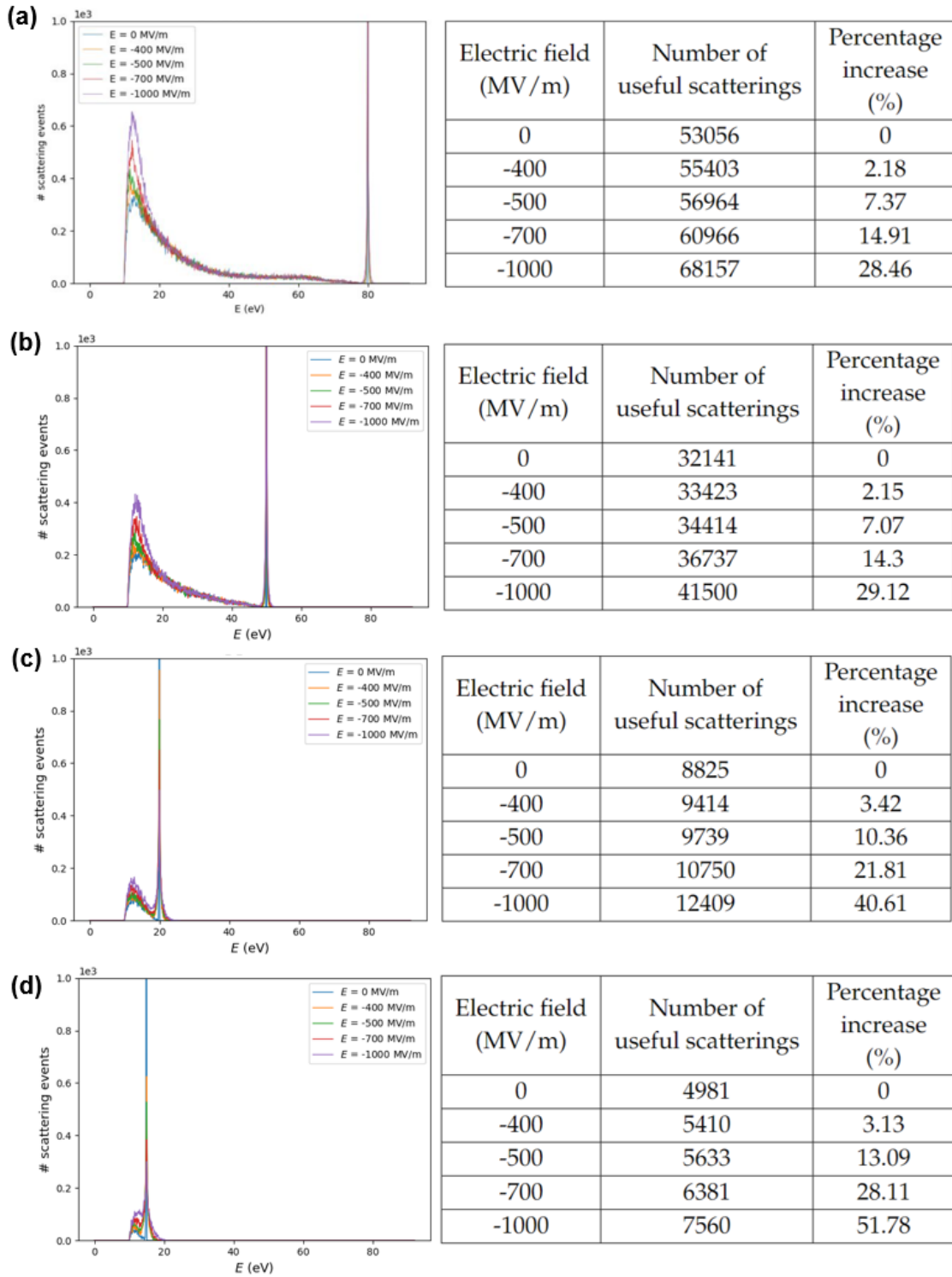


Figure 3.26: Percentage increase in useful scatterings (relative to $E = 0$ MV/m) at varying electric fields with different initial photoelectron energies: (a) 80 eV, (b) 50 eV, (c) 20 eV, and (d) 15 eV

$E = 0$ MV/m to $E = -1000$ MV/m is 34.52%. In contrast, as shown in Figure 3.26 (d), if we generate all photoelectrons at the same location but with a starting energy of 15 eV, the influence of the electric field becomes more significant. The percentage increase in the number of useful scatterings from $E = 0$ MV/m to $E = -1000$ MV/m is 64.21%.

In this quantitative analysis, the percentage increase in the number of useful scatterings from $E = 0$ MV/m to $E = -1000$ MV/m for photoelectrons with starting energies of 80 eV, 50 eV, 20 eV and 15 eV are 34.52%, 36.34%, 50.48% and 64.21%, respectively. This clearly demonstrates a trend: the electric field has a more significant influence on electrons with lower energy.

3.6. Influence of Cut-off Energy on Results

The cut-off energy to stop tracking an electron in Nebula has been changed from the vacuum level to the bottom of the conduction band in this project's use case, as discussed in detail in section 2.2.3. Our simulation results indicate that this change make the influence of electric field much more apparent compared to other parameter changes. This section explores the reasons behind this phenomenon.

3.6.1. Observations in Simulation

Figure 3.27 shows the z-direction analysis of the interaction volume of MOR with different cut-off energies.

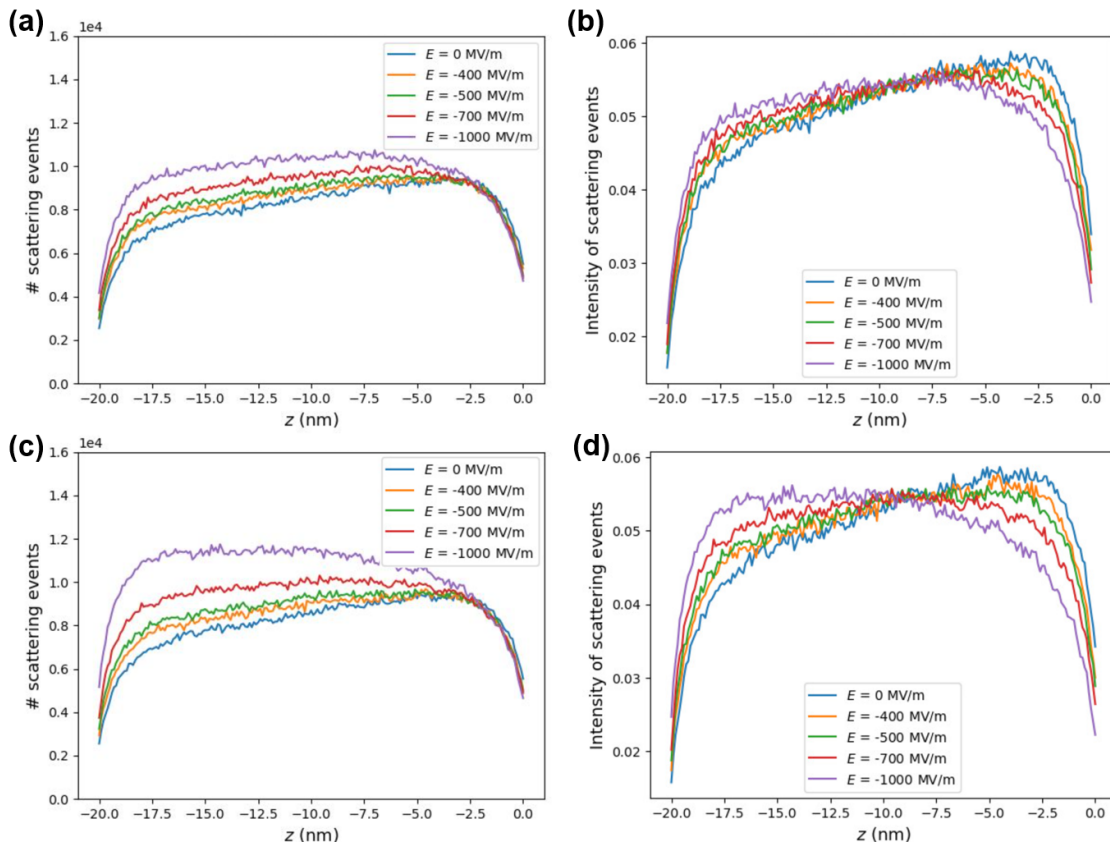


Figure 3.27: MOR with a valence band width of 2 eV and an electron affinity of 1.13 eV: (a) Cut-off energy at the vacuum level, (b) Normalized plot of (a), (c) Cut-off energy at the bottom of conduction band, (d) Normalized plot of (c)

Figure 3.27 (a) is simulated with the cut-off energy set to the vacuum level, while Figure 3.27 (c) is simulated with the cut-off energy set to the bottom of the conduction band. From Figure 3.27 (a) and its normalized plot in Figure 3.27 (b), we observe that the number of useful scatterings does not change significantly with varying electric fields. However, with the cut-off energy set to the bottom of the conduction band, the changes

become more evident, as shown in Figure 3.27 (c) and (d).

3.6.2. Conceptual Analysis

Figure 3.28 presents the band structure of MOR with two types of cut-off energies indicated. When the cut-off energy is set to the vacuum level, the minimum tracking energy of an electron in Nebula is 7.13 eV, as the bottom of the valence band is set to 0 eV in Nebula. This means that when an electron's energy drops below 7.13 eV, it will be removed by Nebula, as no electron can exist in the bandgap, which is a forbidden area for electrons. Similarly, when the cut-off energy is set to the bottom of the conduction band, the minimum tracking energy of an electron in Nebula is 6 eV.

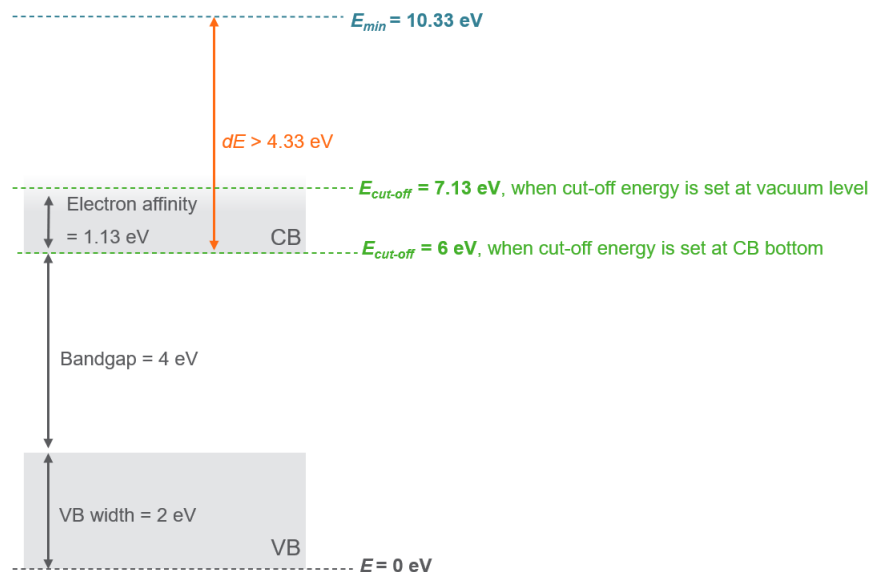


Figure 3.28: Band structure of MOR with two kinds of cut-off energies indicated

The number of useful scatterings and their energy distribution is illustrated in Figure 3.29. Electrons in zone 3 (i.e., with energy greater than E_{min}) can undergo useful scattering events and generate useful SE that can drive the chemical reactions. However, when the cut-off energy is set to the vacuum level, electron in zone 2 will still be tracked, as their energy is above the minimum tracking energy of 6 eV in Nebula. By the same logic, when the cut-off energy is set to the bottom of the conduction band, electrons in both zone 1 and zone 2 will be tracked in Nebula.

The primary reason why changing the cut-off energy affects the electric field's influence is that electrons in zone 1 or zone 2 might gain energy from the electric field and jump to the zone 3 region, thereby contributing to the number of useful scatterings. When the cut-off energy is set to the bottom of the conduction band, more electrons have potential to gain energy from the electric field. Also, as quantitatively analyzed in section 3.5.1, the electron with such a low energy in zone 1 and zone 2 can gain a lot of energy from the electric field, especially for electrons in zone 1. This is why the electric field's influence is more pronounced when $E_{cut-off}$ is 6 eV.

3.6.3. Quantitative Analysis

To quantify the differences in simulation results at different cut-off energies, we calculated the number of useful scatterings at varying electric fields for both cut-off energies cases.

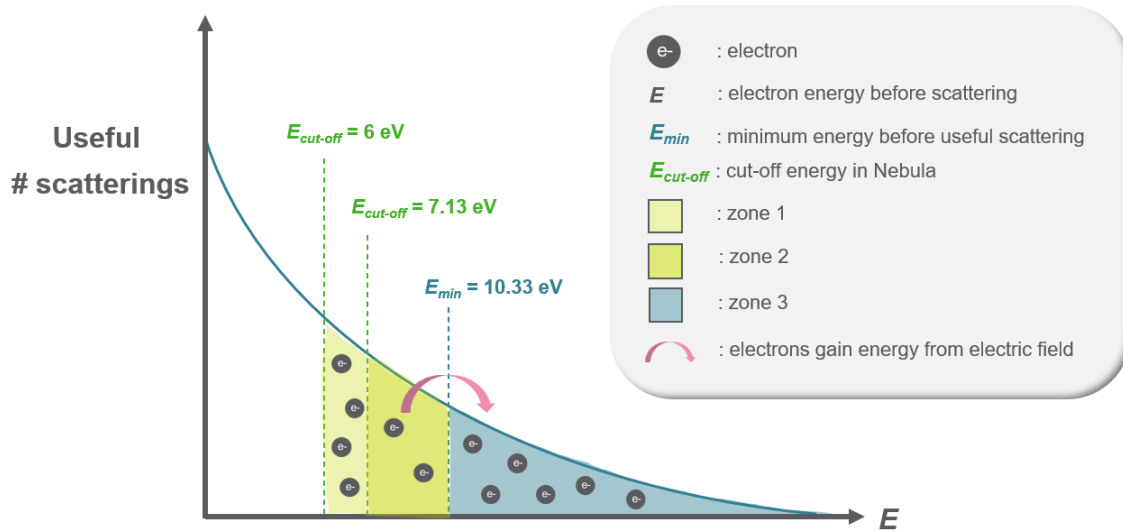


Figure 3.29: Illustration of how different cut-off energies affect the electric field influence

Table 3.15: Percentage increase in the number of useful scatterings in MOR at varying electric fields with cut-off energy set at vacuum level (i.e., $E_{cut-off} = 7.13$ eV) and VB width = 2 eV

Electric field (MV/m)	Number of useful scatterings	Percentage increase (%)
0	1.622e+06	0
-400	1.684e+06	3.89
-500	1.709e+06	5.34
-700	1.787e+06	10.14
-1000	1.92e+06	18.35

Note: Percentage increase (%) is the number of useful scatterings at different electric fields relative to $E = 0$ MV/m

Table 3.16: Percentage increase in the number of useful scatterings in MOR at varying electric fields with cut-off energy set at CB bottom (i.e., $E_{cut-off} = 6$ eV) and VB width = 2 eV

Electric field (MV/m)	Number of useful scatterings	Percentage increase (%)
0	1.622e+06	0
-400	1.676e+06	3.21
-500	1.729e+06	6.58
-700	1.854e+06	14.3
-1000	2.094e+06	29.13

Note: Percentage increase (%) is the number of useful scatterings at different electric fields relative to $E = 0$ MV/m

Table 3.15 shows that when the cut-off energy is set to the vacuum level, there is a 18.35% increase in the number of useful scatterings as the electric field strength increases from $E = 0$ MV/m to $E = -1000$ MV/m. In contrast, Table 3.16 demonstrates a 29.13% increase when the cut-off energy is set to CB bottom. This indicates that setting the cut-off energy to the CB bottom can amplify the influence of the electric field.

3.7. Influence of VB width on Results

The reason why VB width of 2 eV is chosen for MOR has been elaborated in section 2.1.3. Interestingly, our simulation results indicate that setting the VB width from 0 eV to 2 eV affects the number of useful scatterings but does not significantly affect the electric field influence magnitude. In this section, we will discuss the reasons behinds this phenomenon both qualitatively and quantitatively.

3.7.1. Observations in Simulation

Figure 3.30 (a) shows the simulation results for the case of VB width = 0 eV and Figure 3.30 (b) is its normalized version. Figure 3.30 (c) and Figure 3.30 (d) present the same for the case of VB width = 2 eV.

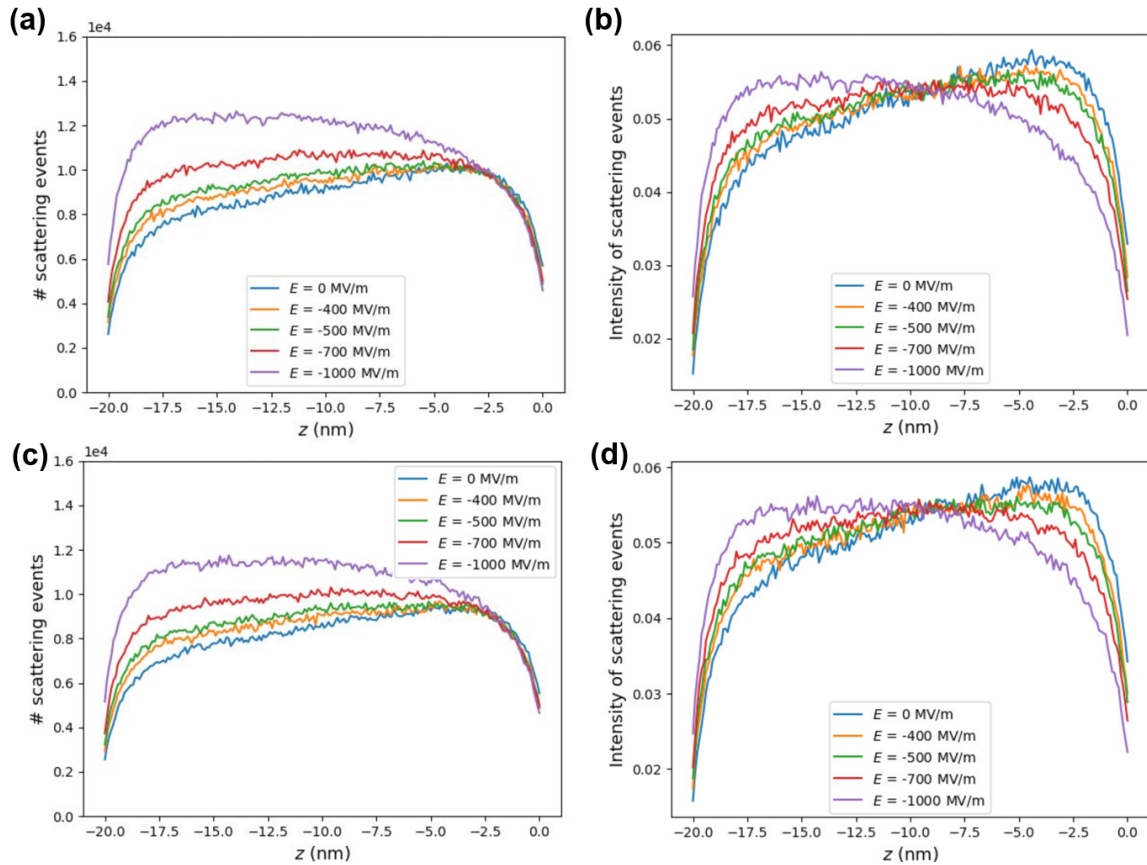


Figure 3.30: MOR with an electron affinity of 1.13 eV and a cut-off energy set to CB bottom: (a) VB width = 0 eV, (b) Normalized plot of (a), (c) VB width = 2 eV, (d) Normalized plot of (c)

Comparing Figure 3.30 (a)(b) and Figure 3.30 (c)(d), we observe that the electric field's influence remains almost the same; however, the number of useful scattering slightly increases. These observation will be quantified in section 3.7.3.

3.7.2. Conceptual Analysis

Figure 3.31 presents the band structure of MOR with different VB widths. The cut-off energy is 4 eV for MOR with VB width = 0 eV and 6 eV for VB width = 2 eV. The change of VB width also changes the minimum energy before scattering from 8.33 eV to 10.33 eV.

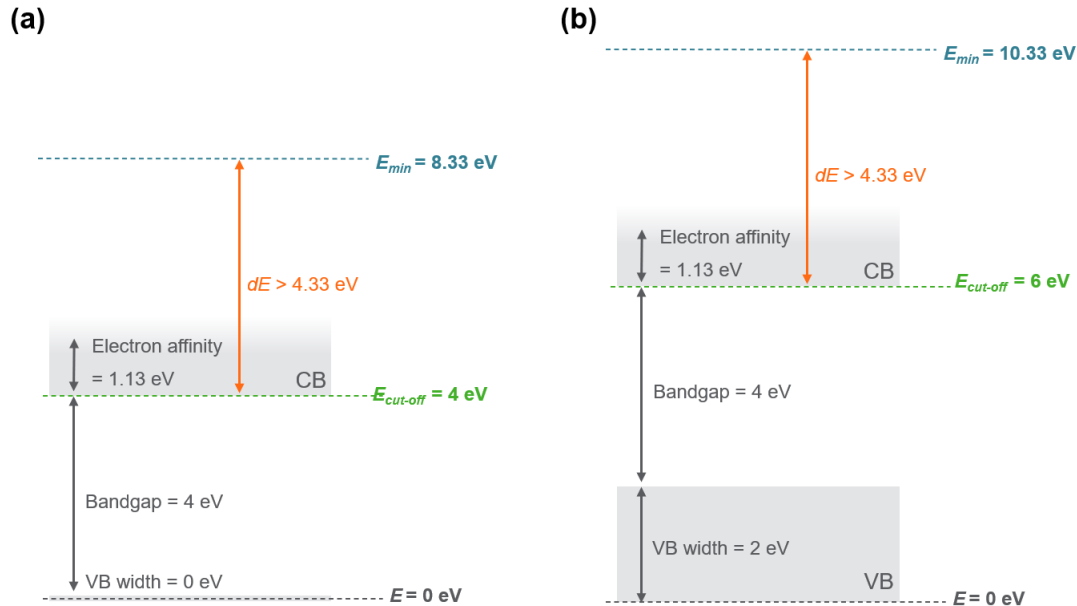


Figure 3.31: Band structure of MOR with cut-off energy at CB bottom and different VB widths (a) VB width = 0 eV (b) VB width = 2 eV

Figure 3.32 (VB width = 0 eV) and Figure 3.33 (VB width = 2 eV) illustrate how changing the VB width affects the simulation results.

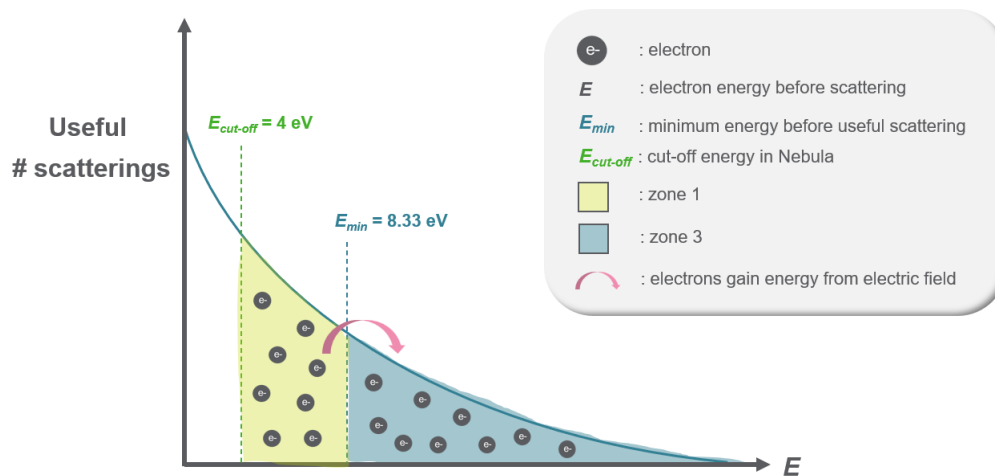


Figure 3.32: Illustration of how VB width affects the number of useful scatterings (cut-off energy at CB bottom and VB width = 0 eV)

In Figure 3.32, the minimum energy before useful scattering is 8.33 eV, lower than the 10.33 eV in Figure 3.33. Thus, increasing the VB width from 0 eV to 2 eV might decrease the number of useful scatterings, as fewer electrons are recorded. However, the number of electrons in zone 1 and their potential to gain energy from the electric field differs in

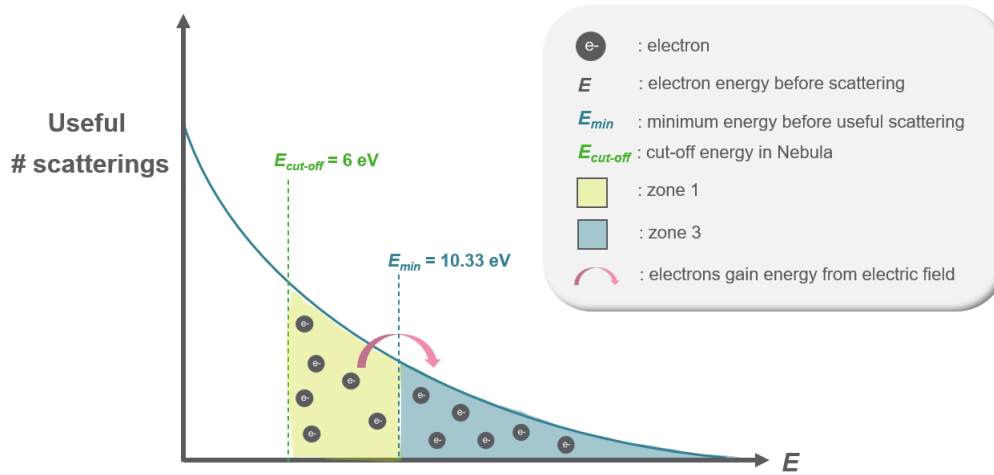


Figure 3.33: Illustration of how VB width affects the number of useful scatterings (cu-off energy at CB bottom and VB width = 2 eV)

these two cases, which affect the electric field influence magnitude. Therefore, in the following section, we will quantify the simulation results to analyze more deeply.

3.7.3. Quantitative Analysis

Comparing Table 3.17 (VB width = 0 eV) and Table 3.16 (VB width = 2 eV), we see that the percentage increase in each electric field strength relative to $E = 0$ MV/m is very similar. This indicates that the number of electrons in zone 1 in Figure 3.32 and Figure 3.33 and their ability to gain energy from the electric field are relatively similar. Thus changing the VB width from 0 eV to 2 eV does not significantly affect the electric field influence. However, we found that the number of useful scatterings at $E = 0$ MV/m decreases when setting VB width from 0 eV to 2 eV. This is due to the change of E_{min} , as shown in Figure 3.34, electrons in zone 4 are not counted in the VB width = 2 eV case.

Table 3.17: Percentage increase in the number of useful scatterings in MOR at varying electric fields with cut-off energy set at CB bottom and VB width = 0 eV

Electric field (MV/m)	Number of useful scatterings	Percentage increase (%)
0	1.733e+06	0
-400	1.797e+06	3.46
-500	1.836e+06	5.97
-700	1.967e+06	13.54
-1000	2.243e+06	29.46

Note: Percentage increase (%) is the number of useful scatterings at different electric fields relative to $E = 0$ MV/m

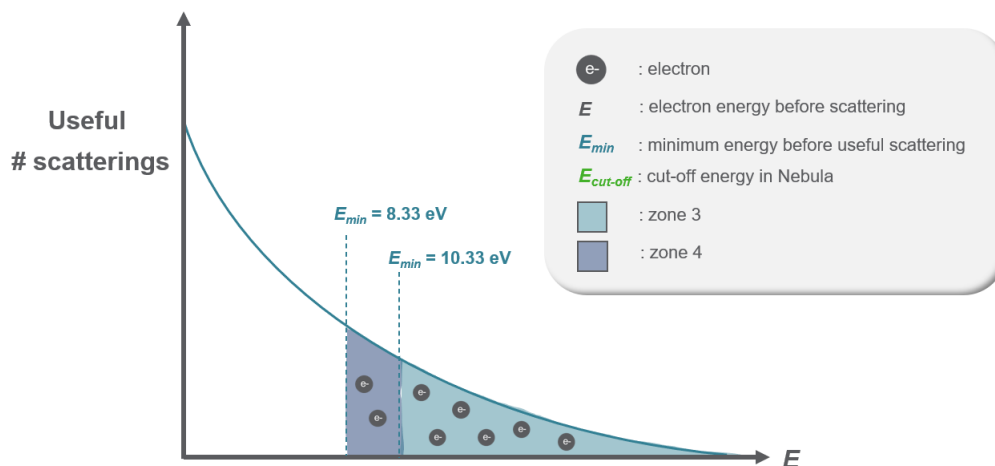


Figure 3.34: Illustration of why the number of useful scatterings decreases when setting VB width from 0 eV to 2 eV at $E = 0$ MV/m

3.8. Compare the influence of Cut-off Energy and VB Width

Referring back to section 3.6, comparing Table 3.15 (cut-off energy at vacuum level and VB width of 2 eV) and Table 3.16 (cut-off energy at CB bottom and VB width of 2 eV), we see that at $E = 0$ MV/m, the number of useful scatterings is the same at around 1.622×10^6 , as E_{min} is 10.33 eV in both cases, as shown in Figure 3.29. However, the percentage increase with varying electric field is significantly different due to the different energy difference between E_{min} and $E_{cut-off}$, which also can be seen in Figure 3.29.

In section 3.7, comparing Table 3.16 (cut-off energy at CB bottom and VB width of 2 eV) and Table 3.17 (cut-off energy at CB bottom and VB width of 0 eV), we see that at $E = 0$ MV/m, the number of useful scatterings differs, with 1.622×10^6 in Table 3.16 and 1.733×10^6 in Table 3.17. However, the percentage increase at varying electric fields is very similar because the energy difference between E_{min} and $E_{cut-off}$ is the same as 4.33 eV. Though the percentage increase might slightly differ due to variations in the potential of electrons in different energy ranges to gain energy from the electric field and the different number of electrons in each energy range.

Combine the simulation results in section 3.6 and section 3.7, it leads to two conclusions:

1. The number of useful scatterings at $E = 0$ MV/m depends on E_{min}
2. The influence of the electric field on the number of useful scatterings mainly depends on the energy difference between E_{min} and $E_{cut-off}$

Without an electric field (i.e., at $E = 0$ MV/m), electrons in zone 1 (from $E_{cut-off}$ to E_{min}) are not useful in our project purpose, as they only lose energy via scattering and cannot jump to zone 3 region to do the chemistry. The number of useful scatterings is defined purely by the electrons in zone 3 ($E > E_{min}$). However, with an external bias, electrons in zone 1 become valuable as they might gain energy from the electric field.

3.9. Compare Mott and Phonon Scattering Models for Sub-100 eV Energies

In section 2.1.2, we discussed that applying phonon scattering for $E < 100$ eV might be more appropriate than simply extending Mott scattering to this region. In this section,

we will compare two cases, observe their response to the electric fields and justify our choice.

3.9.1. Observations in Simulation

First of all, we define two models as follows:

- **Phonon:** Phonon scattering applied in elastic mean free path calculation for $E < 100$ eV (refer to Figure 2.2 (a))
- **Mott:** Mott scattering applied in elastic mean free path calculation for $E < 100$ eV (refer to Figure 2.3)

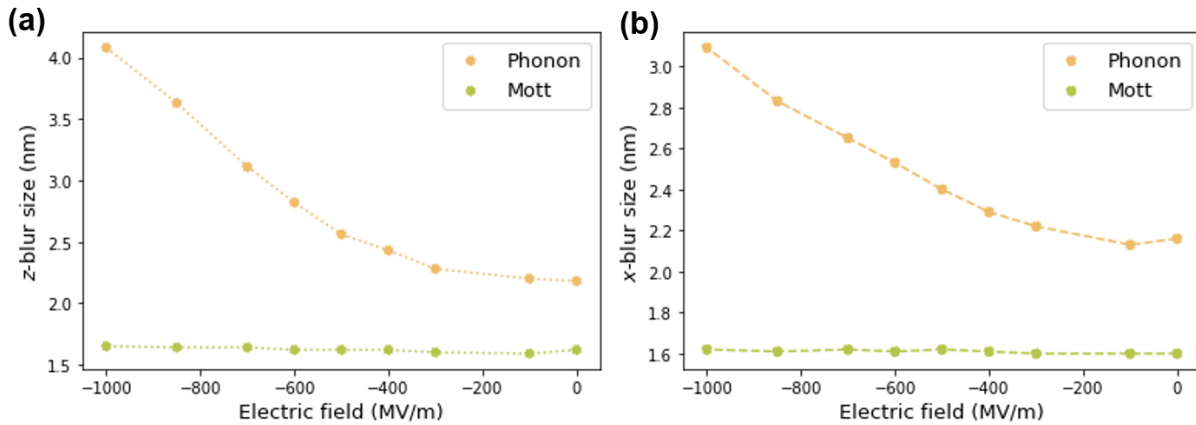


Figure 3.35: Comparison of z-blur and x-blur sizes of two models at varying electric fields

From Figure 3.35, it is evident that Phonon is significantly affected by the electric field: with increasing field strength, both z-blur and x-blur sizes increase. In contrast, Mott remains almost unchanged across the entire range of electric fields.

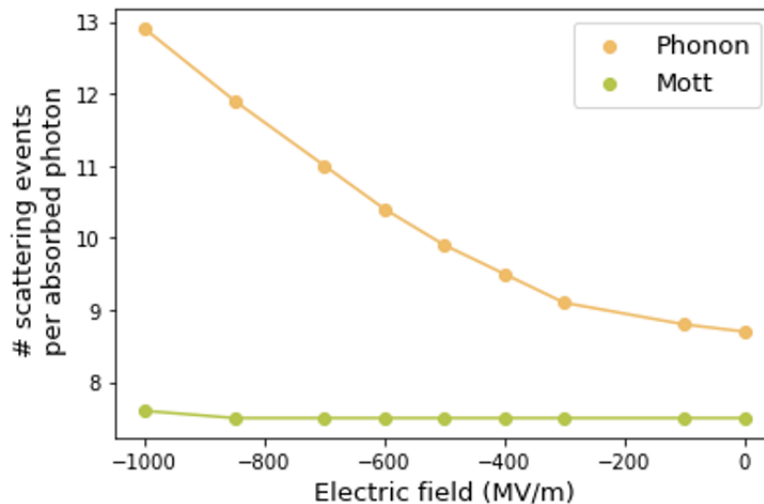


Figure 3.36: Comparison of useful SE yield of two models at varying electric fields

A similar pattern can be observed in Figure 3.36 regarding the number of useful SE yield. This is due to the extremely small elastic mean free path calculated with Mott scattering for $E < 100$ eV.

3.9.2. Conceptual Analysis

Comparing Figure 2.2 (a) and Figure 2.3, we can see that elastic scattering will occur more frequently when applying Mott scattering for $E < 100$ eV than when applying phonon scattering for the same energy range. This is due to the much shorter Mott elastic mean free path in the sub-100 eV region. The increased frequency of elastic scatterings leads to two consequences:

1. The electron blur is smaller (regardless of the electric field).
2. The impact of the electric field is reduced.

For the first point, it is important to note that the “total distance” measured along the trajectory of the electron depends only on the inelastic mean free path if elastic scattering does not cause energy loss. This is because the energy cost per unit travel length without scattering remains the same regardless of whether the electron encounters inelastic or elastic scattering (assuming the same material). Therefore, the total distance should be approximately constant, whether phonon or Mott scattering is applied for $E < 100$ eV, as the inelastic mean free path is identical for both cases. Note that in Nebula simulator, elastic scattering still causes a very small amount of energy loss, so the total distance will not be exactly the same in our case.

If we model electron scattering as a Gaussian random walk, we know that the total distance is proportional to the number of steps, and the end-to-end distance is proportional to the square root of the number of steps, as shown in Equation 3.4.

$$R_{rms} = \sqrt{\langle R^2 \rangle} = \sqrt{Nl^2} = l\sqrt{N} \quad (3.4)$$

Where R_{rms} is the root mean square distance (i.e., end-to-end distance), $\langle R^2 \rangle$ is the mean square displacement, N is the number of steps, and l is the step length. Figure 3.37 compares the end-to-end distance and the ratio of the total distance to the end-to-end distance at different numbers of steps. We can see that under a fixed total distance, a higher number of steps results in a smaller end-to-end distance. This explains why more frequent Mott scatterings lead to smaller electron blur.

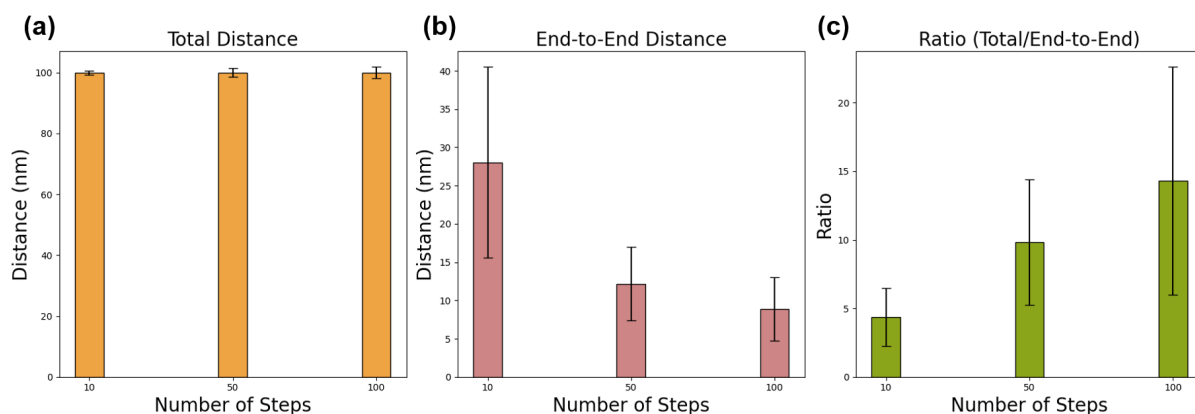


Figure 3.37: Comparison of end-to-end distance at different number of steps under a fixed total distance

Regarding the second point, simulations show that the electric field has less impact when Mott scattering is applied in the sub-100 eV region. This might be because Mott scattering frequently randomizes the electron’s direction, and the travel paths are very

short, making it difficult for the electric field to influence the electron’s direction and speed significantly. As illustrated in Figure 3.38, with the same total distance (i.e., the sum of each travel path), a greater number of scatterings results in a smaller end-to-end distance, and the directions of the electrons become more randomized.

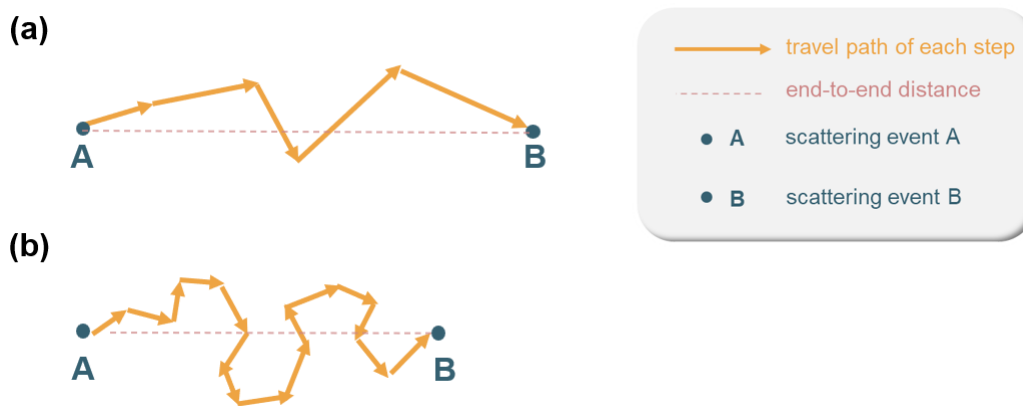


Figure 3.38: Illustration of the random walk of an electron with different number of steps and a fixed total distance

In summary, the frequent elastic scatterings in Mott scattering reduce electron blur and diminish the impact of the electric field due to the increased randomness and shorter travel paths of the electrons.

3.9.3. Quantitative Analysis

Table 3.18 presents the number of total scattering ($dE > 0$), the number of elastic scattering ($0 < dE < 0.05$ eV), the number of inelastic scatterings capable of generating SEs ($dE >$ bandgap), and their ratios relative to the total number of scatterings.

Table 3.18: Comparison of the number of scatterings for two different models at $E = 0$ MV/m

		MOR	
		Phonon	Mott
N_{total} : number of total scatterings	$dE > 0$	2,238,068	5,558,974
$N_{elastic}$: number of elastic scatterings	$0 < dE < 0.05$ eV	2,138,150	5,479,724
$N_{inelastic,SE}$: number of inelastic scatterings that can generate SEs	$dE >$ bandgap	49,331	48,501
$(N_{elastic} / N_{total}) * 100$		95.5 %	98.6 %
$(N_{inelastic,SE} / N_{total}) * 100$		2.2 %	0.87 %

Note 1: dE is the energy loss during the scattering event

Note 2: MOR has a bandgap of 4 eV

Firstly, the number of elastic scattering events is 2.6 times higher in Mott than in Phonon, as the Mott elastic mean free path is much shorter than the inelastic mean free path at $E < 100$ eV, making elastic scattering more likely to happen. Secondly, the number of inelastic scatterings that generate SEs is relatively similar between the two models. This

is because SE generation is dominated by the inelastic mean free path, which remains constant in both models. As discussed in section 2.1.2, the inelastic mean free path depends on the optical properties of the materials and is unaffected by elastic scattering calculations. Note that the two ratios do not sum to 100% because longitudinal optical phonon excitations, counted as inelastic scattering but not generating SEs, is not shown in this table (Details of the physics mechanism has been discussed in section 1.5.2).

Table 3.19: Comparison of electron blur size and the number of useful SE yield per absorbed photon for two different models at $E = 0$ MV/m

	MOR	
	Phonon	Mott
Electron blur	1.09 nm	0.81 nm
Number of useful SE yield per absorbed photon	8.8	7.5

Table 3.19 compares the electron blur and the number of useful SE yield per absorbed photon for both models. The electron blur size is influenced by both elastic and inelastic mean free paths. Mott has a smaller electron blur due to its shorter elastic mean free path. Additionally, Mott also exhibits a smaller SE yield because the relatively high number of elastic scatterings leads to a more pronounced cumulative energy loss, thereby consuming the energy of the electron and decreasing the probability to generate SE.

Given the extremely short mean free path in Mott, as shown in Figure 2.3, which is nearly close to the interatomic distance, and the comparatively small electron blur size of 0.81 nm in the simulation result, Phonon appears to be a better choice. However, it is important to note that, in reality, the elastic scattering mechanism might involve a combination of phonon scattering and Mott scattering. With current technology, the physics of such low-energy electrons in a complex material like MOR remains unknown.

3.10. Feasibility Study

In this section, we will assess the practicality of applying an electric field in the lithography process. Table 3.20 shows the electron blur sizes of MOR without an electric field and at the optimal electric field of -400 MV/m, along with their corresponding illustrations. The electron blur volume (V) is proportional to the square of the x -blur size and multiply with the z -blur size, as shown in Equation 3.5. Thus, we can calculate that the electron blur volume is increased by 26% from 10.17 nm³ to 12.8 nm³ at the optimal electric field.

$$V \propto (\sigma_{x+} + \sigma_{x-})^2 \times (\sigma_{z+} + \sigma_{z-}) \quad (3.5)$$

Table 3.21 presents related parameters to quantify the photon shot noise reduction. The average photon count is proportional to the electron blur volume. Thus, we use electron blur volume directly to quantify how much photon shot noise is mitigated by the increased electron blur.

Assuming each event occurs independently (as is the case in the Nebula simulator) and the average photon count remains constant, we can apply the Poisson distribution to the analysis. This means the standard deviation will be the square root of the mean value, as shown in Equation 3.6.

Table 3.20: Electron blur shape change at the optimal electric field for MOR

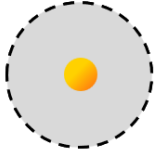
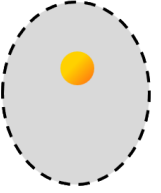
Material	MOR	
Electric field (MV/m)	0	-400
x-blur size (nm)	2.16	2.29
z-blur size (nm)	2.18	2.44
Electron blur volume (nm^3)	10.17	12.8
Illustration of electron blur		

Table 3.21: Evaluation of photon shot noise reduction at the optimal electric field strength for MOR

Material	MOR	
Electric field	0 MV/m	-400 MV/m
Average number of photon count (μ)	10.17	12.8
Standard deviation (σ)	$\sqrt{10.17}$	$\sqrt{12.8}$
Coefficient of variation ($\frac{\sigma}{\mu}$)	$\frac{1}{\sqrt{10.17}}$	$\frac{1}{\sqrt{12.8}}$

$$\mu \propto \sigma^2 \quad (3.6)$$

The coefficient of variation, defined as the standard deviation (σ) divided by the mean value (μ), measures the dispersion of the probability distribution. In our project, it indicates the percentage variation in the number of photons in a unit blur volume, representing photon shot noise.

In the simulation results, we observe that applying an electric field of -400 MV/m on MOR increases the photon counting volume by 26%, but the photon shot noise is only reduced by 11%. This reduction is too small to incentivize commercializing this method. Using a slightly higher EUV dose or tuning the photoresist material to be more sensitive is much cheaper than developing and incorporating the electric field into the current

lithography process. Therefore, even though the electric field achieves our project goal of increasing the z -blur and photon counting volume, the percentage increase is not substantial enough for commercialization. Additionally, -400 MV/m is likely already larger than what is achievable in practice, making the 26% counting volume increase an overestimate.

Moreover, in section 3.1, we identified -400 MV/m as the "optimal" electric field because it homogenizes the electron distribution along the z -direction. However, there is a possibility that anisotropic blur might be a more important factor than a homogeneous profile along the z -direction. In that case, we would need to choose the maximum electric field that does not exceed the material's dielectric strength.

3.11. Alternative Metrics for Analyzing Electron Blur Size

In section 3.3, we initially used a metric encompassing 68% of the total electrons to define the electron blur size. However, we found this metric to be quite sensitive to the tail of the distribution. To address this issue, we will introduce an alternative metric to measure the electron blur size and compare the results obtained from both metrics.

We define two electron blur size measurement metrics as follows:

- **Metric 1:** Blur size = 68% of the total electrons (discussed in section 3.3)
- **Metric 2:** Blur size = $\frac{1}{e}$ of the peak intensity at the center (discussed in section 3.11)

3.11.1. Definition of Blur Size

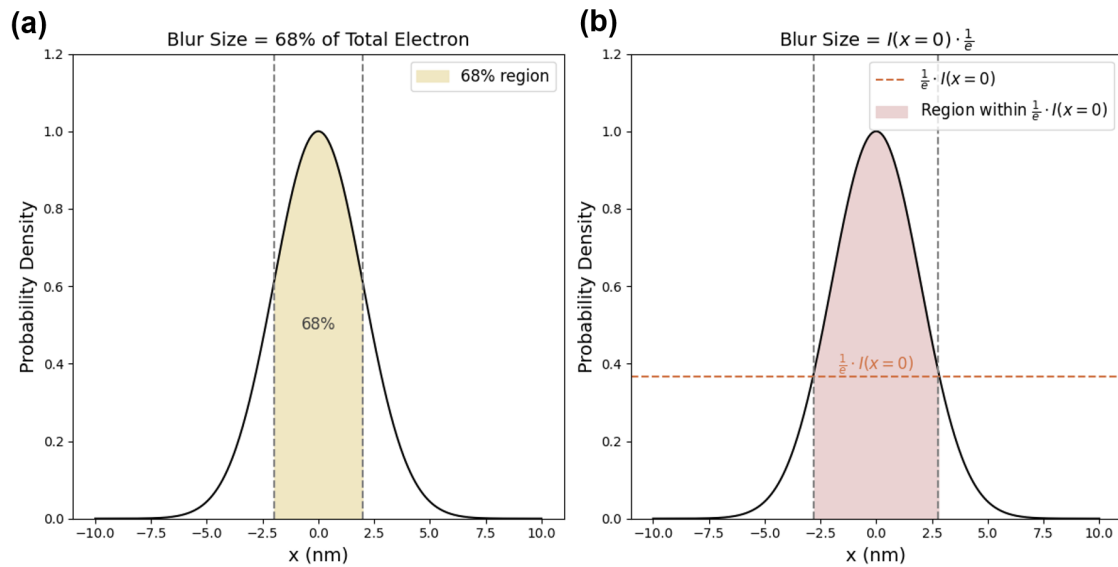


Figure 3.39: Definition of electron blur size. (a) Metric 1: 68% of the total electron distribution (b) Metric 2: The region where the intensity is within $\frac{1}{e}$ of the peak intensity at the center

Figure 3.39 (a) illustrates the original Metric 1 and Figure 3.39 (b) presents the Metric 2. Unlike the original metric, the new metric is less influenced by the tail, as it is based on the peak intensity at the center.

The definition of x -blur and z -blur in Metric 2 are shown in Figure 3.40. In the following sections, we will present the results obtained using the new metric and use MOR as an example. In this section, 600,000 photoelectrons are generated at $x = 0$ nm and $z =$

-10 nm. Given that the $\frac{1}{e}$ of the peak intensity can be quite sensitive to the randomness inherent in the simulation, we increased the number of photoelectrons to 600,000 to minimize the error bars caused by this randomness.

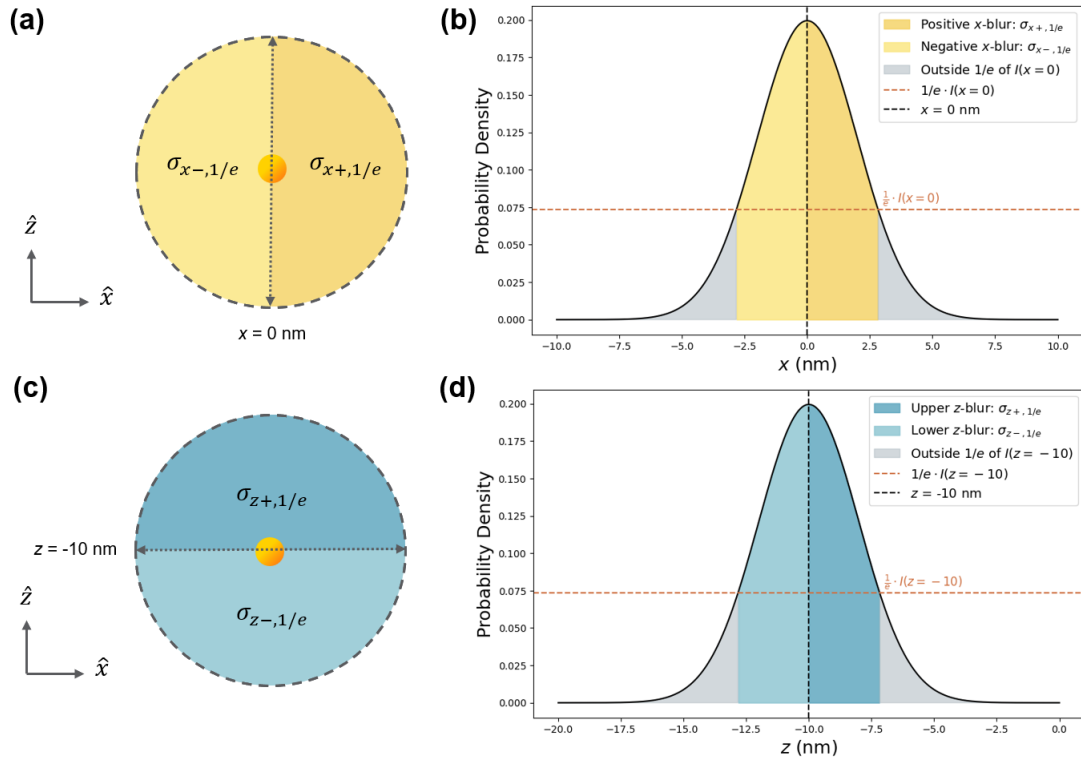


Figure 3.40: Illustration of (a) x -blur definition with new metric (b) spatial distribution along x direction with a center of $x = 0$ nm (c) z -blur definition with new metric (d) spatial distribution along z direction with a center of $z = -10$ nm

3.11.2. x -blur

Figure 3.41 (a) shows the number of useful scatterings along the x -direction, and Figure 3.41 (b) presents its normalized version.

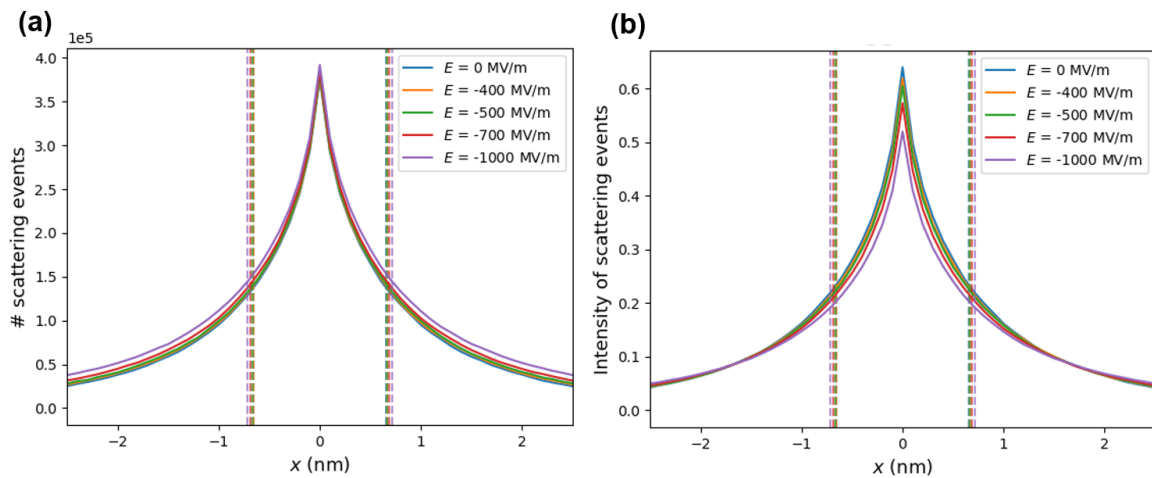


Figure 3.41: MOR (a) Secondary electron distributions along the x -direction (Zoomed-in plot from $x = -2.5$ nm to $x = 2.5$ nm) (b) Normalized zoomed-in plot

Comparing Table 3.4 and Table 3.23, we observe that using Metric 2 results in a less significant percentage increase in x -blur size, with a 9.63% increase at $E = -1000$ MV/m, compared to a 43.06% increase using Metric 1. This implies that the electric field has a more pronounced effect on the tail of the distribution, as more low-energy electrons with large mean free paths are significantly affected by the electric field.

Table 3.22: Quantitative analysis of x -blur of MOR

Electric field (MV/m)	$\sigma_{x+,1/e}$ (nm)	$\sigma_{x-,1/e}$ (nm)	$\sigma_{x+,1/e} + \sigma_{x-,1/e}$ (nm)	Percentage increase (%)
0	0.65	-0.65	1.30	0.00
-100	0.65	-0.65	1.31	0.23
-300	0.66	-0.66	1.32	1.09
-400	0.66	-0.66	1.33	1.68
-500	0.67	-0.67	1.33	2.23
-600	0.67	-0.67	1.35	3.20
-700	0.68	-0.68	1.36	4.32
-850	0.70	-0.70	1.39	6.86
-1000	0.72	-0.72	1.43	9.63

Note: Percentage increase (%) is the x -blur size at varying electric fields relative to the x -blur size at $E = 0$ MV/m

3.11.3. z -blur

Figure 3.42 (a) shows the number of secondary electrons along the z -direction, and Figure 3.42 (b) presents its normalized version.

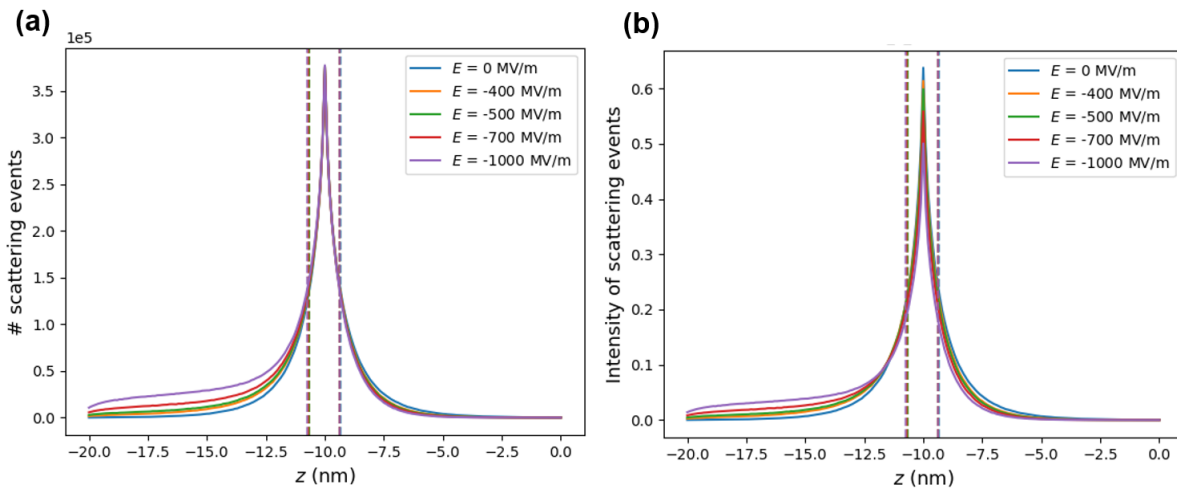


Figure 3.42: MOR (a) Number of along the z -direction (b) Normalized plot

Comparing Table 3.6 and Table 3.23, we see that using Metric 2 results in a much less significant percentage increase in z -blur size, with only a 3.11% increase at $E = -1000$ MV/m, compared to an 87.16% increase using Metric 1. This discrepancy arises because the extended lower z -blur caused by the electric field is primarily in the tail region and most of them are not included in the $\frac{1}{e}$ range of Metric 2.

Table 3.23: Quantitative analysis of z-blur of MOR

Electric field (MV/m)	$\sigma_{z+,1/e}$ (nm)	$\sigma_{z-,1/e}$ (nm)	$\sigma_{z+,1/e} + \sigma_{z-,1/e}$ (nm)	Percentage increase (%)
0	0.65	0.65	1.30	0.00
-100	0.65	0.66	1.31	0.69
-300	0.64	0.67	1.31	0.67
-400	0.64	0.69	1.32	1.47
-500	0.63	0.69	1.31	0.67
-600	0.63	0.70	1.33	1.73
-700	0.62	0.70	1.32	1.49
-850	0.62	0.72	1.33	2.23
-1000	0.61	0.74	1.35	3.11

Note: Percentage increase (%) is the z-blur size at varying electric fields relative to the z-blur size at $E = 0$ MV/m

3.11.4. Anisotropy (S)

Interestingly, with Metric 2, we observe that anisotropy decreases with increasing electric field, as shown in Table 3.24. This is because the percentage increase in x -blur is greater than that in z -blur. This result contrasts with those obtained using Metric 1, where anisotropy increases with the electric field. The primary reason for this difference is that the electric field affects low-energy electrons more significantly, which are predominantly located in the tail region. Metric 1 takes the tail region into account by calculating the total number of electrons, whereas Metric 2 focuses on the peak intensity at the center and sort of excludes the tail region.

Table 3.24: MOR: Compare x -blur and z -blur using anisotropy (S)

Electric field (MV/m)	$\sigma_{z+,1/e} + \sigma_{z-,1/e}$ (nm)	$\sigma_{x+,1/e} + \sigma_{x-,1/e}$ (nm)	S
0	1.30	1.30	1
-100	1.31	1.31	1
-300	1.31	1.32	0.99
-400	1.32	1.33	0.99
-500	1.31	1.33	0.98
-600	1.33	1.35	0.99
-700	1.32	1.36	0.97
-850	1.33	1.39	0.96
-1000	1.35	1.43	0.94

In summary, by using Metric 2 to quantify the electron blur, we found two key points:

1. The electric field affects the tails more than the center.
2. The x -blur increases more than the z -blur when using Metric 2.

For the first point, this is because most low-energy electrons are located in the tail, and the electric field has a more significant effect on low-energy electrons, as discussed in section 3.5. When the electric field influences these electrons in the tail, Metric 2 cannot

measure those changes. This fact might be problematic, as a wide tail might reduce contrast in lithography patterning.

For the second point, since the electric field is applied along the z -direction, the upper z -blur is dragged downwards. Consequently, with Metric 2, the upper z -blur under the influence of the electric field will be much smaller than when using Metric 1, as all upper electrons are concentrated near the center. However, the lower z -blur is not as obviously affected by the electric field because these low-energy electrons are mainly outside the $\frac{1}{e}$ range of the peak intensity.

These findings demonstrate that future investigations into the effects of electric fields need to consider that a single metric might not fully represent the field's impact. Additionally, further studies are needed to determine whether the presence of low-energy electrons in the tail region of the electron distribution is beneficial or detrimental to pattern resolution.

4

Conclusion

The objective of this thesis is to enhance pattern performance under a fixed EUV dose by applying an electric field to the resist layer. The project employs Nebula, an open-source Monte Carlo simulator to simulate the electron-matter interactions inside the resist material. The source code was modified to incorporate the electric field, the material parameters are corrected, and the generation method of photoelectrons is tailored to better reflect real-world conditions. Additionally, several Nebula settings were changed to accommodate MOR material and record only the relevant electron scattering events within the resist.

The simulation results indicate that applying the electric field yields three main benefits for photoresist in EUV lithography:

- **Anisotropic electron blur:** The electron blur is more pronounced in the z -direction than in the x/y directions, reducing LER and increasing the counting volume for each absorbed photon.
- **Asymmetry electron blur in the z -direction:** This leads to more chemical conversion deeper within the resist, alleviating the uneven chemical gradient along the z -direction.
- **Increased SE yield per absorbed photon:** This enhances the probability of each photon performing chemical work, mitigating the photon shot noise problem in EUV lithography.

The optimal electric field for creating anisotropic blur without compromising resolution was found to be -400 MV/m for both MOR and PMMA. At these optimal fields, the z -direction blur is increased by 11.93% while x -direction blur is increased by 6.02% for MOR, with a 3.41% increase in SE yield per absorbed photon. For PMMA, the z -direction blur is increased by 10.17% while the x -direction blur increased by 6.02% with a 3.39% increase in SE yield per absorbed photon.

The simulation result (without an electric field) were validated with experimental data from the literature. The SE yield per absorbed photon for MOR and PMMA were consistent with literature values. The deformation potential in phonon properties of the material file is tuned within a logical range for both materials to obtain a more reasonable electron blur sizes.

Furthermore, we qualitatively and quantitatively analyzed the physics mechanisms

behind several interesting phenomena observed in the simulation. We found that the electric field has a greater effect of lower-energy SEs due to their larger mean free path, amplifying the influence of the electric field. Changing the cut-off energy from the vacuum level to the conduction band bottom magnified the electric field's effect, as electrons between these energy levels can gain energy from the electric field, increasing the useful scatterings. Additionally, correcting the valence band width in the material file from 0 eV to 2 eV reduced the number of useful scatterings depends on the minimum energy required for useful scattering when no external bias is applied, while the influence of the electric field is mainly determined by the energy difference between this minimum energy and the cut-off energy. The model with Mott scattering applied below 100 eV energies region is also compared with the model applied with acoustic phonon scattering. The comparison shows that phonon scattering might be a better choice.

Overall, the simulation results in this study indicate that applying an electric field to MOR can indeed increase the electron blur in z -direction and mitigate the problem of photon shot noise under fixed EUV exposure. However, the magnitude of improvement is not substantial enough to counteract the cost and effort of incorporating electric field setup into the current lithography process. It should be noted that our investigation was conducted entirely through computational methods. Despite our best efforts to accurately model the physics involved, the simulation has several limitations, which will be discussed in the next chapter. Therefore, we recommend experimental validation of the model.

5

Recommendations

In Chapter 5, the limitations of simulation will be discussed in section 5.1, and how the simulation model can be tuned and further improved by experiments will be elaborated in section 5.2.

5.1. Limitations of Simulation

Firstly, the electronic band structure utilized in Nebula is simplified. In reality, there is no clear boundary between the valence band, conduction band and band gap. The band is composed of several orbitals that might overlap. However, to simulate the electronic excitation and electron scattering events in detail, a simplified band structure is useful to mimic the most probable events.

Secondly, some material properties are difficult to find in the literature. For instance, as discussed in section 2.1.3, the valence band width is initially set to 0 eV by default, which is not physically accurate. Measuring the exact valence band width experimentally is challenging, and values calculated from DFT might not reflect the real situation. Moreover, the relevant studies of MOR is restricted to the MOR vendors themselves and not publicly accessible. Consequently, the band gap information is roughly estimated from optical data, and the electron affinity is found in only one source. Moreover, obtaining phonon properties is essential for calculating the elastic mean free path in the $E < 100$ eV region. Unfortunately, the phonon parameters for both MOR and PMMA remain unknown and are challenging to determine experimentally due to their complex structures. Also, distinguishing phonon scattering from other types of scattering is very challenging. Therefore, as detailed in section 3.4, the deformation potentials for both MOR and PMMA were adjusted until the simulated electron blur sizes matched the values reported in the literature.

Thirdly, the physical mechanisms below 100 eV may involve a combination of acoustic phonon scattering and Mott scattering, rather than purely acoustic phonon scattering alone. However, understanding the behavior of low-energy electrons in complex materials such as MOR and PMMA remains incomplete due to current technological limitations. Additionally, the acoustic phonon scattering model applied here is primarily developed for crystalline materials, potentially leading to discrepancies in how electrons behave between crystalline materials and amorphous materials like MOR and PMMA.

Finally, the Nebula simulator does not include all physics mechanisms. Actually, no

existing simulator can perfectly replicate the real scenarios. Details on what is missing in Nebula can be found in Chapter 6 in the work done by Luc van Kessel [60].

5.2. Future Work

Several parameters in this simulation model can be tuned to calibrate the experimental data. For example, as shown in section 2.2.2, the energy loss filter is set to 4.33 eV for MOR based on literature values, and 6.6 eV for PMMA, assuming 1 eV is sufficient for chemistry. Experiments, such as atomic force microscopy (AFM) combined with low-energy electron microscopy (LEEM), can be conducted on MOR and PMMA (or CAR) to determine the exact energy needed to induce chemical reactions by monitoring the relationship between resist thickness loss and the energy of the incoming electron beam.

Moreover, in this project, as discussed in section 2.2.2, we assume an electron is needed to drive chemical reactions and thus exclude the effect of phonon scattering. However, as noted in many studies, the chemical reactions inside the resist material under EUV exposure are not well understood. There might be a chance that energy loss via phonon scattering can facilitate ligand dissociation in MOR and acid generation in CAR. This can be tested by calibrating the energy loss filter in the model and comparing it with experimental results. For example, if the number of chemical reactions per absorbed photon exceeds the SE yield per absorbed photon, it might indicate that phonon scattering contribute to the chemistry.

Furthermore, the current version of Nebula does not include a polaron trapping mechanism. When electrons (or holes) move through a solid, the material polarizes, slowing the electron down. This interaction can distort the surrounding structure, creating a “bubble” of distortion that moves along with the electron. The combination of the electron and the surrounding distortion is called a polaron, as shown in Figure 5.1 [41].

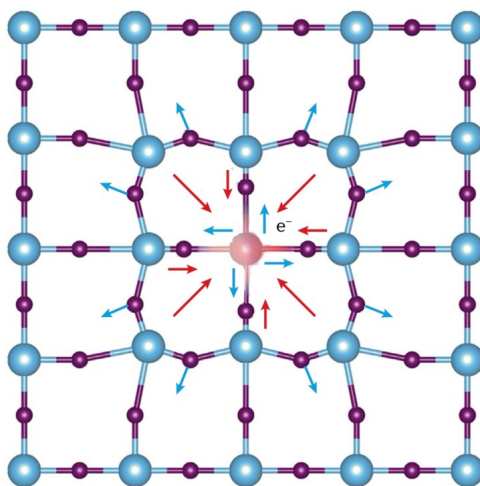


Figure 5.1: Schematic illustration of the formation of a polaron [41]

Polarons can get trapped at certain sites within materials, such as defects and impurities. The mechanism of polaron trapping is more significant for low-energy electrons [45]. Low-energy electrons (i.e., those with low kinetic energy) move more slowly, increasing the likelihood of the polaron interacting strongly with the material and getting stuck in a trapping site. At higher energy, the polaron moves faster and is less likely to get trapped

because it can zip past potential trapping sites more easily. Polaron trapping is more effective in polymers like PMMA than in crystalline materials like silicon [102]. Polymers have more irregularities, such as chain ends, folds, and varying chain orientations, which can act as trapping sites for polarons. Additionally, polymers are more flexible and more easily distorted, making them more conducive to polaron trapping.

If we include polaron trapping in Nebula, we expect three kinds of effects:

1. **Decrease in electron blur:** Trapped polarons reduce the overall spread of electrons in the material.
2. **Decrease in SE yield:** Trapped polarons cannot produce SE, leading to lower SE yield.
3. **Decrease in electric field effect:** Since polaron trapping is more effective for low-energy electrons, and the electric field has a more significant effect on low-energy electrons, the overall impact of the electric field might be reduced.

Lastly, the material parameters used in this project are not from a single source but from various experimental values in different literature. More specific material parameters for MOR, PMMA and CAR should be obtained from XPS experiments, using consistent experimental methods. PMMA is used in this project because CAR is not accessible due to intellectual property rights of vendors. However, collaboration with vendors might allow access to both MOR and CAR, enabling in-house experiments. This would ensure the quality of material parameters used in the model and make the comparison of simulation results between MOR and CAR more meaningful.

References

- [1] Haider Ali et al. "A survey on system level energy optimisation for MPSoCs in IoT and consumer electronics". In: *Computer Science Review* 41 (2021), p. 100416.
- [2] T Allenet et al. "EUV resist screening update: progress towards high-NA lithography". In: *Advances in Patterning Materials and Processes XXXIX*. Vol. 12055. SPIE. 2022, pp. 111–120.
- [3] T Allenet et al. "Image blur investigation using EUV-interference lithography". In: *Extreme Ultraviolet Lithography 2020*. Vol. 11517. SPIE. 2020, pp. 36–44.
- [4] T Allenet et al. "Progress in EUV resist screening by interference lithography for high-NA lithography". In: *International Conference on Extreme Ultraviolet Lithography 2021*. Vol. 11854. SPIE. 2021, pp. 81–90.
- [5] Vadim Banine and Roel Moors. "Plasma sources for EUV lithography exposure tools". In: *Journal of Physics D: Applied Physics* 37.23 (2004), p. 3207.
- [6] VY Banine. "EUV lithography: Historical perspective and road ahead". In: (2014).
- [7] Zelalem Belete et al. "Stochastic simulation and calibration of organometallic photoresists for extreme ultraviolet lithography". In: *Journal of Micro/Nanopatterning, Materials, and Metrology* 20.1 (2021), pp. 014801–014801.
- [8] Ivan Bernalov et al. "Key role of very low energy electrons in tin-based molecular resists for extreme ultraviolet nanolithography". In: *ACS applied materials & interfaces* 12.8 (2020), pp. 9881–9889.
- [9] Ivan Bernalov et al. "Patterning Sn-based EUV resists with low-energy electrons". In: *arXiv preprint arXiv:1910.02511* (2019).
- [10] John J Biafore et al. "Pattern prediction in EUV resists". In: *Lithography Asia 2009*. Vol. 7520. SPIE. 2009, pp. 538–550.
- [11] John J Biafore et al. "Resist pattern prediction at EUV". In: *Extreme Ultraviolet (EUV) Lithography*. Vol. 7636. SPIE. 2010, pp. 250–259.
- [12] John J Biafore et al. "Statistical simulation of resist at EUV and ArF". In: *Advances in Resist Materials and Processing Technology XXVI*. Vol. 7273. SPIE. 2009, pp. 1207–1216.
- [13] X-Ray Data Booklet. "X-ray Data Booklet". In: *Laboratory, Univ. California* (2001).
- [14] Robert Brainard et al. "Photons, electrons, and acid yields in EUV photoresists: a progress report". In: *Advances in Resist Materials and Processing Technology XXV*. Vol. 6923. SPIE. 2008, pp. 662–675.
- [15] Stefan Braun and Andreas Leson. "Optical Elements for EUV Lithography and X-ray Optics". In: *The Nano-Micro Interface: Bridging the Micro and Nano Worlds* (2015), pp. 613–628.
- [16] Timothy A Brunner et al. "Line-edge roughness performance targets for EUV lithography". In: *Extreme Ultraviolet (EUV) Lithography VIII*. Vol. 10143. SPIE. 2017, pp. 48–57.

- [17] Elizabeth Buitrago et al. "EUV lithography process challenges". In: *Frontiers of Nanoscience*. Vol. 11. Elsevier, 2016, pp. 135–176.
- [18] Sonia Castellanos et al. "EUV metal oxide resists: impact of the environment composition on CD during post-exposure delay". In: *Advances in Patterning Materials and Processes XLI*. Vol. 12957. SPIE. 2024, pp. 23–27.
- [19] Chetvorno. <https://commons.wikimedia.org/w/index.php?curid=56983339>. Accessed: 2024-06-12.
- [20] Heon Choi and Ayman Hamouda. "Inverse lithography OPC correction with multiple patterning and etch awareness". In: *Optical Microlithography XXXI*. Vol. 10587. SPIE. 2018, pp. 193–203.
- [21] Kristina D Closser et al. "The importance of inner-shell electronic structure for enhancing the EUV absorption of photoresist materials". In: *The Journal of chemical physics* 146.16 (2017).
- [22] Pooya Davari. "High frequency high power converters for industrial applications". PhD thesis. Queensland University of Technology, 2013.
- [23] Denis David and Christian Godet. "Derivation of dielectric function and inelastic mean free path from photoelectron energy-loss spectra of amorphous carbon surfaces". In: *Applied Surface Science* 387 (2016), pp. 1125–1139.
- [24] VT Davis. *Introduction to Photoelectron Angular Distributions: Theory and Applications*. Vol. 286. Springer Nature, 2022.
- [25] Peter De Bisschop and Eric Hendrickx. "Stochastic effects in EUV lithography". In: *Extreme Ultraviolet (EUV) Lithography IX*. Vol. 10583. SPIE. 2018, pp. 350–366.
- [26] Peter De Bisschop and Eric Hendrickx. "Stochastic printing failures in EUV lithography". In: *Extreme Ultraviolet (EUV) Lithography X*. Vol. 10957. SPIE. 2019, pp. 37–56.
- [27] Peter De Schepper et al. "MOx resist formulation and process advances towards high-NA EUV lithography". In: *Advances in Patterning Materials and Processes XL*. Vol. 12498. SPIE. 2023, p. 1249804.
- [28] Anuja De Silva et al. "Fundamentals of resist stochastic effect for single-expose EUV patterning". In: *Extreme Ultraviolet (EUV) Lithography X*. Vol. 10957. SPIE. 2019, pp. 57–67.
- [29] Anuja De Silva et al. "Single-expose patterning development for EUV lithography". In: *Extreme Ultraviolet (EUV) Lithography VIII*. Vol. 10143. SPIE. 2017, pp. 311–319.
- [30] Danilo De Simone, Yannick Vesters, and Geert Vandenberghe. "Photoresists in extreme ultraviolet lithography (EUVL)". In: *Advanced Optical Technologies* 6.3-4 (2017), pp. 163–172.
- [31] Danilo De Simone et al. "Exploring the readiness of EUV photo materials for patterning advanced technology nodes". In: *Extreme Ultraviolet (EUV) Lithography VIII*. Vol. 10143. SPIE. 2017, pp. 153–169.
- [32] Florian Delachat et al. "Determination of spot size and acid diffusion length in positive chemically amplified resist for e-beam lithography at 100 and 5 kV". In: *Journal of Vacuum Science & Technology B* 32.6 (2014).

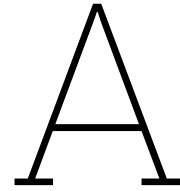
- [33] D Drygiannakis et al. "Simulation of the combined effects of polymer size, acid diffusion length, and EUV secondary electron blur on resist line-edge roughness". In: *Advances in Resist Materials and Processing Technology XXIV*. Vol. 6519. SPIE. 2007, pp. 1129–1140.
- [34] Roberto Fallica et al. "Absorption coefficient and exposure kinetics of photoresists at EUV". In: *Extreme Ultraviolet (EUV) Lithography VIII*. Vol. 10143. SPIE. 2017, pp. 29–39.
- [35] Roberto Fallica et al. "Absorption coefficient of metal-containing photoresists in the extreme ultraviolet". In: *Journal of Micro/Nanolithography, MEMS, and MOEMS* 17.2 (2018), pp. 023505–023505.
- [36] Roberto Fallica et al. "Dynamic absorption coefficients of chemically amplified resists and nonchemically amplified resists at extreme ultraviolet". In: *Journal of Micro/Nanolithography, MEMS, and MOEMS* 15.3 (2016), pp. 033506–033506.
- [37] Roberto Fallica et al. "Mean Free Path of Electrons in Organic Photoresists for Extreme Ultraviolet Lithography in the Kinetic Energy Range 20–450 eV". In: *ACS Applied Materials & Interfaces* 15.29 (2023), pp. 35483–35494.
- [38] Roberto Fallica et al. "The hidden energy tail of low energy electrons in EUV lithography". In: *Advances in Patterning Materials and Processes XXXVI*. Vol. 10960. SPIE. 2019, pp. 7–15.
- [39] H-J Fitting et al. "Attenuation and escape depths of low-energy electron emission". In: *Journal of Electron Spectroscopy and Related Phenomena* 119.1 (2001), pp. 35–47.
- [40] HJ Fitting, E Schreiber, and IA Glavatskikh. "Monte Carlo modeling of electron scattering in nonconductive specimens". In: *Microscopy and Microanalysis* 10.6 (2004), pp. 764–770.
- [41] Cesare Franchini et al. "Polarons in materials". In: *Nature Reviews Materials* 6.7 (2021), pp. 560–586.
- [42] Junichi Fujimoto et al. "Development of laser-produced tin plasma-based EUV light source technology for HVM EUV lithography". In: *Physics Research International* 2012 (2012).
- [43] Gregg M Gallatin. "Resist blur and line edge roughness". In: *Optical Microlithography XVIII*. Vol. 5754. SPIE. 2005, pp. 38–52.
- [44] Gregg M Gallatin, Patrick Naulleau, and Robert Brainard. "Fundamental limits to EUV photoresist". In: *Advances in Resist Materials and Processing Technology XXIV*. Vol. 6519. SPIE. 2007, pp. 387–396.
- [45] JP Ganachaud and A Mokrani. "Theoretical study of the secondary electron emission of insulating targets". In: *Surface Science* 334.1-3 (1995), pp. 329–341.
- [46] Marziogiuseppe Gentile et al. "Dissociative photoionization of EUV lithography photoresist models". In: *Advances in Patterning Materials and Processes XL*. Vol. 12498. SPIE. 2023, pp. 124–133.
- [47] Jesse L Grayson et al. "Indium nitrate hydrate films as potential EUV resists: film formation, characterization, and solubility switch assessment using a 92-eV electron beam". In: *Journal of Micro/Nanopatterning, Materials, and Metrology* 23.1 (2024), pp. 014601–014601.
- [48] Andrew Grenville et al. "Integrated fab process for metal oxide EUV photoresist". In: *Advances in Patterning Materials and Processes XXXII*. Vol. 9425. SPIE. 2015, pp. 225–232.

- [49] Roel Gronheid, Alex Vaglio Pret, and Anatoly Burov. "Depth of focus in high-NA EUV lithography: the role of assist features and their variability budget". In: *Optical and EUV Nanolithography XXXVI*. Vol. 12494. SPIE. 2023, pp. 213–221.
- [50] Steven Grzeskowiak et al. "Acid generation efficiency of EUV PAGs via low energy electron exposure". In: *Journal of Photopolymer Science and Technology* 29.3 (2016), pp. 453–458.
- [51] Joshua A Hagen et al. "Enhanced emission efficiency in organic light-emitting diodes using deoxyribonucleic acid complex as an electron blocking layer". In: *Applied Physics Letters* 88.17 (2006).
- [52] Burton L Henke, Eric M Gullikson, and John C Davis. "X-ray interactions: photoabsorption, scattering, transmission, and reflection at $E= 50\text{-}30,000$ eV, $Z= 1\text{-}92$ ". In: *Atomic data and nuclear data tables* 54.2 (1993), pp. 181–342.
- [53] R Hernández et al. "Study of photosensitive dry films absorption for printed circuit boards by photoacoustic technique". In: *International Journal of Thermophysics* 38 (2017), pp. 1–10.
- [54] William D Hinsberg and Stephen Meyers. "A numeric model for the imaging mechanism of metal oxide EUV resists". In: *Advances in Patterning Materials and Processes XXXIV*. Vol. 10146. SPIE. 2017, pp. 14–24.
- [55] imec. *Challenges and innovations in patterning*. Last accessed 30 May 2024. 2023. URL: <https://www.imec-int.com/en/articles/challenges-and-innovations-patterning>.
- [56] Kenji Ishikawa et al. "Progress in nanoscale dry processes for fabrication of high-aspect-ratio features: How can we control critical dimension uniformity at the bottom?" In: *Japanese Journal of Applied Physics* 57.6S2 (2018), 06JA01.
- [57] Mengran Ji, Ryo Nagata, and Kiichiro Uchino. "Effect of Hydrogen Ion Energy in the Process of Reactive Ion Etching of Sn Thin Films by Hydrogen Plasmas". In: *Plasma and Fusion Research* 16 (2021), pp. 1406003–1406003.
- [58] Mark van de Kerkhof et al. "EUV-induced hydrogen plasma and particle release". In: *Radiation Effects and Defects in Solids* 177.5-6 (2022), pp. 486–512.
- [59] Mark van de Kerkhof et al. "Particulate and molecular contamination control in EUV-induced H₂-plasma in EUV lithographic scanner". In: *Systems Contamination: Prediction, Control, and Performance 2020*. Vol. 11489. SPIE. 2020, pp. 79–95.
- [60] LCPM van Kessel and CW Hagen. "Nebula: Monte Carlo simulator of electron-matter interaction". In: *SoftwareX* 12 (2020), p. 100605.
- [61] Erik Kieft and Eric Bosch. "Refinement of Monte Carlo simulations of electron-specimen interaction in low-voltage SEM". In: *Journal of Physics D: Applied Physics* 41.21 (2008), p. 215310.
- [62] Sangjin Kim et al. "An investigation on the process control for the solid application of EUV MOR". In: *Optical and EUV Nanolithography XXXVI*. Vol. 12494. SPIE. 2023, pp. 294–299.
- [63] Seong-Sue Kim et al. "Progress in EUV lithography toward manufacturing". In: *Extreme Ultraviolet (EUV) Lithography VIII*. Vol. 10143. SPIE. 2017, p. 1014306.
- [64] Takahiro Kozawa and Seiichi Tagawa. "Radiation chemistry in chemically amplified resists". In: *Japanese Journal of Applied Physics* 49.3R (2010), p. 030001.

- [65] Takahiro Kozawa et al. "Acid generation efficiency in a model system of chemically amplified extreme ultraviolet resist". In: *Journal of Vacuum Science & Technology B: Microelectronics and Nanometer Structures Processing, Measurement, and Phenomena* 24.6 (2006), pp. L27–L30.
- [66] Richard A Lawson and Alex PG Robinson. "Overview of materials and processes for lithography". In: *Frontiers of Nanoscience*. Vol. 11. Elsevier, 2016, pp. 1–90.
- [67] Li Li et al. "Extreme ultraviolet resist materials for sub-7 nm patterning". In: *Chemical Society Reviews* 46.16 (2017), pp. 4855–4866.
- [68] Leipeng Liu et al. "Enhanced energy storage properties of all-polymer dielectrics by cross-linking". In: *Reactive and Functional Polymers* 192 (2023), p. 105699.
- [69] Luke T Long, Andrew R Neureuther, and Patrick P Naulleau. "Three-dimensional modeling of EUV photoresist using the multivariate Poisson propagation model". In: *Journal of Micro/Nanopatterning, Materials, and Metrology* 20.3 (2021), pp. 034601–034601.
- [70] Chaoyun Luo et al. "Review of recent advances in inorganic photoresists". In: *RSC advances* 10.14 (2020), pp. 8385–8395.
- [71] Jonathan H Ma et al. "Excitation selectivity in model tin-oxo resist: a computational chemistry perspective". In: *Extreme Ultraviolet (EUV) Lithography XI*. Vol. 11323. SPIE. 2020, pp. 349–355.
- [72] Chris A Mack. "Reducing roughness in extreme ultraviolet lithography". In: *Journal of Micro/Nanolithography, MEMS, and MOEMS* 17.4 (2018), pp. 041006–041006.
- [73] O Madelung, U Rössler, M Schulz, et al. "Group IV Elements, IV-IV and III-V Compounds. Part b-Electronic, Transport, Optical and Other Properties". In: *Semiconductors (Springer, Berlin, 2001)* (2002).
- [74] S Mähl et al. "Analysis of XPS valence band spectra of polymers using a density-functional theory based calculation of model oligomers". In: *Journal of Polymer Science Part A: Polymer Chemistry* 37.1 (1999), pp. 95–103.
- [75] Theodore Manouras and Panagiotis Argitis. "High sensitivity resists for EUV lithography: a review of material design strategies and performance results". In: *Nanomaterials* 10.8 (2020), p. 1593.
- [76] Thomas Marschner et al. "193-nm resist roughness characterization and process propagation investigation using a CD-SEM". In: *Metrology, Inspection, and Process Control for Microlithography XVIII*. Vol. 5375. SPIE. 2004, pp. 477–485.
- [77] *MS Windows NT Kernel Description*. <https://www.nanoscience.com/blogs/which-electron-detector-is-right-for-your-application/>. Accessed: 2024-05-13.
- [78] Seiji Nagahara et al. "Recent advances in EUV patterning in preparation towards high-NA EUV". In: *Advances in Patterning Materials and Processes XL* 12498 (2023), pp. 287–296.
- [79] Amrit Narasimhan et al. "Studying thickness loss in extreme ultraviolet resists due to electron beam exposure using experiment and modeling". In: *Journal of Micro/Nanolithography, MEMS, and MOEMS* 14.4 (2015), pp. 043502–043502.
- [80] Christopher K Ober et al. "EUV photolithography: resist progress and challenges". In: *Extreme Ultraviolet (EUV) Lithography IX* 10583 (2018), pp. 15–27.

- [81] Isabel Pastoriza-Santos et al. "Plasmonic polymer nanocomposites". In: *Nature Reviews Materials* 3.10 (2018), pp. 375–391.
- [82] David R Penn. "Electron mean-free-path calculations using a model dielectric function". In: *Physical Review B* 35.2 (1987), p. 482.
- [83] Alessandro Vaglio Pret et al. "Modeling and simulation of low-energy electron scattering in organic and inorganic EUV photoresists". In: *Advances in Patterning Materials and Processes XXXIV*. Vol. 10146. SPIE. 2017, pp. 48–63.
- [84] Benjamin Rathsack et al. "Resist fundamentals for resolution, LER, and sensitivity (RLS) performance tradeoffs and their relation to micro-bridging defects". In: *Advances in Resist Materials and Processing Technology XXVI*. Vol. 7273. SPIE. 2009, pp. 1246–1256.
- [85] Markus Rohdenburg et al. "Role of low-energy electrons in the solubility switch of Zn-based oxocluster photoresist for extreme ultraviolet lithography". In: *Physical Chemistry Chemical Physics* 23.31 (2021), pp. 16646–16657.
- [86] Max Roser and Hannah Ritchie. *Transistor Count over time*. A logarithmic graph showing the timeline of how transistor counts in microchips are almost doubling every two years from 1970 to 2020; Moore's Law. 2020. URL: <https://ourworldindata.org/uploads/2020/11/Transistor-Count-over-time.png> (visited on 02/12/2024).
- [87] Kaushik Sah et al. "EUV stochastic defect monitoring with advanced broadband optical wafer inspection and e-beam review systems". In: *International Conference on Extreme Ultraviolet Lithography 2018*. Vol. 10809. SPIE. 2018, pp. 40–51.
- [88] Saptadip Saha et al. "Fabrication of hybrid ultraviolet photodetector using organic polymer thin-film-coated TiO₂ nanowires". In: *Journal of Nanophotonics* 10.2 (2016), pp. 026011–026011.
- [89] William R Salaneck. "Photoelectron spectroscopy of the valence electronic structure of polymers". In: *Critical Reviews in Solid State and Material Sciences* 12.4 (1984), pp. 267–296.
- [90] Samsung. *GAA Structure Transistors*. transistor structure. 2019. URL: <https://semiconductor.samsung.com/support/tools-resources/dictionary/gaa-transistors-a-next-generation-process-for-next-generation-semiconductors/> (visited on 03/04/2024).
- [91] E Schreiber and H-J Fitting. "Monte Carlo simulation of secondary electron emission from the insulator SiO₂". In: *Journal of Electron Spectroscopy and Related Phenomena* 124.1 (2002), pp. 25–37.
- [92] Joren Severi et al. "Power spectral density as template for modeling a metal-oxide nanocluster resist to obtain accurate resist roughness profiles". In: *Journal of Micro/Nanopatterning, Materials, and Metrology* 20.2 (2021), pp. 024601–024601.
- [93] Vidharshana Sivakumar. "Monte-Carlo Simulations of Secondary Electron Scattering on 2-D Materials". In: TU Delft, 2024.
- [94] W Steinhögl et al. "Impact of line edge roughness on the resistivity of nanometer-scale interconnects". In: *Microelectronic Engineering* 76.1-4 (2004), pp. 126–130.
- [95] Jason Stowers et al. "Metal oxide EUV photoresist performance for N7 relevant patterns and processes". In: *Advances in Patterning Materials and Processes XXXIII*. Vol. 9779. SPIE. 2016, p. 977904.

- [96] Akiyoshi Suzuki. "Advances in Optics and Exposure Devices Employed in Excimer Laser/EUV Lithography". In: *Handbook of Laser Micro-and Nano-Engineering* (2020), pp. 1–42.
- [97] Shigeo Tanuma, Cedric J Powell, and David R Penn. "Calculations of electron inelastic mean free paths. V. Data for 14 organic compounds over the 50–2000 eV range". In: *Surface and interface analysis* 21.3 (1994), pp. 165–176.
- [98] Justin Torok et al. "Secondary electrons in EUV lithography". In: *Journal of Photopolymer Science and Technology* 26.5 (2013), pp. 625–634.
- [99] N Ueno et al. "Quasi-molecular angle dependence of photoemission from thin films of polystyrene". In: *Journal of electron spectroscopy and related phenomena* 36.2 (1985), pp. 143–151.
- [100] Nobuo Ueno. "Angle-resolved UPS of ultrathin films of functional organic molecules with synchrotron radiation: Determination of molecular orientation by quantitative analysis of photoelectron angular distribution". In: *Journal of electron spectroscopy and related phenomena* 78 (1996), pp. 345–350.
- [101] Ivan A Vartanyants and Jörg Zegenhagen. "Theory of photoelectron emission from an x-ray interference field". In: *The X-Ray Standing Wave Technique: Principles and Applications*. World Scientific, 2013, pp. 181–215.
- [102] Thomas Verduin. "Quantum noise effects in e-beam lithography and metrology". In: *TU Delft* (2017).
- [103] Maarten Vos and Pedro L Grande. "Extracting the dielectric function from high-energy REELS measurements". In: *Surface and Interface Analysis* 49.9 (2017), pp. 809–821.
- [104] Xiaolin Wang et al. "Trends in photoresist materials for extreme ultraviolet lithography: A review". In: *Materials Today* (2023).
- [105] Zhihao Wang et al. "Recent advances in organic-inorganic hybrid photoresists". In: *J. Microelectron. Manuf.* 4 (2021), p. 21040101.
- [106] ZL Wang. "Valence electron excitations and plasmon oscillations in thin films, surfaces, interfaces and small particles". In: *Micron* 27.3-4 (1996), pp. 265–299.
- [107] Wolfgang SM Werner. "Dielectric function of Cu, Ag, and Au obtained from reflection electron energy loss spectra, optical measurements, and density functional theory". In: *Applied physics letters* 89.21 (2006).
- [108] De-Kun Yang et al. "The development of laser-produced plasma EUV light source". In: *Chip* 1.3 (2022), p. 100019.
- [109] Oktay Yildirim et al. "Improvements in resist performance towards EUV HVM". In: *Extreme Ultraviolet (EUV) Lithography VIII*. Vol. 10143. SPIE. 2017, pp. 153–164.
- [110] F Yubero et al. "Dielectric loss function of Si and SiO₂ from quantitative analysis of REELS spectra". In: *Surface and interface analysis* 20.8 (1993), pp. 719–726.
- [111] Yu Zhang et al. "Extreme ultraviolet photoemission of a tin-based photoresist". In: *Applied Physics Letters* 118.17 (2021).



Material Properties

In Appendix A.1 and A.3, the material parameters of MOR and PMMA are shown respectively. In Appendix A.2 and A.4, the optical data of MOR and PMMA are presented, where for each column, the first parameter is the photon energy and the second parameter is ELF at near zero momentum, as shown in Figure 2.1.

A.1. MOR material parameters

name: inpria_30keV
density: 2.5 g/cm³

elements:

Sn: { count: 12, Z: 50, M: 118.71 g/mol }
C: { count: 48, Z: 6, M: 12.011 g/mol }
H: { count: 116, Z: 1, M: 1.008 g/mol }
O: { count: 22, Z: 8, M: 15.999 g/mol }

band_structure:

model: insulator
valence: 2 eV # set a value other than 0, no literature proof.
band_gap: 4 eV # Estimated from optical data
affinity: 1.13 eV # from : doi: 10.1117/12.2553055

optical:

df_file: df_inpria_30keV.dat

phonon:

lattice: 1.54 Å # C-C bond length

isotropic:

ac_def: 3 eV # Unknown, tuned such that reasonable mean free
paths were obtained

longitudinal:

c_s: 2746 m/s # PMMA

transversal:

c_s: 1392 m/s # PMMA

A.2. MOR optical data

-1	12.746 0.473	41.416 0.123
0.001 1e-10	13.148 0.531	42.721 0.118
4.304 1e-10	13.562 0.579	44.066 0.111
4.305 0.004	13.989 0.628	45.454 0.104
4.441 0.013	14.43 0.683	46.886 0.099
4.581 0.023	14.884 0.763	48.362 0.094
4.725 0.032	15.353 0.823	49.886 0.091
4.874 0.04	15.837 0.893	51.457 0.09
5.027 0.047	16.335 0.95	53.078 0.088
5.186 0.054	16.85 0.988	54.75 0.083
5.349 0.066	17.381 0.944	56.474 0.077
5.518 0.079	17.928 0.857	58.253 0.075
5.691 0.079	18.493 0.906	60.088 0.075
5.871 0.082	19.075 0.905	61.98 0.075
6.056 0.088	19.676 0.87	63.932 0.07
6.246 0.088	20.296 0.885	65.946 0.066
6.443 0.09	20.935 0.889	68.023 0.063
6.646 0.102	21.594 0.838	70.166 0.06
6.855 0.119	22.275 0.78	72.376 0.055
7.071 0.124	22.976 0.743	74.655 0.049
7.294 0.128	23.7 0.672	77.007 0.046
7.524 0.126	24.446 0.594	79.432 0.046
7.761 0.121	25.216 0.54	81.934 0.045
8.005 0.124	26.01 0.475	84.515 0.043
8.257 0.128	26.83 0.414	87.177 0.039
8.517 0.132	27.675 0.383	89.923 0.034
8.786 0.134	28.546 0.354	92.755 0.029
9.062 0.134	29.446 0.301	95.676 0.024
9.348 0.139	30.373 0.275	98.69 0.021
9.642 0.151	31.33 0.272	101.799 0.023
9.946 0.174	32.317 0.252	105.005 0.025
10.259 0.191	33.334 0.224	108.312 0.021
10.582 0.223	34.384 0.195	111.724 0.017
10.916 0.248	35.467 0.187	115.242 0.015
11.259 0.283	36.584 0.177	118.872 0.012
11.614 0.321	37.737 0.148	122.617 0.01
11.98 0.354	38.925 0.138	126.478 0.008
12.357 0.417	40.151 0.129	

A.3. PMMA material parameters

elements:

```
H: { count: 8, Z: 1, M: 1.008 g/mol }  
C: { count: 5, Z: 6, M: 12.011 g/mol }  
O: { count: 2, Z: 8, M: 15.999 g/mol }
```

band_structure:

```
model:      insulator  
valence:    2 eV      # set a value other than 0, no literature proof.  
band_gap:   5.6 eV    # from: https://doi.org/10.1063/1.2197973  
affinity:   2.5 eV    # from: https://doi.org/10.1063/1.2197973
```

optical:

```
df_file:    df_PMMA.dat
```

phonon:

```
lattice:    1.54 Å     # C-C bond length
```

isotropic:

```
ac_def: 0.9 eV      # Unknown, tuned such that reasonable mean free  
# paths were obtained
```

longitudinal:

```
c_s: 2746 m/s      # D. Christman, General Motors (1972)
```

transversal:

```
c_s: 1392 m/s      # D. Christman, General Motors (1972)
```

A.4. PMMA optical data

3	5	284	543	-1	8	0.07	60	0.046493839
0.12398	0.029106978				9	0.105	70	0.028319664
0.136378	0.026797948				10	0.145	80	0.018589307
0.142577	0.155646214				11	0.205	100	0.009314816
0.148776	0.158600408				12	0.26	125	0.004482031
0.161174	0.054387977				13	0.315	250	0.000397388
0.173572	0.029106978				14	0.39	287.17	0.002632164
0.179771	0.096022715				15	0.49	329.88	0.00168431
0.18597	0.014571311				16	0.595	378.93	0.001073104
0.210766	0.011847639				17	0.7	435.28	0.000662088
0.2144854	0.173010381				18	0.79	500	0.000407149
0.2182048	0.020469518				19	0.845	543	0.000304282
0.223164	0.00812795				20	0.905	544	0.000581287
0.3	0.00001				21	0.93	1000	6.59348E-05
1	0.00001				22	0.93	2000	4.75978E-06
2	0.00001				23	0.91	4000	3.10476E-07
2.5	0.00001				24	0.88	8000	1.84458E-08
3	0.000384733				27	0.705	16000	1.20048E-09
4	0.001810741				30	0.54	30000	2.0427E-10
5	0.00327799				33	0.38	-1	-1
6	0.015				40	0.175657397		
7	0.02				50	0.083215765		

B

High Performance Cluster Computational Resource

Figure B.1 shows increasing the number of CPU cores on hpc can speed up the simulation significantly, which is very helpful when we are simulating a large number of photoelectrons and their following electron cascade.

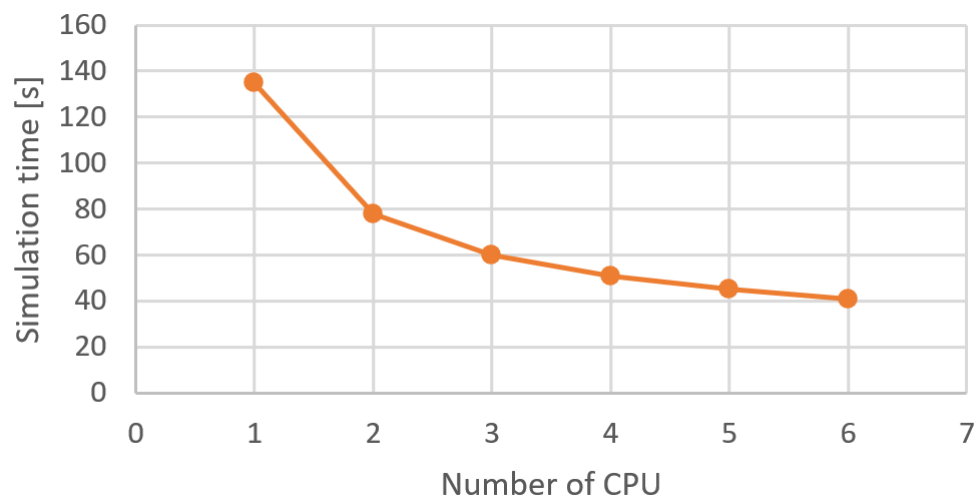


Figure B.1: The effect of the number of CPU cores on simulation time